

von Karman Institute for Fluid Dynamics

Lecture Series 1999-03

## **30<sup>TH</sup> COMPUTATIONAL FLUID DYNAMICS**

March 8 - 12, 1999

ANALYSIS OF PRECONDITIONING METHODS FOR THE EULER AND  
NAVIER-STOKES EQUATIONS

S. Venkateswaran & L. Merkle  
University of Tennessee Space Institute, USA

# Contents

<b>1</b>	<b>Introduction</b>	<b>8</b>
1.1	Understanding Convergence of Time-Marching Algorithms . . . . .	8
1.2	Stability Analysis . . . . .	11
1.2.1	Central-Difference Euler-Implicit Scheme . . . . .	11
1.2.2	Central-Difference ADI Scheme . . . . .	14
1.2.3	Upwind Euler-Implicit Scheme . . . . .	15
1.2.4	Upwind ADI and DDADI schemes . . . . .	21
1.2.5	Upwind Gauss-Seidel Schemes . . . . .	26
1.3	Historical Perspective on Preconditioning . . . . .	27
1.3.1	Preconditioning for the Euler Equations . . . . .	30
1.3.2	Preconditioning for the Navier-Stokes Equations . . . . .	33
1.3.3	Preconditioning for Unsteady Problems . . . . .	34
1.3.4	Preconditioning for Advanced Systems . . . . .	34
1.4	Overview of Contents . . . . .	35
<b>2</b>	<b>Preconditioning for the Euler Equations</b>	<b>37</b>
2.1	Perturbation Analysis of the Low Mach Number Limit . . . . .	37
2.1.1	Equations of Motion . . . . .	37
2.1.2	Perturbation Expansion . . . . .	40
2.1.3	Derivation of Preconditioning . . . . .	42
2.1.4	Characteristics of the Preconditioned System . . . . .	43
2.1.5	Analysis of Artificial Dissipation Models . . . . .	44
2.1.6	Complete Preconditioned Equations . . . . .	46
2.2	Implementation of the Preconditioning System . . . . .	47
2.2.1	Multi-Dimensional Preconditioning System . . . . .	47
2.2.2	Eigenvalues and Definition of Preconditioning Parameter . . . . .	48
2.2.3	Eigenvector Matrices and Flux-Difference Schemes . . . . .	50
2.2.4	Comparison to Turkel and Van Leer Systems . . . . .	50
2.3	Stability and Convergence Studies . . . . .	51
2.3.1	Stability Results . . . . .	51
2.3.2	Convergence Studies . . . . .	52
2.4	Non-Linear Considerations . . . . .	55
2.4.1	Stability and Robustness Issues . . . . .	58

2.4.2	Modification of Preconditioning Definition . . . . .	59
2.4.3	Linearized Dual-Time Preconditioning Method . . . . .	60
<b>3</b>	<b>Preconditioning for the Navier-Stokes Equations</b>	<b>70</b>
3.1	Analytical Solution of the Navier-Stokes Equations . . . . .	70
3.1.1	Standard Navier-Stokes Equations . . . . .	71
3.1.2	Preconditioned Navier-Stokes Equations . . . . .	72
3.2	Perturbation Expansions of the Low Reynolds Number Limit . . . . .	73
3.2.1	Perturbation Expansion and Viscous Preconditioning . . . . .	74
3.2.2	Characteristics of the Preconditioned System . . . . .	76
3.2.3	Analysis of Artificial Dissipation Models . . . . .	78
3.2.4	Complete Viscous Preconditioning System . . . . .	79
3.3	Implementation of Viscous Preconditioning . . . . .	80
3.3.1	Definition of the Viscous Preconditioning Parameter . . . . .	80
3.3.2	Viscous Preconditioning and Time-Step Definition . . . . .	80
3.3.3	Enhanced Definition of Viscous Preconditioning Parameter . . . . .	81
3.4	Analytical Solution of Viscous Preconditioning System . . . . .	83
<b>4</b>	<b>Effects of High Grid Aspect Ratio on Convergence</b>	<b>85</b>
4.1	The Problem of High Aspect Ratios . . . . .	85
4.2	Two-Dimensional ADI Scheme . . . . .	87
4.2.1	Euler Equation Stability Analysis . . . . .	87
4.2.2	Euler Convergence Studies . . . . .	90
4.2.3	Navier-Stokes Stability Analysis . . . . .	92
4.2.4	Navier-Stokes Convergence Studies . . . . .	95
4.3	Three-Dimensional Issues . . . . .	102
<b>5</b>	<b>Preconditioning for the Unsteady Equations</b>	<b>106</b>
5.1	Algorithms for Unsteady Computations . . . . .	107
5.1.1	Unsteady Governing Equations . . . . .	107
5.1.2	Approximate-Newton Method . . . . .	108
5.1.3	Dual-Time Stepping Scheme . . . . .	112
5.2	Perturbation Analysis of the Unsteady Equations . . . . .	113
5.3	Implementation of Unsteady Preconditioning . . . . .	117
5.4	Stability Analysis and Convergence Studies . . . . .	117
5.4.1	One-Dimensional Stability Analysis . . . . .	117
5.4.2	Two-Dimensional Stability Analysis . . . . .	119
<b>6</b>	<b>Preconditioning Formulation for Turbulent Reacting Flows</b>	<b>122</b>
6.1	Computation of Turbulent Flows . . . . .	122
6.2	Computation of Reacting Flows . . . . .	125
6.2.1	Preconditioning System for Reacting Flows . . . . .	125
6.2.2	Numerical Issues in Reacting Computations . . . . .	126
6.2.3	Computational Examples . . . . .	134

<b>7 Conclusions</b>	<b>140</b>
<b>A Governing Equations</b>	<b>142</b>
A.1 Fluid-Dynamic Equations . . . . .	142
A.1.1 1D Navier-Stokes Equations . . . . .	142
A.1.2 2D Navier-Stokes Equations . . . . .	142
A.2 Turbulent Reacting System . . . . .	143
A.2.1 Two-Dimensional Equations . . . . .	143
<b>B Preconditioning System for the Fluids Equations</b>	<b>144</b>
B.1 Preconditioned Equations . . . . .	144
B.1.1 Equations in Generalized Coordinates . . . . .	144
B.1.2 Definition of the Preconditioning Parameter . . . . .	145
B.2 Jacobians and Eigensystem . . . . .	146
B.2.1 Inviscid Jacobians . . . . .	146
B.2.2 Eigenvalues . . . . .	146
B.2.3 Eigenvector Matrices . . . . .	147
<b>C Formulation of Upwind Schemes</b>	<b>148</b>
C.1 Flux-Difference Splitting Procedure . . . . .	148
C.2 Relationship Between Relaxation Methods and Approximate Factorization	149

# List of Figures

1.1	Stability Results. Euler Equations with Euler implicit scheme and central-differences. $M=0.5$ .	13
1.2	Stability Results. Euler Equations with central-differenced ADI scheme. $M=0.5$ .	16
1.3	Stability Results. Euler Equations with central-differenced ADI scheme. $M=0.001$ .	17
1.4	Stability Results. Euler Equations with I/III upwind differences. Euler Implicit scheme. $M=0.5$ .	19
1.5	Stability Results. Euler Equations with I/III upwind differences. Euler Implicit scheme. $M=0.001$ .	20
1.6	Stability Results. Euler Equations with I/III upwind differences. DDADI scheme. $M=0.5$ .	23
1.7	Stability Results. Euler Equations with I/I upwind differences. DDADI scheme. $M=0.5$ .	24
1.8	Stability Results. Euler Equations with I/III upwind differences. Multi-sweep DDADI scheme. $M=0.5$ .	25
1.9	Stability Results. Euler Equations with I/III upwind differences. Point Gauss-Seidel Scheme (DDLU). $CFL=10$ , $M=0.5$ .	28
1.10	Stability Results. Euler Equations with I/III upwind differences. Four-Sweep Line Gauss-Seidel scheme. $M=0.5$ .	29
2.1	Stability results for the preconditioned Euler equations with central difference ADI scheme. $CFL=5$ .	53
2.2	Stability results for the original and preconditioned Euler equations with I/III upwind-DDLGS4 scheme. $CFL=10$ .	54
2.3	Convergence results for central-difference ADI. Inviscid flow in duct.	56
2.4	Convergence results for central-difference ADI. Inviscid flow in duct.	57
2.5	Convergence results vs outer iteration time step for inviscid straight duct. $M = 1 \times 10^{-3}$ .	64
2.6	Convergence results vs CPU time (CRAY-J916) for inviscid straight duct. $M = 1 \times 10^{-3}$ .	66
2.7	Convergence results vs outer iteration time step for inviscid straight duct with different magnitudes of imposed pressure disturbances as initial condition. $M = 1 \times 10^{-3}$ .	67

2.8	Convergence results vs. outer iteration time-step for flat plate boundary layer. $M = 1 \times 10^{-3}$ and $Re_x = 100$ . . . . .	68
2.9	Convergence results vs. CPU time (CRAY-J916) for flat plate boundary layer. $M = 1 \times 10^{-3}$ and $Re_x = 100$ . . . . .	69
4.1	Three types of high aspect ratio cells for three-dimensional problems. . . . .	86
4.2	Euler stability for the preconditioned, 2-D centrally-differenced ADI scheme with $AR=100$ , $M=0.001$ , $v/u=1$ . Left side: $CFL_x=0.01$ , $CFL_y=1$ ; Right side: $CFL_x=0.1$ , $CFL_y=10$ . . . . .	88
4.3	Euler stability for the preconditioned, 2-D centrally-differenced ADI scheme with $AR=100$ , $M=0.001$ , $v/u=1$ . Left side: $CFL_x=1$ , $CFL_y=100$ ; Right side: $CFL_x=3$ , $CFL_y=300$ . . . . .	89
4.4	Euler stability for the preconditioned, 2-D centrally-differenced ADI scheme with $AR=1 \times 10^4$ , $M=0.001$ , $v/u=1$ . $CFL_x=3$ , $CFL_y=3 \times 10^4$ . . . . .	90
4.5	Grid geometry ( $41 \times 41$ ) for the straight channel cases showing aspect ratios from unity to 1000. . . . .	91
4.6	Convergence for the inviscid straight channel cases at aspect ratios from unity to 100, using max-CFL=3. . . . .	91
4.7	Contours of the residual errors for the pressure for the $AR=100$ case, using max-CFL=3. Errors are purely one-dimensional, longitudinal modes. . . . .	92
4.8	Convergence for the inviscid straight channel cases at aspect ratios from unity to $1 \times 10^4$ , using min-CFL=3. . . . .	93
4.9	Contours of the maximum absolute eigenvalue of the amplification matrix for the preconditioned Navier-Stokes stability of the 2-D central difference ADI scheme. $AR=1000$ , $M=0.001$ , $v/u=1$ , $Re_{\Delta x}=100$ , $CFL_x=1$ , $VNN_x=1$ . . . . .	93
4.10	Contours of the maximum absolute eigenvalue of the amplification matrix for the preconditioned Navier-Stokes stability of the 2-D central difference ADI scheme. $AR=1000$ , $M=0.001$ , $v/u=1$ , $Re_{\Delta x}=100$ , $CFL_x=1$ , $VNN_y=1$ . . . . .	95
4.11	Convergence for the fully-developed viscous straight channel case at aspect ratio of 1000 with viscous preconditioning. Standard time-step definition (max-CFL/max-VNN), and improved time-step definition (min-CFL/max-VNN). . . . .	96
4.12	Convergence for the fully-developed viscous straight channel cases at aspect ratios from unity to $1 \times 10^4$ , using min-CFL/max-VNN. . . . .	97
4.13	Shear layer hydrogen mass fraction profiles . . . . .	98
4.14	Convergence for multi-species shear layer for standard and enhanced algorithms. I – min-CFL/max-VNN and MOC II boundary conditions with viscous preconditioning; II – max-CFL/max-VNN, MOC II, viscous preconditioning; III – min-CFL/max-VNN, MOC II, with inviscid preconditioning but no viscous preconditioning; IV – no preconditioning. . . . .	98
4.15	Convergence for flat plate boundary layer for standard and enhanced algorithms . . . . .	99
4.16	Laminar boundary layer solution . . . . .	100

4.17	Turbulent boundary layer solution . . . . .	101
4.18	Stretched grid and Mach contours for the turbulent nozzle computation. . .	101
4.19	Convergence for nozzle computations with the standard algorithm (without aspect ratio control) and the enhanced algorithm (min-CFL/max-VNN). . .	102
4.20	Temporal convergence of the heat flux along the nozzle wall for both the standard algorithm and the enhanced algorithm. . . . .	103
5.1	Stability Results. Approximate-Newton Scheme. Central-Difference ADI. M=0.5, $CFL_{u+c} = 1$ . . . . .	110
5.2	Stability Results. Approximate-Newton Scheme. Central-Difference ADI. M=0.001, $CFL_{u+c} = 1$ and $CFL_u = 1$ . . . . .	111
5.3	Stability Results for Dual Time Scheme, Central-Difference ADI, Steady Preconditioning. M=0.001, $CFL_\tau = 3$ , $CFL_{u+c} = 1$ and $CFL_u = 1$ . . . . .	114
5.4	Stability Results for Dual Time Scheme, Central-Difference ADI, Unsteady Preconditioning. M=0.001, $CFL_\tau = 3$ , $CFL_{u+c} = 1$ and $CFL_u = 1$ . . . . .	120
5.5	Stability Results. Dual-Time Scheme with Unsteady Preconditioning. Upwind DDLGS. M=0.001, $CFL_\tau = 3$ , $CFL_{u+c} = 1$ and $CFL_u = 1$ . . . . .	121
6.1	Hydrogen/Oxygen Constant Volume Bomb. Temperature vs. Time. . . . .	130
6.2	Hydrogen/Oxygen Constant Volume Bomb. Maximum Eigenvalue vs. Time.	131
6.3	Hydrogen/Oxygen Constant Volume Bomb. Minimum Eigenvalue (Magnitude) vs. Time. . . . .	132
6.4	Hydrogen/Oxygen Constant Volume Bomb. Time-Step Size vs. Time. . . . .	133
6.5	Temperature contours for methane/air laminar diffusion flame. . . . .	135
6.6	Convergence results for methane/air laminar diffusion flame. . . . .	136
6.7	Comparison of species profiles for methane/air laminar diffusion flame. . . . .	136
6.8	Convergence results for non-reacting turbulent shear layer. . . . .	137
6.9	Temperature Contours for reacting turbulent shear layer. . . . .	138
6.10	Convergence results for reacting turbulent shear layer. . . . .	139
6.11	Comparison with experimental data for reacting turbulent shear layer. . . . .	139

# List of Tables

3.1	Original Navier-Stokes . . . . .	72
3.2	Preconditioned Navier-Stokes, $\epsilon_p=M^2$ . . . . .	74
3.3	Preconditioned Navier-Stokes . . . . .	84

# Chapter 1

## Introduction

In this introductory section, we begin with a discussion of the convergence characteristics of time-marching algorithms and a historical perspective on the use of preconditioning to enhance convergence. In particular, we provide an overview of von Neumann stability theory and demonstrate its usefulness as a tool for understanding and predicting numerical convergence behavior. Indeed, in the current study, we rely upon a combination of stability analysis and perturbation methods to guide the selection of preconditioning systems. The historical perspective presents an overview of preconditioning methods, starting from the seminal developments of Chorin's artificial compressibility method for incompressible flow up to recent research with reacting and multi-phase systems. Finally, we present an overview of the contents of the remaining chapters in this text.

### 1.1 Understanding Convergence of Time-Marching Algorithms

Preconditioning techniques involve the alteration of the time-derivatives used in time-marching computational fluid dynamics (CFD) methods with the objective of enhancing their convergence and stability characteristics. The original motivation for the development of these techniques arose from the need to compute low speed compressible flows efficiently. Traditional time-marching algorithms that use the physical time-derivatives in their formulation have been extremely successful in the computation of transonic and supersonic flows; however, at low Mach numbers, their performance suffers because of the wide disparity that exists between the particle and acoustic wave speeds. Preconditioning methods introduce artificial time-derivatives which alter the acoustic waves so that they travel at speeds that are comparable in magnitude to the particle waves. Thereby, good convergence characteristics may be attained at all speeds. Further, the preconditioning techniques may be tailored to improve performance for viscous-dominated flows, unsteady flows, high-aspect ratio grids, turbulent flows, reacting flows and multi-phase systems. In each of these instances, the preconditioning procedure must be adapted to account for the controlling flow physics. The development, analysis and application of these methods,

therefore, rest upon appreciating the close connection between the physics of fluid flow and the mathematics of convergence. Accordingly, we begin by discussing the convergence behavior of traditional time-marching systems.

All CFD algorithms involve an iterative procedure to attain the desired steady-state solution because of the inherent non-linearity of the governing equations. Time-marching methods represent a special class of CFD methods, wherein the iterative procedure is cast within a time-marching framework (*e.g.*, see [1, 2, 3]). These methods utilize the time-dependent (or unsteady) form of the governing equations. Starting from an “arbitrary” initial condition, they advance the solution in time until the transient errors are convected out of the system or damped and a time-independent steady state is reached. Because of the nature of this time-iterative procedure, the process of convergence is intimately related to the unsteady flow physics, which, in turn, make these methods extremely appealing from the viewpoint of understanding, predicting and enhancing convergence behavior (*e.g.*, see [3]).

There are two principal agents that are responsible for removing errors from a time-marching system—convection and dissipation. In other words, errors may be convected out of the system (through boundaries) and/or they may be damped within the system. Convection is embodied within the wave propagation processes that are inherent in the fluid dynamic equations, while dissipation is embodied within the diffusion or viscous processes. As an illustration, consider the one-dimensional Navier-Stokes equations:

$$\frac{\partial Q}{\partial t} + \frac{\partial E}{\partial x} = \frac{\partial}{\partial x} \left( R_{xx} \frac{\partial Q_p}{\partial x} \right) \quad (1.1)$$

where the solution vector,  $Q$ , the inviscid flux,  $E$ , and the viscous matrix,  $R_{xx}$ , are given in Appendix A.1.1. The inviscid fluxes contain the convective modes, while the viscous fluxes furnish the damping modes of the Navier-Stokes system. In particular, the inviscid modes are represented by the eigenvalues of the inviscid flux Jacobian,  $A = \partial E / \partial Q$ , which for the one-dimensional system are the particle wave speed ( $u$ ) and the acoustic wave speeds ( $u \pm c$ ). These “inviscid” modes interact with the “viscous” modes, resulting in a system that is rich in physical complexity.

Focusing our attention on the Euler equations subset (obtained by dropping the viscous flux terms from Eqn. 1.1), we note that the physical equations are described by the three convective wave speeds (*i.e.*,  $u$ ,  $u + c$  and  $u - c$ ) and no damping modes are present. It is useful to consider the Euler equations in their so-called characteristic form:

$$\frac{\partial \hat{Q}}{\partial t} + \Lambda \frac{\partial \hat{Q}}{\partial x} = 0 \quad (1.2)$$

where  $\partial \hat{Q} = M^{-1} \partial Q$ ,  $\Lambda = \text{diag}(u, u + c, u - c)$  and  $M^{-1}$  is the modal matrix, consisting of the left eigenvectors of  $A$  and satisfying the relation,  $M^{-1} A M = \Lambda$ . It is apparent that the Euler equations represent a set of three wave equations in the characteristic variable  $\hat{Q}$ . Errors present in the characteristic variables are accordingly transported out of the system at the wave speeds of the system, *i.e.*,  $u$ ,  $u + c$  and  $u - c$ .

The inherent strengths and limitations of the traditional time-marching algorithm are readily apparent. At transonic and supersonic speeds, the acoustic wave speeds are of the same magnitude as the particle wave speed, which means that all disturbances are transported out of the system in commensurate fashion and efficient convergence is obtained. Indeed, we note that time-marching methods were originally developed for transonic and supersonic aerodynamics computations, and so, this observation is not surprising. At low speeds, however, the particle wave speed can be orders of magnitude smaller than the acoustic wave speeds. The particle and acoustic error modes are then transported at widely varying time-scales. Since stability constraints typically force the selection of finite time-step sizes, it is evident that acoustic modes would be propagated efficiently, while the particle modes would languish. This naturally results in poor convergence rates of the standard time-marching algorithm. This problem of highly disparate wave-speeds is commonly referred to as a “stiffness” or “ill-conditioning” of the governing time-marching system.

Preconditioning involves replacing the natural time-derivatives of the physical system by introducing artificial time-derivatives in order to eliminate the stiffness in the wave-speeds and render the system well-conditioned. A simple preconditioning method for the 1D Euler system in Eqn. 1.2 is to premultiply the time-derivative by a matrix as follows:

$$|\Lambda| \frac{\partial \hat{Q}}{\partial t} + \Lambda \frac{\partial \hat{Q}}{\partial x} = 0 \quad (1.3)$$

where  $|\Lambda| = \text{diag}(|u|, |u+c|, |u-c|)$ . This “preconditioned” system may be re-transformed to the original conservative form:

$$|A| \frac{\partial Q}{\partial t} + \frac{\partial E}{\partial x} = 0 \quad (1.4)$$

where  $|A| = M|\Lambda|M^{-1}$ . The magnitudes of the eigenvalues of this modified system are all unity, indicating that the system is perfectly conditioned. Also, note that the system maintains the signs of the original eigenvalues, i.e, two positive and one negative for subsonic flow (assuming  $u > 0$ ) and all positive for supersonic flow. While this is a nice “textbook” example to show how preconditioning systems may be derived, this procedure is, in fact, not very useful for low Mach numbers in practice, one reason being the difficulty of extending it to multi-dimensions.

We have noted that the Euler equations are described completely by convective wave physics and there is no dissipation mechanism present in the system. This is, of course, true only at the partial differential equation level. Practical schemes always involve the presence of “artificial” dissipation terms arising from the discretization of the spatial and temporal terms. Central differencing of the spatial terms is usually accompanied by the overt addition of artificial dissipation terms, while upwind differencing inherently possesses dissipation. One-sided temporal discretizations, likewise, introduce dissipative modes. We will consider the effect of such artificial dissipation terms later in the text. For the present time, it is sufficient to note that the forms and magnitudes of the artificial dissipation

terms are typically determined by the eigenvalues of the Euler system. Thus, for an ill-conditioned system, the artificial dissipation terms can also become ill-conditioned and our observations regarding the convergence difficulties remain valid.

In this section, we have seen how understanding the physics of time-marching procedures aids in understanding the numerical convergence process. In fact, it is often equally instructive to examine non-time-marching iterative methods from a time-marching perspective for this reason. Of course, our observations regarding the convergence performance have hitherto been of a qualitative nature. In the following section, we will see how more quantitative assessments of convergence behavior may be obtained by using classical linear stability theory.

## 1.2 Stability Analysis

Von Neumann stability analysis is a valuable analytical tool for studying the manner in which errors in the solution are amplified (instability) or damped (stability) [1, 2, 3]. More importantly, stability analysis can tell us how fast the errors will decay, providing a quantitative or semi-quantitative estimate of the convergence rate of the algorithm. We note that there are several simplifying assumptions employed in the stability analysis. Firstly, von Neumann theory uses Fourier series and requires a set of linear, constant coefficient equations. Also, the effect of boundary conditions are ignored and the situation corresponds to the use of periodic boundary conditions. In spite of these limitations, empirical evidence suggests that the stability results are extremely meaningful for practical fluid dynamic computations. We further note that although stability theory is generally utilized in textbooks to analyze model scalar equations, we employ it here to study the complete, coupled Navier-Stokes equations.

In this section, we outline the stability procedure and present an overview of stability results for several classical time-marching algorithms. We will see all practical algorithms introduce a constraint on the the time-step size, that is related to the wave speeds (for the inviscid Euler equations). It is this time-step restriction that is responsible for the poor performance of the schemes for ill-conditioned problems such as low Mach number flows. In later sections, we use stability studies to demonstrate how preconditioning systems alleviate such difficulties and enable reliable convergence behavior.

### 1.2.1 Central-Difference Euler-Implicit Scheme

We begin with the two-dimensional Euler equations:

$$\frac{\partial Q}{\partial t} + \frac{\partial E}{\partial x} + \frac{\partial F}{\partial y} = 0 \quad (1.5)$$

The terms are defined in Appendix A.1.2. For simplicity, we have not included the artificial dissipation terms that are customary for central-differencing. Expressing the

Euler Implicit scheme in the so-called “delta” form, we get:

$$\left[ I + \Delta t \frac{\partial A}{\partial x} + \Delta t \frac{\partial B}{\partial y} \right] \Delta Q = -\Delta t \mathcal{R}^n \quad (1.6)$$

where  $\Delta Q = Q^{n+1} - Q^n$ ,  $\Delta t$  is the time-step size and the residual  $\mathcal{R} = \frac{\partial E}{\partial x} + \frac{\partial F}{\partial y}$ . As the time-marching iterations converge, the change in the solution vector approaches zero and the desired steady state equations, represented by the residual,  $\mathcal{R}$ , is satisfied.

For central differencing of the convective fluxes, von Neumann stability analysis yields the following expression for the amplification matrix:

$$G = \left[ I + A \frac{\Delta t}{\Delta x} i S_x + B \frac{\Delta t}{\Delta y} i S_y \right]^{-1} \quad (1.7)$$

where the amplification matrix  $G$  is defined as,  $Q^{n+1} = G Q^n$  and  $S_x = \sin(k \Delta x)$  and  $S_y = \sin(l \Delta y)$ . The magnitude of the eigenvalues of  $G$  (i.e.,  $|g_k|$ ) represent the stability characteristics of the Euler implicit algorithm and are commonly referred to as amplification factors. The amplification factors determine whether errors in the system are damped ( $|g_k| < 1$ ) or amplified ( $|g_k| > 1$ ) and, more importantly, depending on their precise magnitudes, they determine the convergence rate. Thus, if  $|g_k| \rightarrow 0$ , we would anticipate rapid damping of errors (and rapid convergence), while if  $|g_k| \rightarrow 1$ , we would expect very little damping (and, typically, slow convergence).

For the central-difference, Euler implicit scheme in Eqn. 1.7, it is straightforward to see that the stability results are characterized by three non-dimensional parameters or the “CFL” numbers, namely,  $CFL_u = u \Delta t / \Delta x$ ,  $CFL_{u+c} = (u + c) \Delta t / \Delta x$  and  $CFL_{u-c} = (u - c) \Delta t / \Delta x$ . Further, it is clear that the scheme is unconditionally stable, and the amplification factors approach unity as the CFL numbers approach zero, while they approach zero as the CFL numbers approach infinity. These observations suggest that large CFL numbers (or time-steps) may be safely employed (at least, for the linear problem) and rapid convergence would be obtained.

Figure 1.1 shows the maximum of the eigenvalues of the amplification matrix obtained numerically as a function of wave-number space for  $CFL_{u+c} = 1$  and 100 respectively. Here,  $M = 0.5$ ,  $u = v$  and typical values are employed for the other flowfield parameters. Note that, at  $CFL = 1$ , there is reasonable damping of the mid-wavenumbers, but little damping at the low and high wavenumber regions. At the higher CFL, excellent damping properties are observed over the entire wavenumber domain, indicating rapid convergence. (The peaks in the amplification factor at the high wave numbers are due to the absence of artificial dissipation and are readily damped by the addition of the same.) At even higher CFL numbers, the amplification factors approach zero over the entire domain. Thus, with the Euler implicit scheme, extremely fast convergence would be obtained when large CFL numbers are used.

Three further observations may be made with regard to the above result. Firstly, we note that the stability analysis indicates strong damping characteristics for the Euler implicit scheme, although the Euler equations themselves possess only convective terms and

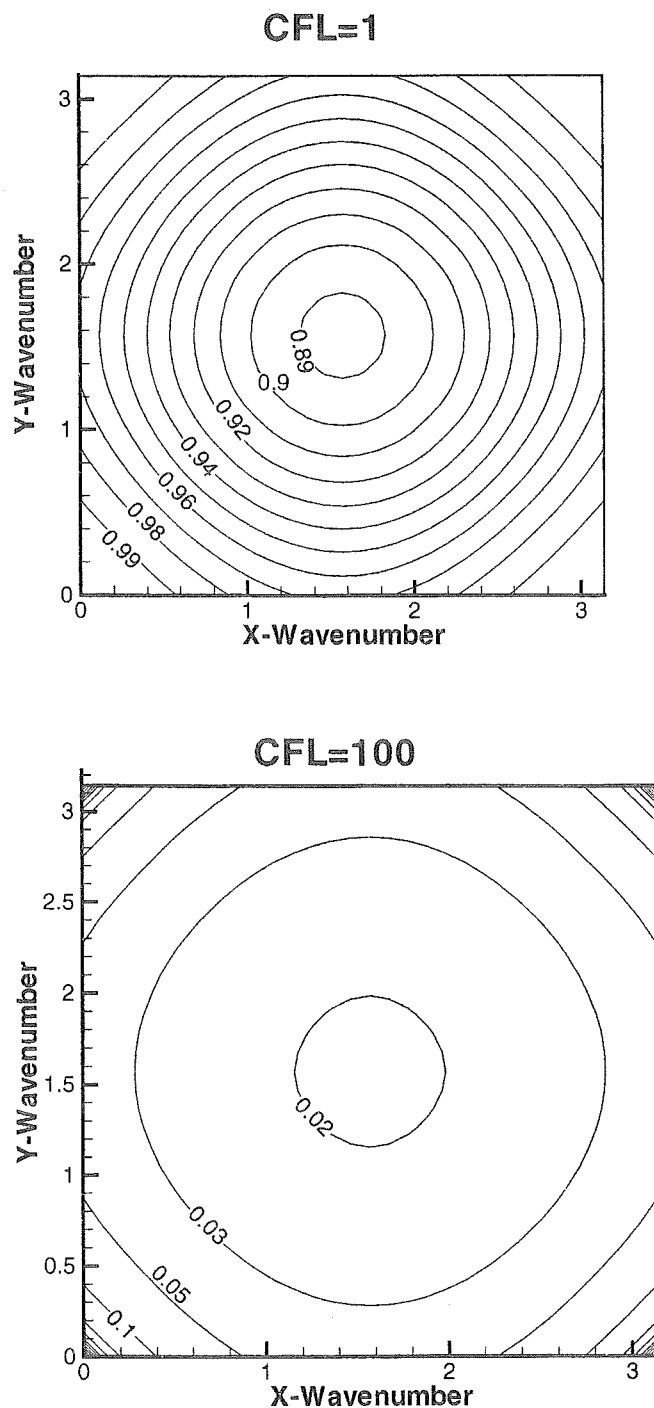


Figure 1.1: Stability Results. Euler Equations with Euler implicit scheme and central-differences.  $M=0.5$ .

no artificial dissipation terms have been explicitly added. The source of the damping is, of course, the backward-differencing used in the temporal discretization, made evident by examining the “equivalent” pde (*e.g.*, see [1]) for the scheme. Addition of physical and/or artificial dissipation (discussed later) will introduce further damping, that is preferentially more pronounced at the high wave numbers [3].

The second observation is that the stability results reveal only part of the convergence story—*i.e.*, they indicate only the extent to which errors are damped and do not provide an estimate of the convective transport of errors. However, in practice, convective transport by itself is not a very effective means of attaining convergence because practical boundary conditions inevitably cause reflection of errors back into the domain, which, in turn, need to be damped. Numerical convergence behavior is, therefore, largely determined by the damping introduced by the scheme, making stability analysis a critical tool for predicting algorithmic performance.

Finally, we note that at low Mach numbers, since the acoustic speeds are much greater than the particle speeds, the corresponding CFL numbers have disparate magnitudes. This would mean that while the acoustic CFL numbers are large and damp out the acoustic modes effectively, the particle CFL numbers may remain small and the associated error modes may languish. However, for the direct scheme considered here, this problem will not limit performance since the CFL numbers may be chosen to be infinitely large. (In practice, difficulties do arise due to the definition of the artificial dissipation terms, which are discussed later.) At any rate, direct solution implicit schemes are impractical for CFD computations and approximate inversion techniques are typically used. As we will see in the following sections, such approximate methods typically introduce additional constraints on the time-step definition, which lead to serious convergence difficulties for low Mach number problems.

### 1.2.2 Central-Difference ADI Scheme

The central-difference ADI algorithm [4, 5, 6] may be written as:

$$\left[ I + \Delta t \frac{\partial A}{\partial x} \right] \left[ I + \Delta t \frac{\partial B}{\partial y} \right] \Delta Q = -\Delta t \mathcal{R}^n \quad (1.8)$$

Note that the two-dimensional implicit operator on the left-hand side (LHS) is replaced by the product of two one-dimensional (block tridiagonal) operators, which are more straightforward to solve. The penalty for this approximation is the introduction of “approximate-factorization” (or AF) error terms on the LHS, which are given by  $\Delta t^2 \frac{\partial A}{\partial x} \frac{\partial B}{\partial y}$ . Because these error terms are proportional to  $\Delta t^2$ , convergence difficulties occur at large time-step sizes (or CFL numbers) as we will presently see. The right-hand side (RHS) residual, however, remains unchanged, and, therefore, solution accuracy is not compromised.

Von Neumann stability analysis gives the following result for the amplification matrix:

$$G = \left[ I + A \frac{\Delta t}{\Delta x} i S_x + B \frac{\Delta t}{\Delta y} i S_y - AB \frac{\Delta t^2}{\Delta x \Delta y} \right]^{-1} \left[ I - AB \frac{\Delta t^2}{\Delta x \Delta y} \right] \quad (1.9)$$

It is evident upon examining this expression that the scheme is unconditionally stable. However, as the CFL numbers approach infinity, the approximate factorization errors dominate and the amplification factors approach unity. This fact is clearly observed in the stability results given Fig. 1.2 for  $CFL = 5$  and  $CFL = 100$  with  $M = 0.5$  and  $u = v$ . (Unless otherwise specified, the CFL numbers here and elsewhere in this text refer to  $CFL_{u+c}$ ). For low CFL numbers (i.e., around unity or less), the stability results resemble the Euler implicit results presented earlier because the factorization errors are negligibly small. As the CFL number increases, the amplification factors decrease initially as for the Euler implicit scheme, until the AF errors start to dominate, causing the amplification factor to approach unity. At  $CFL = 5$ , the amplification factors show reasonable damping over the entire wavenumber domain, although the influence of the AF errors is starting to become significant at the mid-wavenumbers. At  $CFL = 100$ , the AF errors dominate over the entire wavenumber space and the amplification factor is unity everywhere (with the exception of the purely one-dimensional modes that occur along the axes of the stability plots). Thus, the ADI scheme promises optimal convergence for intermediate values of the CFL number, typically in the range of 5 to 10.

Figure 1.3 shows the maximum amplification factors for a low Mach number ( $M = 0.001$  and  $u = v$ ). For  $CFL_{u+c} = 5$ , which would be about the normal operating value for this parameter, we observe that  $CFL_u = CFL_v = 0.005$ , which means that the error modes corresponding to the particle waves are propagated and damped very slowly. Indeed, the stability result shows that the amplification factor is essentially unity over the entire wavenumber region, indicating very poor convergence. On the other hand, at  $CFL_u = 5$ , the particle wave modes are handled optimally, while the acoustic CFL numbers are much larger than their optimal values ( $CFL_{u+c} = CFL_{v+c} = 5000$ ). Consequently, the AF errors dominate these modes, resulting again in poor damping and convergence.

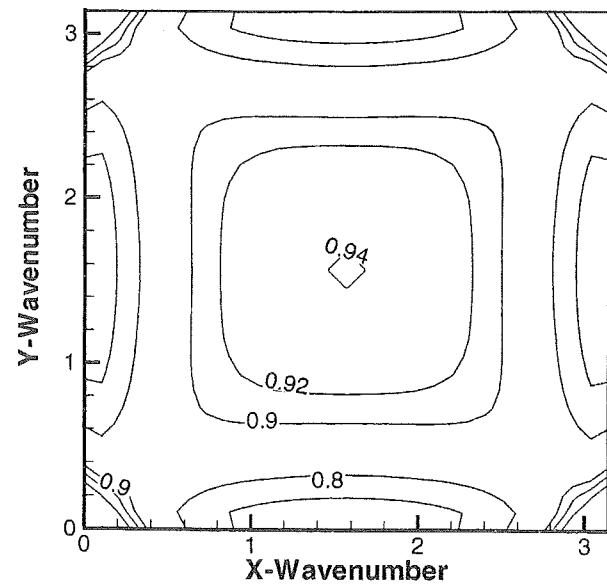
Before closing, we briefly consider explicit schemes such as the popular multi-stage Runge-Kutta schemes. Unlike implicit schemes, explicit methods are conditionally stable, which means that the time-step has to be selected according to the stability criterion. For the four-stage Runge-Kutta scheme, it is well-known that the maximum allowable time-step is given by,  $CFL_{u+c} + CFL_{v+c} = 2\sqrt{2}$ . This means that for low Mach number conditions, the particle CFL numbers ( $CFL_u$  and  $CFL_v$ ) will necessarily be very small, meaning that these modes will not be damped at all. Thus, both explicit and implicit time-marching techniques suffer serious convergence degradation at low Mach numbers.

### 1.2.3 Upwind Euler-Implicit Scheme

We next turn our attention to the stability and convergence properties of implicit upwind schemes. We will consider the representation of the convective fluxes using standard flux-difference splitting methods [2, 7]. Complete details are given in Appendix C.1. Application of the Euler implicit scheme yields the following:

$$\left[ I + \frac{\Delta t}{\Delta x} (\nabla_x \mathcal{A}^+ + \Delta_x \mathcal{A}^-) + \frac{\Delta t}{\Delta y} (\nabla_y \mathcal{B}^+ + \Delta_y \mathcal{B}^-) \right] \Delta Q = -\Delta t \mathcal{R}^n \quad (1.10)$$

**CFL=5**



**CFL=100**

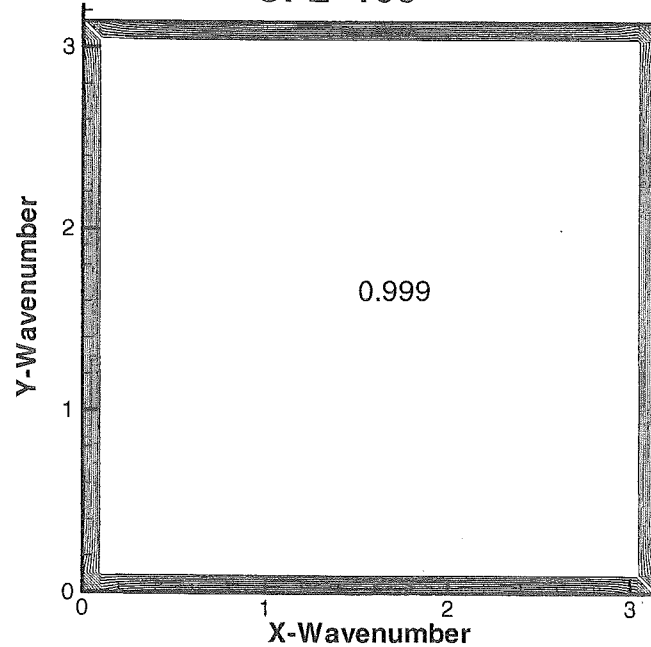


Figure 1.2: Stability Results. Euler Equations with central-differenced ADI scheme.  
 $M=0.5$ .

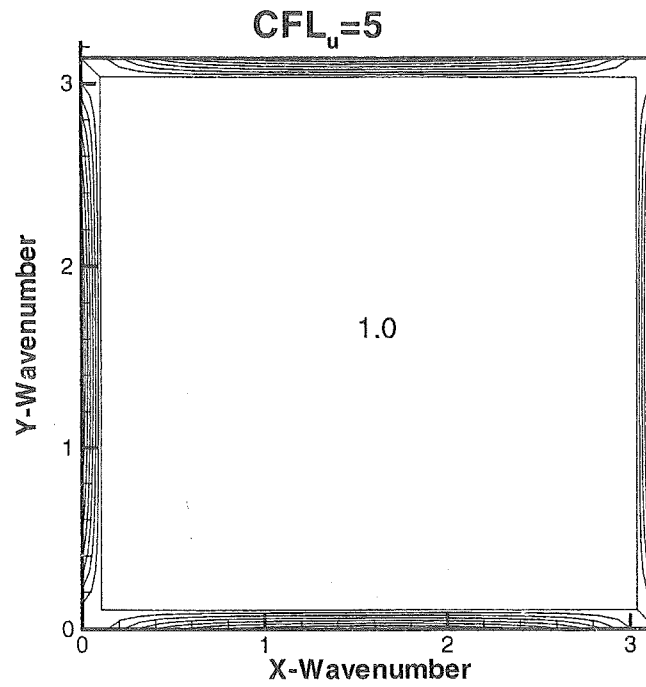
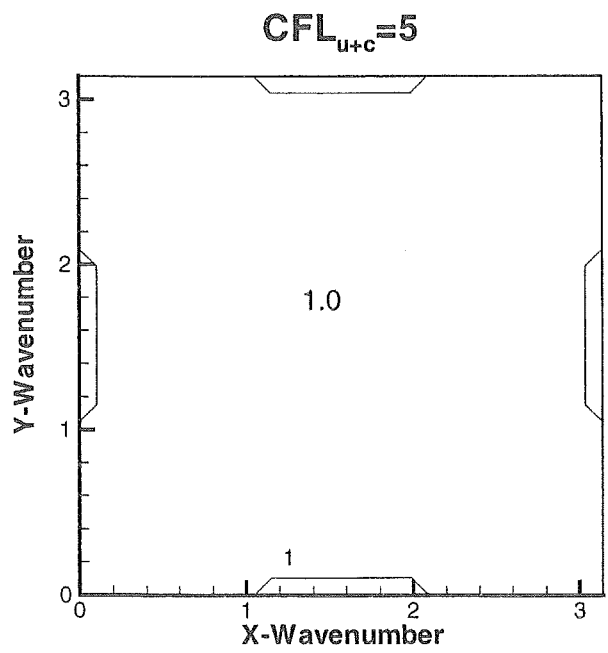


Figure 1.3: Stability Results. Euler Equations with central-differenced ADI scheme.  
 $M=0.001$ .

where  $\Delta_x$  and  $\nabla_x$  represent first-order forward, and first-order backward differencing in  $x$ , with similar definitions for the  $\Delta_y$  and  $\nabla_y$  operators. The quantity  $\mathcal{R}^n$  represents the residual of the steady-state equations. The definitions of the Jacobians  $\mathcal{A}^\pm$  and  $\mathcal{B}^\pm$  are also given in Appendix C.1.

The residual operator on the RHS is typically treated using third-order upwind biased differences. In Eqn. 1.10, however, we have employed first-order upwind differences on the LHS operator. This is the usual choice in most CFD codes because third-order differencing on the LHS would increase the band-width of the associated block matrix. Also, the first-order matrix on the LHS is more diagonally dominant, allowing the use of a wide range of approximate matrix inversion methods (beside ADI) as discussed in the following sections. Most of our discussion will focus on the first-order LHS/third-order RHS (or I/III) system. Occasionally, we will discuss the properties of the I/I and the III/III systems as well.

Figure 1.4 shows the stability results for the direct solution of the I/III system given in Eqn. 1.10 for  $CFL = 1$  and  $100$ . Compared to the central-differencing case (Fig. 1.1), we note that the upwind scheme is also unconditionally stable; however, there are some differences. The first difference is that the high wavenumbers are now damped. This is because, unlike central differences, the upwind discretization inherently contains artificial dissipation terms. Secondly, it is interesting to note that, at the higher  $CFL$  ( $CFL = 100$ ), the scheme shows improved damping at the low wavenumbers (similar to the central difference result), but at the mid- and high-wavenumbers, the gains are not as dramatic. In fact, even at much higher  $CFL$  numbers (not shown here), the stability results closely resemble the results at  $CFL = 100$ . This indicates that, although the scheme is unconditionally stable, the relative gains of running at very high  $CFL$  numbers are modest. In contrast, the stability results for the I/I and III/III systems show that the amplification factors approach zero over the entire domain as the  $CFL$  approaches infinity, which is in agreement with the central-difference result. Thus, the “freezing” of the amplification factors for the I/III system occurs because of the inconsistency between the first-order LHS and the third-order RHS.

The I/III inconsistency also leads to interesting results for low Mach number computations. Figure 1.5 shows results for  $CFL = 100$  and  $CFL = 1 \times 10^6$  for  $M = 0.001$ . It should be noted that these are the acoustic  $CFL$  numbers and the corresponding particle  $CFL$  numbers,  $CFL_u = CFL_v = 0.1$  and  $1000$  respectively. Thus, at the lower  $CFL$  shown, the scheme is non-optimal for the particle modes and the amplification factor is close to unity, particularly at low wavenumbers. At the higher  $CFL$  shown, all the relevant  $CFL$  numbers are large; however, we observe that, while there is good damping at the high wavenumber regions, the low wavenumber region is still beset with amplification factors close to unity. Even at much higher  $CFL$  values, the amplification factor distribution remains unchanged, which, as we saw earlier, is a facet of the I/III inconsistent differencing. In practical computations, these low-frequency modes would control the convergence process, thereby rendering this scheme inefficient for low-speed computations. Thus, practical upwind schemes demonstrate low Mach number difficulties even for the “direct” or “unfactored” scheme.

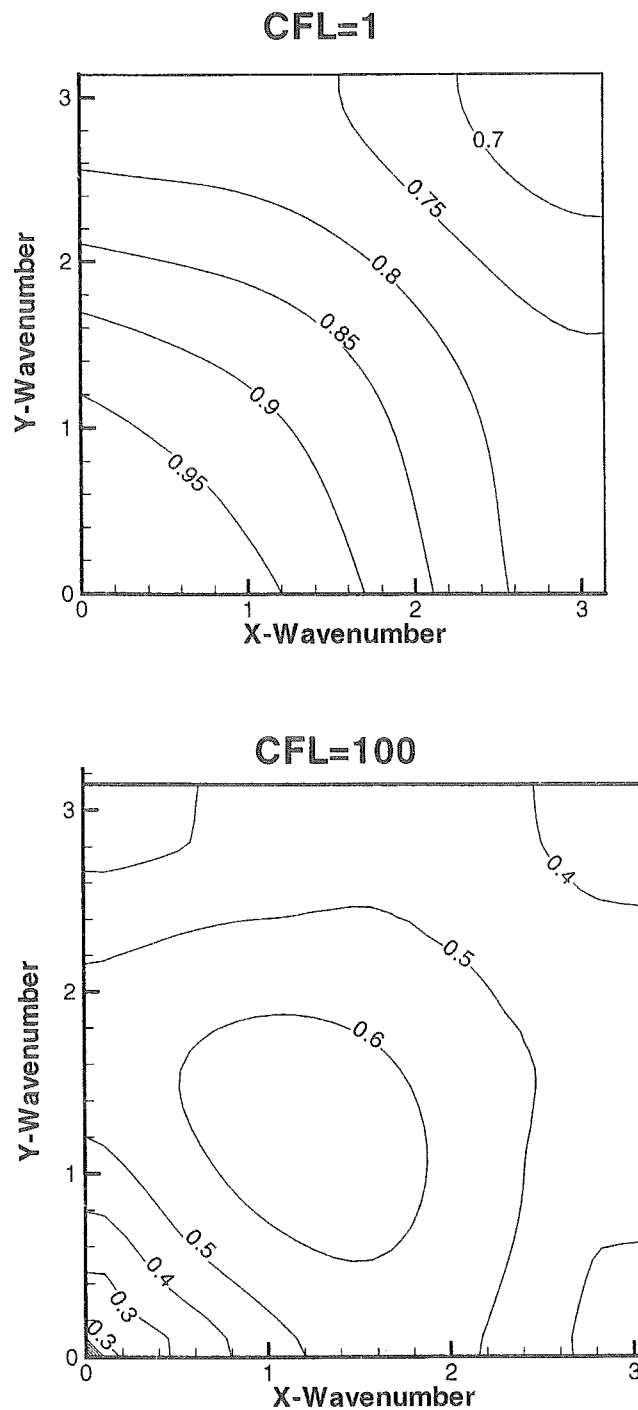


Figure 1.4: Stability Results. Euler Equations with I/III upwind differences. Euler Implicit scheme.  $M=0.5$ .

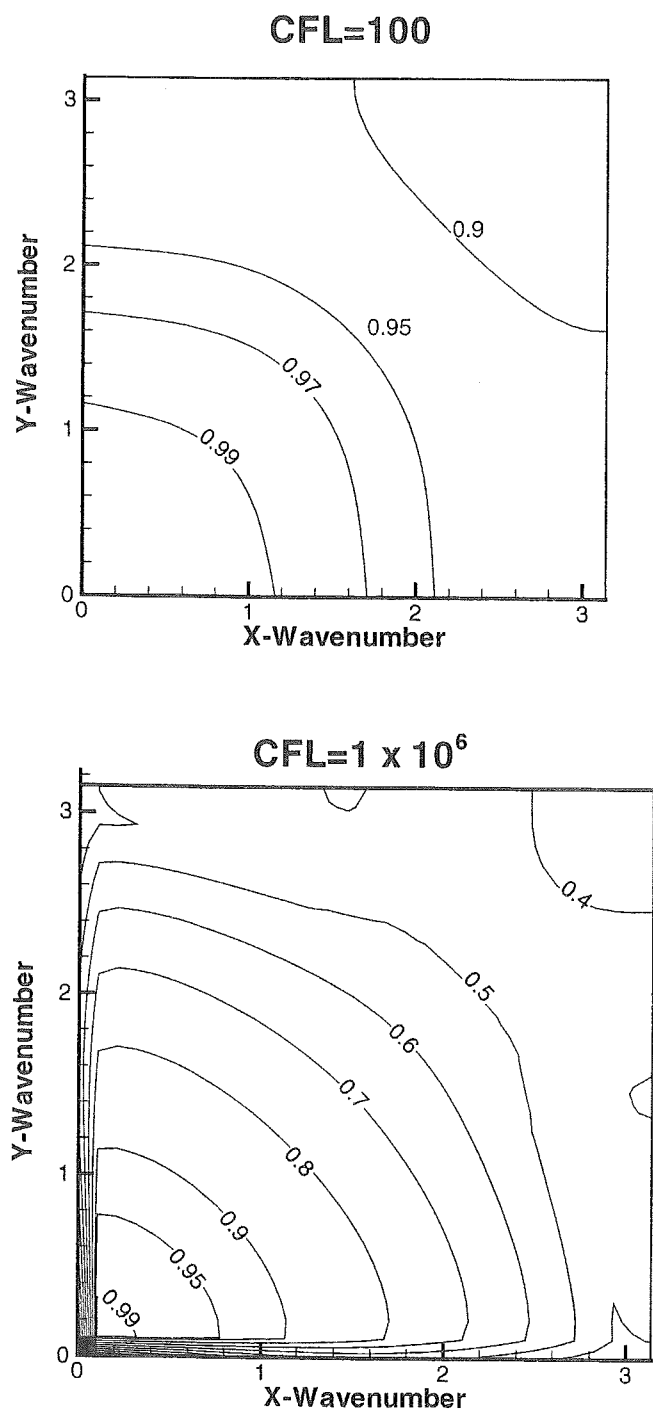


Figure 1.5: Stability Results. Euler Equations with I/III upwind differences. Euler Implicit scheme.  $M=0.001$ .

### 1.2.4 Upwind ADI and DDADI schemes

Efficient solution of Eqn. 1.10 requires that it be solved by some approximate means. The diagonally dominant form of the first-order LHS allows numerous methods to be used [8, 9]. Here, we consider three common algorithms (along with minor modifications as noted below): upwind implementation of the alternating-direction implicit (ADI) [10] the point Gauss-Seidel method (LU factorization) [11] and the line Gauss-Seidel (LGS) method [12]. Although the symmetric point- and line-Gauss Seidel algorithms are commonly referred to as relaxation algorithms, in fact, they can be written as approximate factorization schemes [50]. Accordingly, we use the following generic factorized form to express all of the algorithms considered here:

$$(\mathcal{D} + \mathcal{T}_1)\mathcal{D}^{-1}(\mathcal{D} + \mathcal{T}_2)\Delta Q = -\Delta t \mathcal{R}^n \quad (1.11)$$

where  $\mathcal{D}$  is the block-diagonal term.

Firstly, we distinguish between “non-diagonally dominant” and “diagonally-dominant” formulations. The standard upwind-ADI procedure involves approximately factoring the LHS operator in Eqn. 1.10 before discretization. The diagonal contributions of the spatial difference operators then do not contribute to the  $\mathcal{D}$  term in Eqn. 1.11. Hence, we refer to the standard ADI scheme as non-diagonally dominant. On the other hand, if the discretization is performed first and all diagonal terms are grouped together (into  $\mathcal{D}$ ) before approximate factorization, the resulting scheme would be diagonally-dominant.

The standard upwind-ADI scheme may be written as:

$$\begin{aligned} \mathcal{D} &= I \\ \mathcal{T}_1 &= \frac{\Delta t}{\Delta x}(\nabla_x \mathcal{A}^+ + \Delta_x \mathcal{A}^-) \\ \mathcal{T}_2 &= \frac{\Delta t}{\Delta y}(\nabla_y \mathcal{B}^+ + \Delta_y \mathcal{B}^-) \end{aligned} \quad (1.12)$$

Note that this form is analogous to Eqn. 1.8. The stability characteristics of the upwind-ADI scheme resemble those of the central-difference ADI presented in Section 1.2.2. The scheme is unconditionally stable, and promises optimal convergence for intermediate values of the CFL number (usually 5 to 10). At higher CFL numbers, the AF errors dominate the LHS operator and cause convergence to deteriorate.

The DDADI scheme may be written as:

$$\begin{aligned} \mathcal{D} &= I + \frac{\Delta t}{\Delta x} (\mathcal{A}_i^+ - \mathcal{A}_i^-) + \frac{\Delta t}{\Delta y} (\mathcal{B}_j^+ - \mathcal{B}_j^-) \\ \mathcal{T}_1 &= -\frac{\Delta t}{\Delta x} \mathcal{A}_{i-1}^+ + \frac{\Delta t}{\Delta x} \mathcal{A}_{i+1}^- \\ \mathcal{T}_2 &= -\frac{\Delta t}{\Delta y} \mathcal{B}_{j-1}^+ + \frac{\Delta t}{\Delta y} \mathcal{B}_{j+1}^- \end{aligned} \quad (1.13)$$

Stability characteristics for the DDADI scheme for  $CFL = 1$  and  $10$  and Mach number,  $M = 0.5$ , are given in Fig. 1.6. The scheme is observed to be stable at  $CFL = 1$ , but unstable at  $CFL = 10$ . At the lower  $CFL$ , as may be expected, the amplification factor is close to unity for low frequencies, suggesting slow convergence. Thus, in the case of ADI, the diagonal-dominant formulation has more restrictive stability compared to the standard ADI formulation. We point out that these results are for the I/III system. Stability results for the I/I system using DDADI are given in Fig. 1.7. Now, the scheme is observed to be unconditionally stable, suggesting that the earlier instability is due to the inconsistent differencing. Interestingly, for the I/I result, there is not much difference in the overall damping characteristics for the  $CFL = 10$  and  $CFL = 100$  cases (and it remains the same at much higher CFL numbers as well). Thus, although the scheme is unconditionally stable, we expect about the same convergence rate at  $CFL = \infty$  as at  $CFL = 10$ . In this case, the “freezing” of the amplification factor appears even though consistent discretization has been employed; perhaps surprisingly, we observe that this effect is characteristic of all approximate methods of inverting diagonally-dominant matrix operators encountered in CFD problems.

We pointed out that the DDADI scheme is, in fact, an alternating direction line-Jacobi relaxation procedure. It is customary with relaxation schemes to perform several sets of relaxation sweeps at each iteration level. The corresponding multi-sweep DDADI scheme may be expressed as follows (see Appendix C.2):

$$(\mathcal{D} + \mathcal{T}_1)\mathcal{D}^{-1}(\mathcal{D} + \mathcal{T}_2)(Q^{k+1} - Q^k) = -\Delta t \mathcal{R}^n - (\mathcal{D} + \mathcal{T}_1 + \mathcal{T}_2)(Q^k - Q^n) \quad (1.14)$$

where  $\mathcal{D}$ ,  $\mathcal{T}_1$  and  $\mathcal{T}_2$  are the same as defined in Eqn. 1.13. Note that we have introduced an “inner” iteration counter,  $k$ , in addition to the outer-iteration counter,  $n$ . The outer iterations correspond to the non-linear time-marching procedure represented by Eqn. 1.5, while the inner iterations correspond to multiple DDADI sweeps of the linear system in Eqn. 1.10. When the inner iterations converge,  $Q^{k+1} = Q^k$ , and the RHS of Eqn. 1.14 (which is the unfactored linear system in Eqn. 1.10) is satisfied. Then,  $Q^{n+1}$  is set equal to  $Q^k$  and the solution is advanced to the next time-step.

The overall performance of the scheme depends upon whether and how fast the inner iterations converge. Interestingly, the stability of the inner iterative procedure in Eqn. 1.14 corresponds to the stability of the I/I system since all operators involving  $Q^k$  and  $Q^{k+1}$  are first-order operators. Note that the third-order operators in  $\mathcal{R}^n$  do not influence the inner iteration stability. For the DDADI scheme, we have already determined that the I/I system is unconditionally stable, while the I/III system has more restrictive stability. Therefore, the multi-sweep DDADI procedure has the potential of using the I/I inner iterations to stabilize the I/III outer iterations.

Figure 1.8 shows overall stability for the multi-sweep DDADI scheme. At  $CFL=10$ , which is unstable for a single DDADI sweep, we observe that performing one additional DDADI sweep is sufficient to stabilize the scheme. At a much larger  $CFL = 1 \times 10^6$ , we require about 20 DDADI sweeps to stabilize the scheme. It is noteworthy that, in the latter instance, the stability result closely resembles the direct stability result given in Fig. 1.4.

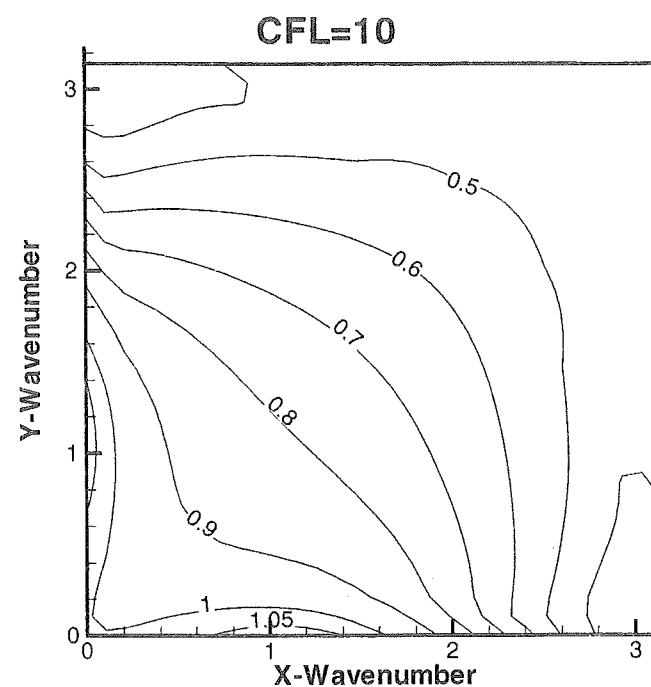
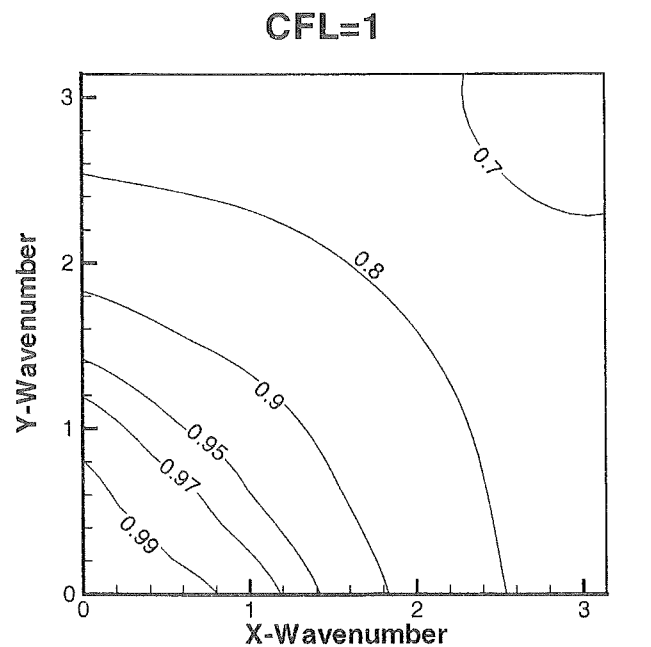


Figure 1.6: Stability Results. Euler Equations with I/III upwind differences. DDADI scheme.  $M=0.5$ .

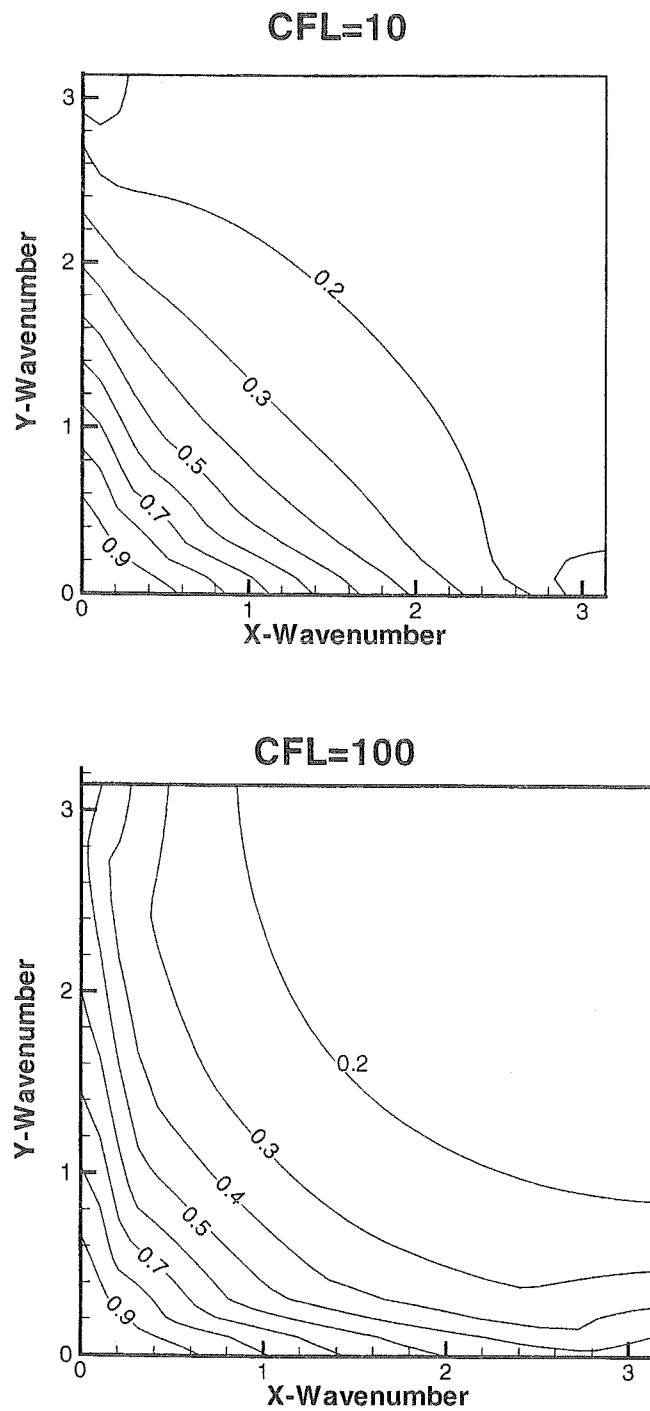
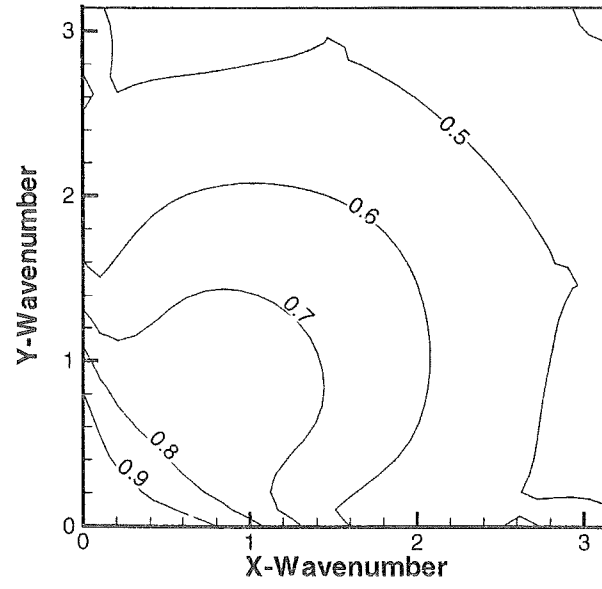


Figure 1.7: Stability Results. Euler Equations with I/I upwind differences. DDADI scheme.  $M=0.5$ .

**CFL=10, 2 DDADI sweeps**



**CFL=10<sup>6</sup>, 20 DDADI sweeps**

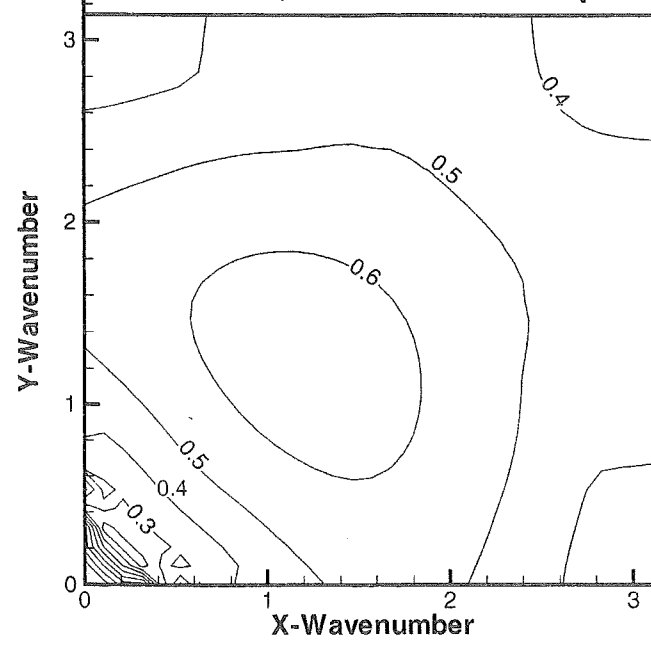


Figure 1.8: Stability Results. Euler Equations with I/III upwind differences. Multi-sweep DDADI scheme.  $M=0.5$ .

The multi-sweep DDADI scheme has enjoyed a renaissance in recent years [13, 14, 15]. It is however our experience that the multi-sweep DDADI scheme generally performs only as well as the upwind-ADI scheme. One reason for this is the fact that the inner iterations cost about the same as the outer iterations and the stability gains come at the cost of performing these expensive inner iterations. In this regard, we point out that the inner iterations are linear and do not require re-computation of the Jacobians if they can be stored. Modern parallel architectures do allow the potential for such storage and may make such multi-sweep schemes attractive. Further, Huang and Coakley [16] have introduced an interesting variant that minimizes the storage requirements of such schemes. Finally, we note that such multi-sweep iterative procedures may also be derived for the conventional (non-diagonally dominant) ADI schemes (with similar gains in stability and convergence) using a dual time-stepping procedure [17], as discussed in Section 2.4.3.

### 1.2.5 Upwind Gauss-Seidel Schemes

We turn our attention to conventional relaxation techniques such as point- and line-Gauss Seidel iterations. It is customary to perform these procedures after discretization of the fluxes, and so, they correspond to equivalent diagonally dominant factorization schemes. Using the procedure outlined in Appendix C.2, we may express the symmetric point Gauss-Scheme (SPGS) as the following AF scheme:

$$\begin{aligned} \mathcal{D} &= I + \frac{\Delta t}{\Delta x} (\mathcal{A}_i^+ - \mathcal{A}_i^-) + \frac{\Delta t}{\Delta y} (\mathcal{B}_j^+ - \mathcal{B}_j^-) \\ \mathcal{T}_1 &= -\frac{\Delta t}{\Delta x} \mathcal{A}_{i-1}^+ - \frac{\Delta t}{\Delta y} \mathcal{B}_{j-1}^+ \\ \mathcal{T}_2 &= +\frac{\Delta t}{\Delta x} \mathcal{A}_{i+1}^- + \frac{\Delta t}{\Delta y} \mathcal{B}_{j+1}^- \end{aligned} \quad (1.15)$$

Since the first operator is a lower triangular block matrix and the second operator is an upper triangular block matrix, such schemes are sometimes referred to as LU approximate factorization. In order to emphasize their diagonally dominant formulation, we designate the scheme as DDLU. We may also formulate a non-diagonally dominant variant of the scheme, but its stability properties are more restrictive than the DDLU scheme and is not considered further here.

Stability results for the DDLU scheme applied to the I/III upwind system are given in Fig. 1.9 for CFL=10. The figure shows the results for both the  $(0, \pi)$  quadrant (top plot) and the full  $(-\pi, \pi)$  range (bottom plot). Interestingly, the scheme is observed to be stable in the  $(0, \pi)$  quadrant, but is unstable in the  $(-\pi, 0)$  quadrant. The instability occurs at CFL numbers above about 5 and is initially very weak. At higher CFL numbers (not shown), the results in the first quadrant display the “freezing” that is characteristic of diagonally-dominant schemes, while the second quadrant indicates a progressively stronger instability. For the I/I upwind scheme, the DDLU scheme is unconditionally stable, which means that a multi-sweep formulation may be successfully employed to obtain

overall stability. The multi-sweep results are similar to those of the DDADI scheme and are not presented here. We further note that the DDLU scheme is a popular choice among researchers using algebraic multigrid techniques [55, 56]. In these schemes, I/III discretization is typically employed at the outer non-linear level, while DDLU is used in concert with multigrid procedures at the inner linear stage.

We may also express the line-Gauss Seidel iterations in factorization form, which we refer to as DDLGS. We can formulate two versions of the DDLGS procedure. The two-sweep version (DDLGS-2) performs symmetric line-Gauss Seidel sweeps only in the  $x$ -direction, while the four-sweep version (DDLGS-4) includes symmetric  $x$ -sweeps, followed by symmetric  $y$ -sweeps. We show the algebraic representation for only the 2-sweep version here. The reader is referred to Ref. [18] for the 4-sweep version.

The DDLGS-2 scheme may be written in the following factored form:

$$\begin{aligned}\mathcal{D} &= I + \frac{\Delta t}{\Delta x} (\mathcal{A}_i^+ - \mathcal{A}_i^-) + \frac{\Delta t}{\Delta y} (\nabla_y \mathcal{B}^+ + \Delta_y \mathcal{B}^-) \\ \mathcal{T}_1 &= -\frac{\Delta t}{\Delta x} \mathcal{A}_{i-1}^+ \\ \mathcal{T}_2 &= \frac{\Delta t}{\Delta x} \mathcal{A}_{i+1}^-\end{aligned}\tag{1.16}$$

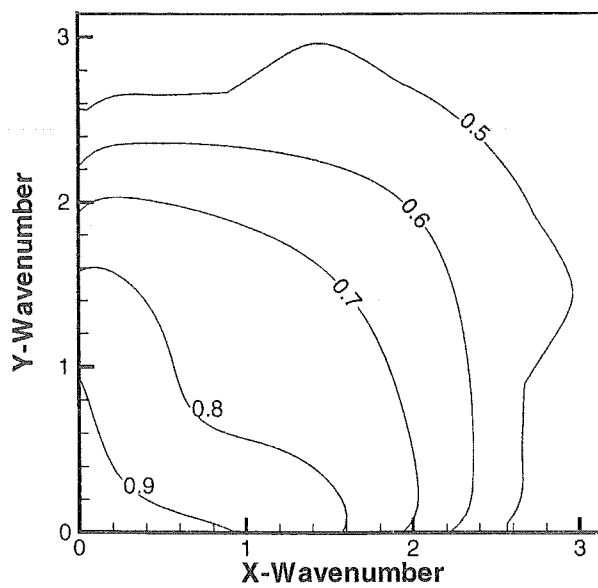
Each sweep of the DDLGS algorithms requires block tri-diagonal inversions along a line across the domain.

Figure 1.10 shows the stability result for the DDLGS-4 scheme (DDLGS-2 results are qualitatively similar). Like the other diagonally-dominant schemes, the scheme is observed to be conditionally stable, with a limiting CFL around 30. At  $CFL = 10$ , we observe that the scheme possesses excellent damping properties, particularly in the low frequency region that typically controls overall convergence rates. The  $CFL = 100$  result indicates a strong instability at low frequencies. Indeed, the source of this instability is somewhat puzzling since it is not restricted to the I/III system; rather, it is apparent in the I/I system as well. This latter result suggests that the multi-sweep version of the DDLGS schemes may not perform as well as the multi-sweep DDADI or DDLU schemes examined earlier, although dual-time procedures (Section 2.4) may be used to optimize it. In any case, the superior convergence properties at  $CFL = 10$  makes this an interesting scheme to consider for practical computations.

### 1.3 Historical Perspective on Preconditioning

We have seen that conventional time-marching algorithms face convergence difficulties at low Mach numbers because of the ill-conditioned wave speeds of the time-marching system. Similar difficulties also arise for flows in other regimes such as diffusion-dominated flows, flows in stretched grid regions (as in boundary layers), source-dominated flows (reacting flows) and unsteady flows. Even in these more complex situations, convergence problems may be traced to ill-conditioning of the controlling time-scales. For instance, in

**CFL=10, 0 to pi**



**CFL=10, -pi to pi**

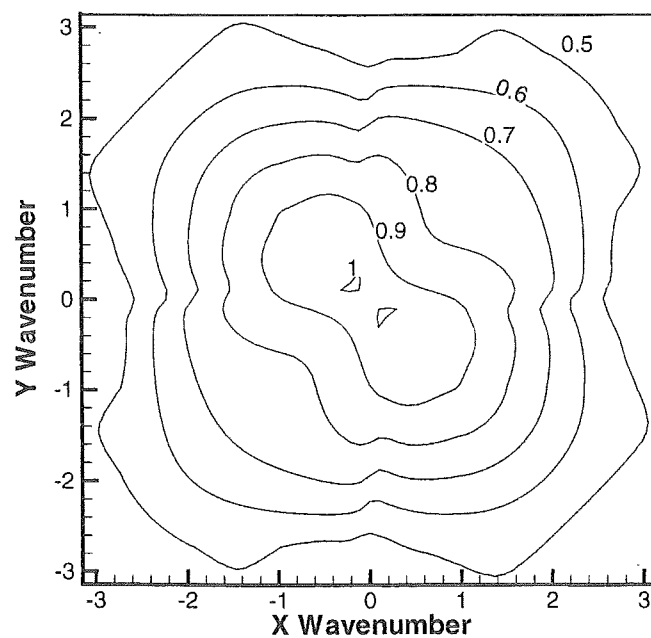


Figure 1.9: Stability Results. Euler Equations with I/III upwind differences. Point Gauss-Seidel Scheme (DDLU). CFL=10, M=0.5.

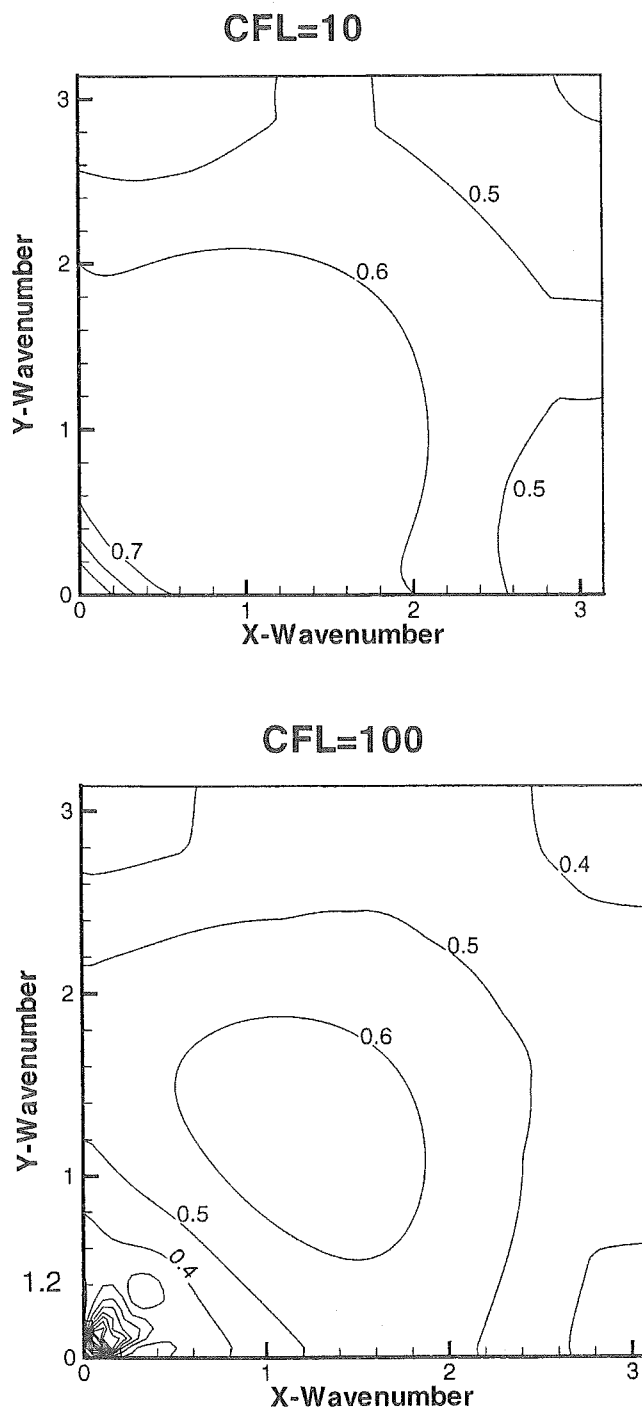


Figure 1.10: Stability Results. Euler Equations with I/III upwind differences. Four-Sweep Line Gauss-Seidel scheme.  $M=0.5$ .

the viscous-dominated limit, the relative time-scales of convection and diffusion determine the convergence rate. Time-marching algorithms are particularly conducive to analyzing such difficulties and, more importantly, for devising techniques to eliminate them. Preconditioning is the term used to define a class of time-marching algorithms, wherein the physical time-derivatives are replaced by a set of pseudo-time derivatives. The modified time-derivatives ensure attractive convergence properties by properly conditioning the controlling time-scales of the system. In recent years, preconditioning methods have gained wide acceptance and are being routinely used in a wide range of fluid dynamic computations.

In this section, we trace the historical development of preconditioning schemes. Since much of the research has focused on the low Mach number Euler equations, we review this area first. We then look at the progress made in the Navier-Stokes and high grid aspect ratio (stretched grid) problems. We next consider the unsteady problem and discuss the role that preconditioning plays in the context of time-accurate computations. Finally, we look at the research in the extension of preconditioning techniques to more complex systems such as multi-species reacting flows and multi-phase flows.

### 1.3.1 Preconditioning for the Euler Equations

An early and seminal contribution to the development of preconditioning methods was the artificial compressibility method devised by Chorin [19] for the incompressible equations. The incompressible limit of the Euler equations is particularly challenging for time-marching computations, since the density is constant. This means that the time-derivative of density drops out of the continuity equation and the time-marching system becomes singular. Further, there is no means of updating the pressure in the solution since it is no longer related to the density. Chorin addressed these difficulties by introducing a suitably scaled pressure time-derivative in the continuity equation. The new time-derivative term, referred to as artificial compressibility, renders the system non-singular and provides a direct means of updating the pressure.

The artificial compressibility system shares several characteristics with the compressible system, which make it favorable for time-marching solutions. As in the compressible case, the eigenvalues of the corresponding inviscid Jacobian are all real, thereby rendering the system hyperbolic and well-posed for time-marching. Further, this allows the use of characteristic-based procedures for upwind discretizations [7] and boundary condition formulation [20]. Moreover, the artificial compressibility system retains the signs of the acoustic and particle wave speeds, ensuring well-posedness with regard to boundary condition specification. Finally, the artificial compressibility scaling parameter ( $\beta$ ) can be selected to maintain the pseudo-acoustic speeds to be the same order as the particle speed, thereby rendering the system well-conditioned for optimal convergence. Artificial compressibility methods have been widely used for incompressible flow computations (eg., [21, 22]) and the method has been refined to allow local definitions of the  $\beta$  parameter, thereby optimizing computations in the style of local time-stepping procedures. Perhaps more importantly, the success of the artificial compressibility method has furnished the

impetus for the development of preconditioning methods for low-speed compressible flows.

A second important development that has aided the application of time-marching methods to low Mach number flows was the use of perturbation expansion procedures to obtain asymptotic forms of the compressible equations in the low speed limit. An early example of the perturbation analysis is the work of Rehm and Baum [23], which was later applied to time-marching computations of low Mach number flows by Guerra and Gustaffson [24] and by Merkle and Choi [25]. Gustaffson expanded the equations in terms of the first power of the Mach number, while Merkle and Choi used the more conventional expansion based upon the square of the Mach number. The latter technique has been applied to a number of practical problems (*eg.*, [26, 27]). Although it was not realized at the time, the perturbation method is, in fact, closely related to Chorin's method. Further, both methods share the disadvantage of being valid only in the low speed regime. In other words, the perturbation equations cannot be used for transonic flow applications or for flowfields involving a mixture of flow regimes.

The earliest examples of preconditioning methods, that are valid at all flow Mach numbers, are the works of Viviand [28], Briley *et al.* [29], Turkel [30] and Choi and Merkle [22]. Turkel [30] was the first to systematically extend Chorin's formulation to the compressible system and to derive a preconditioning method that is well-conditioned at all Mach numbers. Further, Turkel also refined Chorin's formulation by introducing a second parameter ( $\alpha$ ), which provides improved conditioning of the system. Turkel and his co-workers (*eg.*, [31, 32, 33]) have extensively tested the preconditioning system for practical aerodynamic computations.

Choi and Merkle [34] extended their previous low Mach perturbation formulation to derive a preconditioning system that is valid at all speeds. Although derived from different philosophies, the Choi-Merkle preconditioning system is closely related to Turkel's system. The major difference is that the Choi-Merkle system was derived based upon using temperature as a dependent variable (in the energy equation), while the Turkel system was derived using entropy as the dependent variable. More recently, Weiss and Smith [35] have also adapted the Choi-Merkle method by using entropy as the dependent variable. The Choi-Merkle system has also been extensively applied by several researchers (*eg.*, [36, 37, 38]).

Van Leer *et al.* [39, 40] developed an alternate preconditioning formulation that was based upon a characteristic re-scaling of the equations. A one-dimensional example of the procedure was given in Eqn. 1.3. Van Leer *et al.* extended the idea to multi-dimensions by starting from the supersonic range and then extending down to low Mach numbers. Unlike the other preconditioning methods discussed so far, their formulation introduces a preconditioning treatment of the equations in the transonic regime as well as for low Mach numbers. Further, their analysis provided an interesting physical and geometrical interpretation of the acoustic and particle wave processes. In spite of their structural differences, however, we point out that the van Leer system (at low Mach numbers) is also closely related to the Turkel and Choi-Merkle systems.

Van Leer *et al.* also observed that the low Mach number preconditioning not only improved the convergence of the system, but was also responsible for maintaining accuracy

at low speeds. Turkel [32] showed that this was due to the conditioning of the artificial dissipation terms. Ill-conditioning of the original system at low Mach numbers causes the artificial dissipation terms to become unduly large (or small in some cases) resulting in poor representation of the solution at the discrete level. The well-conditioned eigensystem corresponding to the preconditioned system rectifies this problem and ensures reliable accuracy.

Experience with using preconditioning methods for practical computations has confirmed that significant gains in convergence performance are possible at low Mach numbers. For complex problems, however, the convergence gains are sometimes accompanied by reduced robustness. In particular, the preconditioned scheme becomes unstable when local pressure disturbances are much larger than the local dynamic pressure ( $\rho u^2$ ). This is in dramatic contrast with standard compressible codes, which remain stable until the disturbances are of the order of the thermodynamic pressure. Recently, the present authors [17] have re-formulated the preconditioning procedure by introducing it at the linear solver level rather than at the non-linear level, thereby enhancing robustness to pressure fluctuations.

A related robustness issue is the instability in stagnation regions, which occurs when local variables are employed in the definition of the preconditioner. Darmofal [41] observes that the eigenvectors of the preconditioned system become nearly parallel in the low Mach number limit, suggesting singular behavior at this limit. Lee [42] notes that, in addition, the ill-defined flow angle in the vicinity of the stagnation point exacerbates the problem. The customary “fix” for the stagnation point problem is to employ the free-stream variables in the preconditioner definition, although some researchers (*e.g.*, [31]) prefer to specify a “cut-off” value in the definition. The difficulty with either of these approaches is that it becomes difficult to optimize the algorithm for more complex problems, where different flow regimes may co-exist in different sections of the flowfield. Weiss and Smith [55] have developed a pressure-gradient based cut-off that modifies the definition of the preconditioner locally in the stagnation region. Darmofal [43] has recently assessed similar procedures and has reported encouraging results. We note that the robustness and instability problems described above are common to all of the low Mach number preconditioning systems (and the artificial compressibility system), although some of the modifications to the preconditioning definition are easier to accomplish with the Turkel and Choi-Merkle systems.

Finally, we briefly discuss an alternate preconditioning strategy based upon the block-Jacobi relaxation procedure developed by Pierce and Giles [44]. The block-Jacobi preconditioning has been shown to be effective in accelerating the convergence of explicit time-marching methods, particularly when it is used in concert with multigrid techniques. The block-Jacobi preconditioner is, however, a different kind of convergence acceleration tool compared to the preconditioning methods discussed here. Specifically, it does not provide any enhancement at low Mach numbers since it does not eliminate the stiffness between acoustic and particle waves. The block-Jacobi preconditioner is, in fact, equivalent to applying block-Jacobi relaxation and its gains are due to bringing in a degree of implicitness into an otherwise explicit method. For this reason, we would not anticipate any gains

when used with an implicit solution technique such as ADI or Gauss-Seidel. Further, for explicit methods, the block-Jacobi relaxation may also be effectively combined with any of the low Mach number preconditioning strategies discussed earlier.

### 1.3.2 Preconditioning for the Navier-Stokes Equations

Early research by Choi and Merkle [25] on using the low Mach number perturbation equations for viscous flows pointed to the difficulty with using inviscid procedures for low speed, but highly viscous (low-Reynolds number) calculations. They reported improved low-Reynolds number performance when they modified the perturbation parameter by introducing a new scaling parameter ( $k$ ) to account for viscous effects. They later refined the selection of the  $k$  parameter [34] in the context of the preconditioned equations by simultaneously optimizing the acoustic time-scale and the diffusion time scale (rather than the particle convective time scale used in the inviscid case). This essentially introduces a modified definition of the preconditioning parameter ( $\epsilon$  in the Choi-Merkle system and  $\beta$  in the artificial compressibility and Turkel systems). Weiss and Smith [35] equivalently interpreted this modification in terms of a diffusion “velocity” scale.

Although the Choi-Merkle viscous modifications worked well, the precise nature of the controlling Navier-Stokes scales was not well-understood. Using a linearized analysis of the Navier-Stokes equations, the present authors [45] have shown that, at low Re numbers, the errors are controlled by acoustic wave propagation and particle wave damping. Thus, optimizing these scales ensures that all the error modes are damped in commensurate fashion. Further, they have extended the perturbation analysis to examine the equations at the viscous limit [46] and have also examined the conditioning of the artificial dissipation terms under such conditions [47].

Researchers have also attempted block-Jacobi type preconditioning methods for addressing the viscous stiffness problem at low Reynolds numbers [48, 42]. However, as in the inviscid case, the block-Jacobi method does not relieve the stiffness problem. The associated gains are, therefore, probably related to enhanced stability characteristics arising from the semi-implicit treatment of the viscous terms.

A problem related to Navier-Stokes solutions is the presence of high grid aspect ratios, which arise in high Reynolds number boundary layers and shear layers. In high Reynolds number problems, where high aspect ratio cells typically arise, the flowfield is convection-dominated in the streamwise direction and diffusion-dominated in the wall-normal direction. Buelow *et al.* [49, 50, 18] have addressed this problem in the context of several implicit schemes. They determined that high aspect ratio convergence may be optimized for line-implicit schemes, such as ADI and line-Gauss Seidel relaxation, by proper definition of the local time-step. Further, they refined the viscous preconditioning definition by accounting for viscous scales in the different coordinate directions. They were able to demonstrate convergence rates that are independent of the grid aspect ratio for two-dimensional computations; however, difficulties remain with three-dimensional high aspect ratio cells.

An alternate approach for tackling high grid aspect ratios is through the use of semi-

coarsening multigrid strategies (*e.g.*, [51, 52]). Raithby and his group [53, 54] have pioneered the application of algebraic multigrid techniques for the solution of such problems. Weiss *et al.* [55] have combined local preconditioning methods with the algebraic multigrid and demonstrated grid aspect ratio independent convergence. Recently, several researchers have obtained encouraging results with such preconditioned-multigrid approaches (*e.g.*, [44, 56]).

### 1.3.3 Preconditioning for Unsteady Problems

Unsteady compressible solutions typically involve iterative procedures to eliminate linearization and factorization errors at each physical time-step [57]. Unsteady incompressible solutions also require such “inner” iterations, except that these iterations are usually performed using a dual time-stepping formulation (see [58, 59]). Here, the physical time-derivatives are employed at the outer level to march the equations in physical time, while artificial compressibility is introduced through a second set of pseudo-time derivatives, which are then used to iteratively solve the non-linear equations at each physical time level. The dual time-stepping concept has also been applied to the low Mach number perturbation system for unsteady combustion problems [26].

For the preconditioning system, dual time procedures have been designed by Withington *et al.* [60], Shuen *et al.* [61] and the present authors [62]. While the earlier works used the same steady-state preconditioning matrix for the unsteady computations, the present authors determined that, under certain limits, the preconditioning definition should be modified to account for the presence of the physical time-derivatives. McHugh and Ramshaw [63] have analyzed the dual-time scheme for incompressible computations and reached similar conclusions. Further, we have also used perturbation expansions to study performance behaviour [46] as well as the conditioning of the dissipation terms under unsteady conditions [47]. Recently, Buelow *et al.* [64] have re-formulated the preconditioned dual-time procedure for the diagonalized implicit algorithm [6].

### 1.3.4 Preconditioning for Advanced Systems

Practical engineering computations often involve additional complexities such as non-ideal gases, multiple species, chemical reactions, turbulence, multiple-phases, plasmas, etc. Since many of these problems are characterized by low-speeds, strong diffusion effects, and unsteadiness, preconditioning offers the ideal platform for building schemes to compute such flows. Extension of the preconditioning system to reacting flows has been carried out by Shuen *et al.* [61], Withington *et al.* [60] and Venkateswaran *et al.* [36, 65]. Venkateswaran *et al.* [65] examined the numerical difficulties introduced by chemical source terms and determined that the source term eigenvalues controlled the solution behaviour during the initial, “non-linear” stages of the computation. Once the flame has been successfully established, the source terms no longer materially impact the convergence process and asymptotic, “linear” convergence rates are observed.

Extension of the preconditioning system to generalized fluids has been carried out

by Weiss *et al.* [35], Merkle *et al.* [67] and Oefelein and Yang [76]. The generalized formulation allows the same code to be used for incompressible, perfect gas and arbitrary equation of state fluids. Multi-phase formulations have been studied for homogeneous mixtures by Merkle *et al* [68] and Kunz [69], and for the complete multi-fluid system, by Kunz *et al* [70] and the present authors [71]. The full multi-fluid system is particularly interesting since the corresponding time-marching system possesses complex eigenvalues, and hence, is not well-posed for time-marching. Preconditioning offers the interesting potential of altering the system characteristics such that they become real and, therefore, well-posed for time-iterative solutions. The research in these areas is still at a relatively early stage and we anticipate further developments in the near future.

## 1.4 Overview of Contents

In this introductory chapter, we have discussed the convergence of time-marching algorithms and the need for preconditioning at low Mach numbers, low Reynolds numbers, high aspect ratios, etc. We have discussed the usefulness of stability theory to predict and understand convergence behaviour and we have employed it to examine the stability of standard implicit schemes such as ADI and Gauss-Seidel relaxation schemes. We have also presented a historical perspective on the development of preconditioning algorithms for the Euler, Navier-Stokes, unsteady and more advanced equation systems. In the following chapters, we consider each of the cases individually. We begin with the the low Mach number limit of the Euler equations in Chapter 2, and then consider the low Reynolds number limit for the Navier-Stokes equations in Chapter 3. Aspect ratio issues that arise in high-Reynolds number Navier-Stokes solutions are dealt with in Chapter 4. Unsteady Euler and Navier-Stokes solution are discussed in Chapter 5. Finally, we discuss more advanced systems, such as turbulent and multi-species, reacting flows in Chapter 6.

Throughout this text, asymptotic expansions are used to relate the behaviour of the solutions under various limiting conditions such as low Mach number, low Reynolds number and different unsteady limits. The perturbation equations are then used to fashion appropriate pseudo-time derivatives, which ensure that the terms are in balance with the important physical derivatives. A simple mathematical continuation procedure is used to link all these limits into a single function, which defines the overall preconditioning matrix. Linearized solutions of the preconditioned perturbation equations are used to verify that the dominant physical processes (such as wave propagation and damping) are indeed commensurate in magnitude, thereby providing reliable convergence behaviour over broad flow regimes.

The perturbation equations are also used to examine the conditioning of the artificial dissipation terms, which influences the overall accuracy of the computations. Both central-difference and upwind flux-difference schemes are considered. Again, we verify that the preconditioning formulation provides reliable accuracy in different flow regimes.

We also discuss practical implementation of preconditioning schemes. Eigenvalues and eigenvectors of the Navier-Stokes equations and the Reynolds-averaged, reacting Navier-

Stokes system are given in the Appendices. Stability analyses and convergence studies are used to verify the performance enhancements of the preconditioning method in the context of practical implicit schemes. Finally, we present representative examples of practical flowfield computations to demonstrate the broad applicability of the preconditioning schemes.

# Chapter 2

## Preconditioning for the Euler Equations

The primary difficulty that limits the general applicability of time-marching algorithms is the convergence degradation at low Mach numbers. As we have seen, this difficulty has its source in the widely disparate characteristic speeds of the Euler equations. Accordingly, we begin our discussion on preconditioning schemes by examining the Euler equations. We employ perturbation procedures to examine the asymptotic form of the Euler equations in the low Mach number limit and then use the analysis to identify preconditioning procedures to mitigate the problems. The resulting preconditioning system is shown to possess well-conditioned characteristic speeds irrespective of the Mach number and practical convergence studies are used to confirm the theoretical findings. Finally, we discuss additional stability and robustness issues that arise with regard to the preconditioning systems and review some potential improvements to the basic methodology.

### 2.1 Perturbation Analysis of the Low Mach Number Limit

In this section, we carry out classical perturbation expansions to examine the low Mach number form of the compressible Euler equations. We use the analysis to modify the system so that it remains well-behaved at all Mach numbers. We verify convergence properties by studying the eigenvalues of the modified system. Further, in the following section, we employ the perturbation form of the equations to investigate the formulation of artificial dissipation models as well.

#### 2.1.1 Equations of Motion

We begin with the Euler equations for a general, compressible fluid. Although our interests are primarily in multi-dimensional applications, the basic concepts are contained within the one-dimensional equations, and for notational convenience, we use this simplified set.

In general vector form, the one-dimensional Euler equations in conservation form are,

$$\frac{\partial Q}{\partial \tau} + \frac{\partial E}{\partial x} = 0 \quad (2.1)$$

The vectors  $Q$  and  $E$  have their standard definitions and are given in Appendix A.1.1. Note that we have employed the variable  $\tau$  to signify the time variable in order to emphasize our interest in obtaining steady solutions. In other words, the  $\tau$  variable may be interpreted as a *pseudo-time* variable. (We will reserve the symbol  $t$  to refer to the physical time variable.)

### Transformation of Variables

The vector  $Q$  is the traditional primary dependent variable vector for the conservative variables. For the purposes of the perturbation expansion and the derivation of the preconditioning system, it is more convenient to use an alternate primitive variable set,  $Q_p$ , for the dependent variable vector. This new vector  $Q_p$  is given as,

$$Q_p = \begin{pmatrix} p \\ u \\ T \end{pmatrix}$$

Employing the chain-rule to transform variables, Eqn. 2.1 becomes,

$$\frac{\partial Q}{\partial Q_p} \frac{\partial Q_p}{\partial \tau} + \frac{\partial E}{\partial x} = 0 \quad (2.2)$$

where

$$\frac{\partial Q}{\partial Q_p} = \begin{pmatrix} \rho_p & 0 & \rho_T \\ u\rho_p & 1 & u\rho_T \\ h_o\rho_p - (1 - \rho h_p) & \rho u & h_o\rho_T + \rho h_T \end{pmatrix}$$

The four variables  $\rho_p$ ,  $\rho_T$ ,  $h_p$  and  $h_T$  that appear in this matrix are thermodynamic quantities that describe the properties of the working fluid. The subscripts denote partial derivatives, i.e.,  $\rho_p = (\partial \rho / \partial p)_T$ , etc. These relations can be obtained directly from the equations of state,  $\rho = \rho(p, T)$  and  $h = h(p, T)$ . For a perfect gas,  $\rho_p = (1/RT)$ , while  $\rho_T = -(p/T)$ ,  $h_p = 0$  and  $h_T$  is the specific heat.

### Non-Conservative Equations

To simplify the algebra, it is easier to work with the non-conservative equations. The conservative equations given above can be converted to non-conservative form by standard techniques. The continuity equation is obtained from the first row, while the non-conservative momentum equation is obtained by subtracting  $u$  times the continuity equation from the second row. The non-conservative form of the energy equation is obtained by adding  $-h + \frac{1}{2}(u^2 + v^2)$  times the first row to the third row, and then subtracting  $u$

times the second row from the third row. These operations may be represented in compact fashion by pre-multiplying Eqn. 2.2 by the transformation matrix  $\mathcal{K}$ ,

$$\mathcal{K}\left(\frac{\partial Q}{\partial Q_p} \frac{\partial Q_p}{\partial \tau} + \frac{\partial E}{\partial x}\right) = 0 \quad (2.3)$$

where

$$\mathcal{K} = \begin{pmatrix} 1 & 0 & 0 \\ -u & 1 & 0 \\ -h + \frac{1}{2}(u^2 + v^2) & -u & 1 \end{pmatrix}$$

The resulting set of non-conservative equations are:

$$\begin{aligned} \rho_p \frac{\partial p}{\partial \tau} + \rho_T \frac{\partial T}{\partial \tau} + \frac{\partial \rho u}{\partial x} &= 0 \\ \rho \frac{\partial u}{\partial \tau} + \rho u \frac{\partial u}{\partial x} + \frac{\partial p}{\partial x} &= 0 \\ -(1 - \rho h_p) \frac{\partial p}{\partial \tau} + \rho h_T \frac{\partial T}{\partial \tau} + \rho u \left( \frac{\partial h}{\partial x} - \frac{1}{\rho} \frac{\partial p}{\partial x} \right) &= 0 \end{aligned} \quad (2.4)$$

where the last equation clearly is the transport of entropy.

### Non-Dimensionalized Equations

We now non-dimensionalize the equations of motion by introducing reference scales for all the variables,

$$L, p_r, \rho_r, T_r, h_r, u_r, \tau_r$$

Here,  $L$  represents a length scale that is characteristic of the problem, while the reference pressure,  $p_r$ , density,  $\rho_r$ , temperature,  $T_r$ , and enthalpy,  $h_r$  are taken as representative thermodynamic quantities. The reference velocity,  $u_r$ , is chosen as the oncoming or free-stream velocity. The characteristic time,  $\tau_r$ , is defined later.

The resulting non-dimensional equations are,

$$\begin{aligned} \left(\frac{L}{\tau_r u_r}\right)\left(\tilde{\rho}_p \frac{\partial p}{\partial \tau} + \tilde{\rho}_T \frac{\partial T}{\partial \tau}\right) + \frac{\partial \rho u}{\partial x} &= 0 \\ \left(\frac{L}{\tau_r u_r}\right)\rho \frac{\partial u}{\partial \tau} + \rho u \frac{\partial u}{\partial x} + \left(\frac{p_r}{\rho_r u_r^2}\right) \frac{\partial p}{\partial x} &= 0 \\ \left(\frac{L}{\tau_r u_r}\right)\left[-\left(\frac{p_r}{\rho_r h_r} - \rho \tilde{h}_p\right) \frac{\partial p}{\partial \tau} + \rho \tilde{h}_T \frac{\partial T}{\partial \tau}\right] + \rho u \frac{\partial h}{\partial x} - \left(\frac{p_r}{\rho_r h_r}\right) u \frac{\partial p}{\partial x} &= 0 \end{aligned} \quad (2.5)$$

where we have written the equations so that the coefficients of the convective terms are unity. For clarity, we have used tildes on the four properties,  $\tilde{\rho}_p$ ,  $\tilde{\rho}_T$ ,  $\tilde{h}_p$  and  $\tilde{h}_T$ , to indicate that they are non-dimensional. The non-dimensionalization is of the form,  $\tilde{\rho}_p = p_r \rho_p / \rho_r$ , etc. We note all the other terms (except the reference quantities) are also non-dimensional, but the tildes have been dropped to avoid the clutter.

The non-dimensional equations introduce three dimensionless quantities. Two of them are dimensionless pressures, the ratio of the pressure to the dynamic pressure,  $(p_r/\rho_r u_r^2)$ , and the ratio of the pressure to the other thermodynamic properties,  $(p_r/\rho_r h_r)$ . The third non-dimensional quantity is a dimensionless time, which is the ratio of the flow time to the characteristic time-step,  $(L/\tau_r u_r)$ .

### 2.1.2 Perturbation Expansion

The above non-dimensional equations provide a vantage point from which we can assess the order of magnitude of the various terms in the equations. Here, we are particularly interested in the low-speed limit, while in later sections, we will adopt the same procedure to examine regimes where diffusion and/or unsteady effects dominate.

At low speeds, the reference velocity,  $u_r$ , approaches zero so that the ratio of the dynamic pressure to the thermodynamic pressure,  $(\rho_r u_r^2/p_r)$ , is small. Accordingly, we specify the small parameter,  $\epsilon_i = \rho_r u_r^2/p_r$ , and consider the limiting form of the equations as this parameter goes to zero. (The subscript  $i$  indicates that this choice of small parameter corresponds to the inviscid system under scrutiny here.) Note that, for perfect gases, this small parameter,  $\epsilon_i = \gamma M_r^2$  [25]. This means that the limiting case of  $\epsilon_i$  approaching zero is appropriately interpreted as the low-Mach number limit.

The choice of the thermodynamic pressure as the reference pressure,  $p_r$ , is appropriate for transonic speeds and using it at low speeds enables us to extend the low-speed equations to the transonic and supersonic regimes. Taking  $p_r$  as the thermodynamic pressure also causes the second non-dimensional pressure term,  $p_r/\rho_r h_r$ , to be of order one. In other words, we define the reference enthalpy such that  $p_r/\rho_r h_r$  becomes unity. Further, we require that the non-dimensional time term also be order unity. This condition requires that the reference time scale,  $\tau_r = L/u_r$ , i.e., which is a convective time scale. Although this may appear to be an arbitrary choice, it is in fact a reasonable one for low-speed flows. Further, this selection does not affect the analysis since the non-dimensional time term multiplies all of the time-derivative terms.

Having specified a small parameter,  $\epsilon_i$ , we now consider the limiting form of the equations as  $\epsilon_i$  goes to zero. Since  $\rho_r u_r^2/p_r$  appears only in the momentum equation, it represents an appropriate place to start the perturbation expansion. Re-writing the momentum equation, we get,

$$\rho \frac{\partial u}{\partial \tau} + \rho u \frac{\partial u}{\partial x} + \frac{1}{\epsilon_i} \frac{\partial p}{\partial x} = 0 \quad (2.6)$$

We have written the equation such that the convective terms are order unity. For the equation to hold at low speeds, we must require that the pressure gradient term be balanced by the convective terms no matter how small  $\epsilon_i$  gets. In order facilitate this, we expand the pressure in a power series of  $\epsilon_i$ ,

$$p = p_0 + \epsilon_i p_1 + \dots \quad (2.7)$$

A more complete procedure would use analogous expansions for all the variables, but the results show that only the zeroth-order quantities of the remaining variables appear in the final equation. Consequently, to minimize the algebra, we perturb only the pressure.

Substituting Eqn. 2.7 into Eqn. 2.6, and retaining only the leading order terms, we obtain,

$$\rho \frac{\partial u}{\partial \tau} + \rho u \frac{\partial u}{\partial x} + \frac{1}{\epsilon_i} \frac{\partial(p_0 + \epsilon_i p_1)}{\partial x} = 0 \quad (2.8)$$

It is clear that there is no term that can balance the  $1/\epsilon_i$  term in the pressure gradient. Consequently, we conclude that,

$$\frac{\partial p_0}{\partial x} = 0 \quad (2.9)$$

That is to say, the zeroth order pressure,  $p_0$ , is independent of the spatial coordinate and can only vary in time. We will further note that, for most problems,  $P_0$  is fixed by some boundary condition, and hence, this quantity is independent of time as well. Eqn. 2.9 then implies that the zeroth order pressure does not affect the steady-state solution apart from its impact on the thermodynamics and the first-order pressure term,  $\epsilon_i p_1$ , acts like a gauge pressure. Thus, both the convective and pressure derivative terms are now of order unity.

The resulting zeroth order momentum equation contains the zeroth order velocity and density but the first-order pressure,

$$\rho \frac{\partial u}{\partial \tau} + \rho u \frac{\partial u}{\partial x} + \frac{\partial p_1}{\partial x} = 0 \quad (2.10)$$

Note that the  $\epsilon_i$  term in the pressure has been canceled by the  $1/\epsilon_i$  term that multiplies the pressure gradient term. All the terms in Eqn. 2.10 are order one and the momentum equation provides a means of updating the velocity  $u$ . However, the presence of the first-order pressure,  $p_1$ , implies that we must have a viable way of updating it from either the continuity or the energy equations. We look at these equations next.

Substituting Eqn. 2.7 into the energy equation in Eqn. 2.5, we get,

$$[-(1 - \rho \tilde{h}_p) \epsilon_i \frac{\partial p_1}{\partial \tau} + \rho \tilde{h}_T \frac{\partial T}{\partial \tau}] + \rho u \frac{\partial h}{\partial x} - \epsilon_i u \frac{\partial p_1}{\partial x} = 0 \quad (2.11)$$

Here, we have dropped the zeroth order pressure terms in both the temporal and spatial derivative terms, in keeping with our inference from Eqn. 2.9. Among the remaining time derivatives, the first-order pressure derivative is order  $\epsilon_i$ , while the time-derivative of temperature is order one. Thus, the energy equation is an equation for updating the temperature and does not provide a direct means of updating the perturbation pressure,  $p_1$ .

The only remaining equation is the continuity equation. With the above definitions, the continuity equation becomes:

$$\tilde{\rho}_p \epsilon_i \frac{\partial p_1}{\partial \tau} + \tilde{\rho}_T \frac{\partial T}{\partial \tau} + \frac{\partial \rho u}{\partial x} = 0 \quad (2.12)$$

Here again, we have dropped the zeroth-order pressure time-derivative. The first-order pressure time-derivative is of order  $\epsilon_i$ . Therefore, the continuity equation also does not provide an adequate means of updating the perturbation pressure  $p_1$ .

Note that in our analysis, we have not altered the equations in any way. We have simply analyzed the proper low Mach number limiting form and have determined that the standard unsteady equations do not possess a natural means of updating the pressure field. This is, of course, a statement of the well-known singularity problem for the incompressible equations. The advantage of deriving the above perturbation equations lies in the potential for altering the time-derivatives in such a manner as to allow updating of the pressure field. We examine the possibilities of achieving this in the following section.

### 2.1.3 Derivation of Preconditioning

The preceding analysis outlined the fundamental problem with the low Mach number limit of the Euler equations. The time-derivatives involving the perturbation pressure,  $p_1$ , become vanishingly small as  $\epsilon_i$  approaches zero and, therefore, they do not provide a reliable means of updating the pressure field. In this section, we seek to remedy this situation by modifying the artificial properties, i.e.,  $\tilde{\rho}_p$ ,  $\tilde{\rho}_T$ ,  $\tilde{h}_p$  and  $\tilde{h}_T$ , that occur in the temporal derivatives. The overall philosophy is that proper balance of the temporal and spatial derivatives in each equation would ensure efficient convergence of the system.

Time-derivatives of  $p_1$  appear in the continuity and energy equations. Re-writing the continuity equation, by replacing the property,  $\tilde{\rho}_p$ , by  $\tilde{\rho}'_p$ , we get,

$$\tilde{\rho}'_p \epsilon_i \frac{\partial p_1}{\partial \tau} + \tilde{\rho}_T \frac{\partial T}{\partial \tau} + \frac{\partial \rho u}{\partial x} = 0 \quad (2.13)$$

To obtain an update relation for  $p_1$  from this equation, we must require that the time term be order one or the coefficient of the time term be  $1/\epsilon_i$ . We enforce this condition by setting,

$$\tilde{\rho}'_p = \frac{k_i}{\epsilon_i} = \frac{k_i p_r}{\rho_r u_r^2} \quad (2.14)$$

where  $k_i$  is a constant of order one. In dimensional form, this requires that the artificial property coefficient be equal to  $\rho'_p = k_i/u_r^2$ .

We note that the physical property,  $\rho_p$ , represents the reciprocal of the isothermal sound speed squared. For an ideal gas, the artificial property  $\rho'_p$  may equivalently be expressed as  $\rho'_p = k_i \rho_p / \gamma M_r^2$ , where  $\rho_p = 1/RT$  and  $M_r$  is the reference Mach number. This form is particularly well-suited for compressible codes since it approaches the standard equations near the transonic limit. Further, for incompressible flows, we note that  $\rho'_p$  is analogous to the reciprocal of Chorin's artificial compressibility parameter,  $\beta$ .

With the re-scaling of the  $\tilde{\rho}_p$  term, the system is now well-posed and well-conditioned for time marching solutions. The other property functions need not be altered. In previous work [25],  $\tilde{\rho}_T$  was replaced by  $\tilde{\rho}'_T = 0$ , which removes time-derivative of temperature from the continuity equation. While this does not affect the overall convergence characteristics, it does alter the form of the equations as we approach transonic flow. Consequently, we

prefer to retain the original form of  $\tilde{\rho}_T$  in the present formulation (*i.e.*,  $\tilde{\rho}'_T = \tilde{\rho}_T$ ). In the energy equation, it is possible to re-scale  $\tilde{h}_p$  to make the pressure time-derivative term to be order one. The authors are not aware of any benefits of doing this, and so, both the enthalpy derivatives are retained in their original forms.

In closing, we also point out that the above development could equivalently be carried out using the entropy variable instead of temperature. This alternate choice results in the property,  $\rho_p$ , becoming the derivative of density at constant entropy and, therefore, the artificial property,  $\rho'_p$  may be interpreted as scaling the isentropic sound speed squared rather than the isothermal sound speed squared. This choice corresponds to the preconditioning systems used by Turkel [30] and Weiss and Smith [35]. The differences between the temperature and entropy systems are minor and, at any rate, can be readily incorporated in the definition of the scaling factor  $k_i$  in Eqn. 2.14 as discussed in Section 2.2.2.

### 2.1.4 Characteristics of the Preconditioned System

The low Mach number perturbation equations may be expressed in vector form,

$$\tilde{\Gamma}_p \frac{\partial \tilde{Q}_p}{\partial \tau} + \tilde{A} \frac{\partial \tilde{Q}_p}{\partial x} = 0 \quad (2.15)$$

where

$$\tilde{\Gamma}_p = \begin{pmatrix} \tilde{\rho}'_p \epsilon_i & 0 & \tilde{\rho}_T \\ 0 & \rho & 0 \\ -(1 - \rho \tilde{h}_p) \epsilon_i & 0 & \rho \tilde{h}_T \end{pmatrix} \quad \tilde{A} = \begin{pmatrix} u \tilde{\rho}_p \epsilon_i & \rho & u \tilde{\rho}_T \\ 1 & \rho u & 0 \\ -(1 - \rho \tilde{h}_p) \epsilon_i & 0 & \rho u \tilde{h}_T \end{pmatrix}$$

Note that in the above equation, all the terms are order unity with the exception of those involving the perturbation parameter,  $\epsilon_i$ . The term time-derivative of the continuity equation becomes order one when we define the artificial property  $\tilde{\rho}'_p$  appropriately. This leaves the spatial derivative in continuity and the spatial and temporal derivative terms in the energy equation (which have the coefficient  $(1 - \rho \tilde{h}_p) \epsilon_i$ ). Clearly, these terms may be dropped from the equation, but are retained in order to extend the formulation to all speeds. This is discussed in the next section.

In this section, we examine the eigenvalues of the perturbation system in Eqn. 2.15 in order to verify that they are indeed well-conditioned. For this purpose, we will in fact drop the small terms in the continuity and energy equations since this simplifies the algebra and elucidates the results. The corresponding eigenvalues are  $u$  and  $\lambda_{\pm}$ , which are defined as,

$$\lambda_{\pm} = \frac{1}{2} \left[ u \pm \sqrt{u^2 + \frac{4}{\epsilon_i \tilde{\rho}'_p}} \right] \quad (2.16)$$

When preconditioning is not used, in the  $\epsilon_i \rightarrow 0$  limit,  $\tilde{\rho}'_p$  is order one and the acoustic eigenvalues become large because of the  $1/\epsilon_i$  term. The system is then ill-conditioned leading to the convergence difficulties outlined in Chapter 1. When preconditioning is

introduced,  $\tilde{\rho}'_p$  is order  $1/\epsilon_i$ . Therefore, the acoustic eigenvalues become the same order as the particle velocity and the system becomes well-conditioned.

It is also noteworthy that apart from the magnitude of the acoustic eigenvalues, the perturbation/preconditioning procedure retains the essential character of the Euler equations. The eigenvalues are all real, indicating that the system is hyperbolic in nature. Further, two of the eigenvalues are positive (for positive  $u$ ) and one is negative and, therefore, the signs of the original eigenvalues are also preserved.

### 2.1.5 Analysis of Artificial Dissipation Models

Artificial dissipation is essential in CFD algorithms to eliminate the high wavenumber modes in the solution. Artificial dissipation models may be broadly classified into two families. The first family is associated with central-differenced schemes [72], wherein the dissipation is added as a conscious, explicit step through the introduction of higher-order derivative terms. The second family is associated with upwind schemes, where the dissipation is an inherent part of the spatial discretization. It is important to recognize that the upwind systems may equivalently be represented by a combination of central differencing and additional dissipation terms.

We have hitherto discussed the convergence of time-marching algorithms under low Mach number conditions and how preconditioning may be employed to eliminate the difficulties. More recently, there has been a realization that preconditioning is also important for ensuring an accurate representation of computational solutions under low Mach number conditions [39, 32]. The accuracy problem arises because of the formulation of artificial dissipation terms and exists for both central and upwind representations. In this regard, the low Mach perturbation equations provide an excellent basis for assessing artificial dissipation terms as well. In particular, it enables us to examine the forms of these terms as we approach low Mach numbers. We first consider standard artificial dissipation models used with central-difference schemes and then study the inherent dissipation contained in upwind flux-difference procedures.

#### Central-Difference Schemes

We re-write Eqn. 2.15 with a standard fourth-order scalar dissipation term added,

$$\tilde{\Gamma}_p \frac{\partial \tilde{Q}_p}{\partial \tau} + \tilde{A} \frac{\partial \tilde{Q}_p}{\partial x} = \epsilon_e^4 \Delta x^3 |a_r| \tilde{\Gamma}_p \frac{\partial^4 \tilde{Q}_p}{\partial x^4} \quad (2.17)$$

Here,  $\epsilon_e^4$  is the dissipation coefficient,  $a_r$  is a scaling velocity scale and  $\Delta x^3$  represents the grid spacing. We note that the typical choice of the velocity scale is the spectral radius of the system Jacobian.

The dissipation terms in the continuity, momentum and energy equations take the following form:

$$AD_{\text{cont}} = \epsilon_e^4 \Delta x^3 |a_r| [\tilde{\rho}'_p \epsilon_i \frac{\partial^4 p_1}{\partial x^4} + \tilde{\rho}_T \frac{\partial^4 T}{\partial x^4}]$$

$$AD_{\text{mom}} = \epsilon_e^4 \Delta x^3 |a_r| \rho \frac{\partial^4 u}{\partial x^4} \quad (2.18)$$

$$AD_{\text{energy}} = \epsilon_e^4 \Delta x^3 |a_r| \rho \tilde{h}_T \frac{\partial^4 T}{\partial x^4}$$

where we have dropped the small  $\epsilon_i$  terms in the energy equation.

We require that the coefficient of the artificial dissipation terms be order of one to keep the dissipation bounded and well-behaved in the low Mach limit. In the momentum equation, for instance, the relevant coefficient is the velocity scale,  $|a_r|$ . If  $a_r$  is selected to be the acoustic eigenvalue corresponding to the original system (see Eqn. 2.16), its magnitude would scale as  $1/\sqrt{\epsilon_i}$  (or  $1/M$  for the ideal gas system). This is clearly much greater than unity in the limit as  $\epsilon_i$  tends to zero. On the other hand, if  $a_r$  is chosen according to the eigenvalues of preconditioned system, its magnitude scales as the particle velocity,  $u$ , which is order one.

For the continuity equation, the coefficient of the fourth-order pressure derivative is given as,  $|a_r| \tilde{\rho}_p \epsilon_i$ . In the low Mach limit without preconditioning,  $\tilde{\rho}_p' = \rho_p$ ,  $|a_r|$  goes to  $1/M$ ,  $\tilde{\rho}_p$  is order one, and  $\epsilon_i$  goes as  $M^2$ . Therefore, the dissipation coefficient scales as  $M$ . In other words, it becomes disappearingly small and, under such conditions, the pressure field would show odd-even splitting errors in the solution. At the same time, in the momentum and energy equations, where the coefficients of the dissipation terms depend upon  $|a_r|$ , the dissipation scales as  $1/M_r$ , leading to excessive numerical dissipation. When preconditioning is used,  $\tilde{\rho}_p' = k_i/\epsilon_i$  and  $a_r$  is order one, which means that the dissipation coefficients in all the equations are order one and well-behaved. Therefore, we may conclude that the dissipation terms are well-behaved if the preconditioned characteristics are employed in their formulation and are poorly behaved when they are not.

### Upwind Flux-Difference Schemes

An upwind flux-difference scheme applied to Eqn. 2.15 would correspond to the addition of matrix dissipation terms as outlined in Appendix C.1. The first-order upwind representation takes the following form,

$$\tilde{\Gamma}_p \frac{\partial \tilde{Q}_p}{\partial \tau} + \tilde{A} \frac{\partial \tilde{Q}_p}{\partial x} = \frac{\Delta x}{2} \tilde{\Gamma}_p |\tilde{\Gamma}_p^{-1} \tilde{A}| \frac{\partial^2 \tilde{Q}_p}{\partial x^2} \quad (2.19)$$

where the terms are written in non-conservative form for simplicity.

For the system in Eqn. 2.15, the matrix dissipation is given by,

$$\tilde{\Gamma}_p |\tilde{\Gamma}_p^{-1} \tilde{A}| = \begin{pmatrix} \frac{2}{S} & \frac{\rho u}{S} & u \tilde{\rho}_T \\ \frac{u}{S} & \frac{\rho}{2S} (u^2 + S^2) & 0 \\ 0 & 0 & \rho u \tilde{h}_T \end{pmatrix} \quad (2.20)$$

where  $S = \sqrt{u^2 + \frac{4}{\tilde{\rho}_p \epsilon_i}}$ . In the low Mach limit,  $S$  tends to  $1/\epsilon_i$  or  $1/M$  when preconditioning is not employed. All other terms in Eqn. 2.20 are order unity. Examining the matrix dissipation coefficient, we can see that the (2, 2) entry scales as  $1/M$ , signifying

excess dissipation in the momentum equation. On the other hand, the (1, 1) scales as  $M$ , suggesting that the pressure field does not possess adequate dissipation. When preconditioning is used,  $\mathcal{S}$  is order one and, therefore, all the terms in the dissipation matrix are well-proportioned and good accuracy should be obtained at all Mach numbers. We note that these conclusions are, in fact, the same as those for the central difference scheme.

The above findings are readily confirmed by practical computations, which testify to the usefulness of the perturbation procedure for such assessments. In later chapters, we will employ similar perturbation techniques to examine both convergence and accuracy issues for the Navier-Stokes equations and for unsteady computations.

### 2.1.6 Complete Preconditioned Equations

In the above sections, we have developed the appropriate preconditioning system after examining the low Mach number asymptotic form of the Euler equations. In this section, we re-work our way back to the dimensional Euler equations in conservative form. In particular, we will take care that the system remains applicable for all flow regimes—low Mach number, transonic and supersonic.

We firstly remove the perturbation parameter from the equations by re-defining the perturbation pressure to be  $P_1 = \epsilon_i p_1$ . In other words, we re-write the pressure,  $p = p_0 + P_1$ . We then re-write the equations in dimensional form,

$$\begin{aligned} \rho'_p \frac{\partial P_1}{\partial \tau} + \rho_T \frac{\partial T}{\partial \tau} + \frac{\partial \rho u}{\partial x} &= 0 \\ \rho \frac{\partial u}{\partial \tau} + \rho u \frac{\partial u}{\partial x} + \frac{\partial P_1}{\partial x} &= 0 \\ -(1 - \rho h_p) \frac{\partial P_1}{\partial \tau} + \rho h_T \frac{\partial T}{\partial \tau} + \rho u \left( \frac{\partial h}{\partial x} - \frac{1}{\rho} \frac{\partial p_1'}{\partial x} \right) &= 0 \end{aligned} \quad (2.21)$$

with the stipulation that  $\rho'_p = k_i/u^2$  for subsonic flow and  $\rho'_p = \rho_p$  for supersonic flow. This preconditioned system corresponds to the standard equations in non-conservative form (Eqn. 2.4) with the exception of the introduction of the artificial property,  $\rho'_p$  and the use of the perturbation pressure,  $P_1$ , in the pressure derivatives. We note that the latter step is important because the thermodynamic pressure,  $p_0$ , is typically orders of magnitude larger than the perturbation or dynamic pressure,  $P_1$ , at low speeds. In this manner, it is possible to retain sufficient accuracy in the computation of pressure gradients without the deleterious influence of machine round-off. Finally, we note that there is no stipulation that the ‘perturbation’ pressure be small. Hence, these equations hold for transonic conditions as well and, in fact, they revert to the standard compressible system when the Mach number is greater than or equal to one.

We may write Eqn. 2.21 in vector notation,

$$\Gamma_p^{nc} \frac{\partial Q_p}{\partial t} + \mathcal{K} \frac{\partial E}{\partial x} = 0 \quad (2.22)$$

where

$$\Gamma_p^{nc} = \begin{pmatrix} \rho'_p & 0 & \rho_T \\ 0 & \rho & 0 \\ -(1 - \rho h_p) & 0 & \rho h_T \end{pmatrix}$$

where the superscript *nc* signifies the non-conservative form.

Pre-multiplying Eqn. 2.22 by the transformation matrix  $\mathcal{K}^{-1}$ , we may obtain the conservative form of the preconditioned equations,

$$\Gamma_p \frac{\partial Q_p}{\partial \tau} + \frac{\partial E}{\partial x} = 0 \quad (2.23)$$

where

$$\Gamma_p = \mathcal{K}^{-1} \Gamma_p^{nc} = \begin{pmatrix} \rho'_p & 0 & \rho_T \\ u\rho'_p & 1 & u\rho_T \\ h_o\rho'_p - (1 - \rho h_p) & \rho u & h_o\rho_T + \rho h_T \end{pmatrix}$$

which is the form of the preconditioning matrix with the Euler equations written in their standard conservative form.

## 2.2 Implementation of the Preconditioning System

Having derived the preconditioning system for low Mach numbers, in this section, we discuss the formulation of the preconditioning system for practical computations. We begin by presenting the preconditioned equations in multi-dimensions. We then discuss the definition of the preconditioning parameter and go on to present the eigenvalues and eigenvectors of the system. Finally, we compare our preconditioning formulation with the van Leer and Turkel systems.

### 2.2.1 Multi-Dimensional Preconditioning System

The two-dimensional preconditioned Euler equations in vector form may be expressed as,

$$\Gamma_p \frac{\partial Q_p}{\partial \tau} + \frac{\partial E}{\partial x} + \frac{\partial F}{\partial y} = 0 \quad (2.24)$$

where

$$Q_p = \begin{pmatrix} p \\ u \\ v \\ T \end{pmatrix} \quad \Gamma_p = \begin{pmatrix} \rho'_p & 0 & 0 & \rho'_T \\ u\rho'_p & \rho & 0 & u\rho'_T \\ v\rho'_p & 0 & \rho & v\rho'_T \\ h_o\rho'_p - (1 - \rho h_p) & \rho u & \rho v & h_o\rho_T + \rho h_T \end{pmatrix}$$

The inviscid flux vectors  $E$  and  $F$  are given in Appendix A.1.2. Note that for code implementation, we typically replace the pressure  $p$  as  $p_0 + P_1$  (where  $p_0$  is constant and is usually the some reference pressure such as the “back” pressure) as discussed in Section 2.1.6). Essentially, this replaces the pressure in  $Q_p$  and in the pressure gradient

terms with the perturbation pressure  $P_1$ , thereby enhancing the computational accuracy under low Mach number conditions.

In the above equation, we have chosen to retain the primitive variable set,  $Q_p$ , as the dependent variable in Eqn. 2.23. This choice is convenient for general fluids with equations of state written in terms of the pressure and temperature. Further, it is advantageous for multi-species reacting systems since reaction rates are also typically known in terms of temperature and pressure. Finally, we note that  $Q_p$  is the same as the vector that appears in the viscous terms (see Appendix A.1.2). This choice of the dependent variable then obviates the need to transform the diffusion terms from  $Q_p$  to  $Q$ . For these reasons, we prefer this choice for implementation in the computational code.

In some instances, particularly when preconditioning capability is being added to an existing code, it may be desirable to use the conservative variables. Transformation of the present system to the conservative variables,  $Q$ , may be accomplished by applying the chain-rule. The system then becomes,

$$\Gamma_c \frac{\partial Q}{\partial \tau} + \frac{\partial E}{\partial x} + \frac{\partial F}{\partial y} = 0 \quad (2.25)$$

Here,  $\Gamma_c = \Gamma_p \partial Q_p / \partial Q$ . For low Mach calculations, where it is desirable to use  $P_1$  instead of the full pressure, we would also need to introduce a perturbation density ( $\rho = \rho_0 + \rho_1$ , where  $\rho_0$  is constant) to maintain accuracy in the density update. The rest of the present development may be applied in a straightforward manner to this alternate form of the system.

The preconditioning matrix in Eqn. 2.24 has two scaling parameters,  $\rho'_p$  and  $\rho'_T$ . When these parameters take on their standard values,  $\rho_p$  and  $\rho_T$  respectively, we get the original (non-preconditioned) system. For purposes of preconditioning,  $\rho'_p$  is the important parameter, which we designate as the preconditioning parameter. Following the earlier derivation for the 1D system, we select this parameter to be proportional to the inverse of the local velocity squared or  $1/V^2$ , where  $V = \sqrt{u^2 + v^2}$ . The precise definition is considered in the following section. The second parameter,  $\rho'_T = \delta \rho_T$ , where  $\delta = 0$  yields the original Choi-Merkle system [34], and  $\delta = 1$  yields the variant suggested by Weiss and Smith. The latter choice is also equivalent to the Turkel system with  $\alpha = 0$  [30].

### 2.2.2 Eigenvalues and Definition of Preconditioning Parameter

The eigenvalues of the preconditioned system in Eqn. 2.24 are given by the eigenvalues of  $\Gamma_p^{-1} A_p$ , where the inviscid Jacobian is  $A_p = \partial E / \partial Q_p$ . The eigenvalues are,  $u$ ,  $\lambda_+$  and  $\lambda_-$ , the latter two being the pseudo-acoustic eigenvalues, which are given by:

$$\lambda_{\pm} = \frac{1}{2} \left[ u \left( 1 + \frac{d}{d'} \right) \pm \sqrt{u^2 \left( 1 - \frac{d}{d'} \right)^2 + 4 \frac{\rho h_T}{d'}} \right] \quad (2.26)$$

where

$$d = \rho h_T \rho_p + \rho_T (1 - \rho h_p)$$

and

$$d' = \rho h_T \rho'_p + \rho'_T (1 - \rho h_p)$$

Note that when  $d' = d$ , we obtain the standard, non-preconditioned system and the acoustic eigenvalues should equal  $u \pm c$ . It is thereby evident that the isentropic sound speed squared,  $c^2 = (\rho_p)_s$ , is given by  $\rho h_T/d$ , which for ideal gases is  $\sqrt{\gamma RT}$ .

The ratio  $\rho h_T/d'$  may be interpreted as the artificial sound speed squared, introduced by the preconditioning. This artificial speed may be defined as,

$$\frac{\rho h_T}{d'} = V_p^2 \quad (2.27)$$

which yields,

$$\rho'_p = \frac{1}{V_p^2} - \frac{\rho'_T (1 - \rho h_p)}{\rho h_T}$$

Here,  $V_p = \text{Min}(V_{inv}, c)$ , where  $V_{inv} = \sqrt{u^2 + v^2}$ . In other words, the preconditioning sets the artificial sound speed equal to the magnitude of the particle velocity for subsonic flow and to the physical sound speed for supersonic flow. The original system is therefore restored for supersonic flow. For  $\rho'_T = \rho_T$ , Eqn. 2.26 is the same as the definition used in [35], while for  $\rho'_T = 0$ , it is the same as that in [34].

In the case of compressible flows, where the isentropic sound speed is finite, we note that the ratio  $d/d' = M_p^2$ , where we may equivalently write  $M_p = \text{Min}(M_{inv}, 1)$  and  $M_{inv} = \sqrt{u^2 + v^2}/c$ . Thus, we may re-write the eigenvalues as,

$$\lambda_{\pm} = \frac{1}{2}[u(1 + M_p^2) \pm \sqrt{u^2(1 - M_p^2)^2 + 4M_p^2 c^2}] \quad (2.28)$$

We may also express  $\rho'_p = 1/\epsilon_p c^2$ , where  $\epsilon_p$  is defined as,

$$\epsilon_p = \frac{M_p^2}{1 - M_p^2 \frac{\rho'_T (1 - \rho h_p)}{d}} \quad (2.29)$$

For ideal gases,  $\rho_p = 1/RT$ ,  $\rho_T = -\rho/T$ ,  $h_p = 0$  and  $h_T = C_p$ , the definition of  $\epsilon_p$  becomes,

$$\epsilon_p = \frac{M_p^2}{1 + \delta(\gamma - 1)M_p^2}$$

which is the expression given in [34] and [17]. By examining the eigenvalues, we note that, in the limit that  $M \rightarrow 0$ , the condition number (ratio of the maximum to minimum eigenvalue) for this system is about 2.6.

For incompressible flow, where the sound speed given by  $\rho h_T/d = \infty$ , the preconditioning velocity parameter,  $V_p$ , is always set to the particle velocity. Further, since  $d/d' = 0$ , the acoustic eigenvalues become,

$$\lambda_{\pm} = \frac{1}{2}[u \pm \sqrt{u^2 + 4V_p^2}] \quad (2.30)$$

Also, note that  $\rho'_p = 1/\beta = 1/V_p^2$  and  $\rho'_T = \rho_T = 0$ .  $\beta$  is Chorin's artificial compressibility parameter [19].

### 2.2.3 Eigenvector Matrices and Flux-Difference Schemes

Practical implementation of preconditioning in Euler codes requires the eigenvector matrices for implementation of characteristic boundary procedures and for the derivation of matrix dissipation terms that are used in upwind flux-difference schemes. Eigenvector matrices for the preconditioned equations in generalized coordinates are given in Appendix B.2. The upwind flux difference formulation is summarized in Appendix C.1.

### 2.2.4 Comparison to Turkel and Van Leer Systems

Before closing this section on preconditioning implementation, we briefly compare the preconditioning system developed here with those suggested by Turkel [30] and Van Leer [39]. For simplicity, we restrict ourselves to the perfect gas case. While we traditionally prefer to express our system in the  $Q_p$  variables, Turkel and van Leer typically make different variable choices. For the sake of uniformity, however, we give all the systems in the  $Q_p$  variables.

The preconditioning system developed here may be written as follows for a perfect gas,

$$\Gamma_p = \begin{pmatrix} \frac{1}{\epsilon_p c^2} & 0 & 0 & -\frac{\rho}{T} \delta \\ \frac{u}{\epsilon_p c^2} & \rho & 0 & -\frac{\rho u}{T} \delta \\ \frac{v}{\epsilon_p c^2} & 0 & \rho & -\frac{\rho v}{T} \delta \\ \frac{h_o}{\epsilon_p c^2} - 1 & \rho u & \rho v & -\frac{\rho h_o}{T} \delta + \rho C_p \end{pmatrix} \quad (2.31)$$

where  $\epsilon_p = M_p^2/[1 + \delta(\gamma - 1)M_p^2]$ .

The Turkel system for a perfect gas is given by,

$$\Gamma_{turkel} = \begin{pmatrix} \frac{1}{\epsilon_p c^2} & 0 & 0 & -\frac{\rho}{T} \\ \frac{u}{\epsilon_p c^2} + \frac{\alpha u}{M_p^2 c^2} & \rho & 0 & -\frac{\rho u}{T} \\ \frac{v}{\epsilon_p c^2} + \frac{\alpha v}{M_p^2 c^2} & 0 & \rho & -\frac{\rho v}{T} \\ \frac{h_o}{\epsilon_p c^2} + \frac{\alpha(u^2+v^2)}{M_p^2 c^2 - 1} & \rho u & \rho v & -\frac{\rho h_o}{T} + \rho C_p \end{pmatrix} \quad (2.32)$$

where  $\epsilon_p$  and  $M_p$  are defined similarly. We note that the Turkel system is the same as the Choi-Merkle system for  $\delta = 1$  (in the Choi-Merkle system) and for  $\alpha = 0$  (in the Turkel system). The definition of  $\alpha$  is given as  $1 + M_p^2$  in [30]. In theory, the introduction of  $\alpha$  improves the condition number to unity (from about 2.6) at the low Mach limit. However, significant convergence enhancements have not been demonstrated in practice.

The Van Leer system for a perfect gas is given as,

$$\Gamma_{vanleer} = \begin{pmatrix} \frac{1}{\epsilon'_p c^2} & \frac{\rho C}{cM} & 0 & -\frac{\rho}{T} \\ \frac{u}{\epsilon'_p c^2} + \frac{C}{\alpha M} & \frac{\rho u C}{cM} + \rho(C^2 + \frac{S^2}{\beta}) & \frac{\rho u S}{cM} + \rho C S(1 - \frac{1}{\beta}) & -\frac{\rho u}{T} \\ \frac{v}{\epsilon'_p c^2} + \frac{S}{\alpha M} & \frac{\rho v C}{cM} + \rho C S(1 - \frac{1}{\beta}) & \frac{\rho v S}{cM} + \rho(S^2 + \frac{C^2}{\beta}) & -\frac{\rho v}{T} \\ \frac{h_o}{\epsilon'_p c^2} & \rho u + \frac{\rho h_o C}{cM} & \rho v + \frac{\rho h_o S}{cM} & \rho C_p - \frac{\rho h_o}{T} \end{pmatrix} \quad (2.33)$$

where, for subsonic flow, we have,

$$\epsilon'_p = \frac{M^2}{(1 + (\gamma - 1)M^2 + \sqrt{1 - M^2})} \quad \beta = \sqrt{1 - M^2}$$

and

$$C = \frac{u}{\sqrt{u^2 + v^2}} \quad S = \frac{v}{\sqrt{u^2 + v^2}}$$

Clearly, the van Leer system possesses significant structural differences over the Turkel and Choi-Merkle systems. Note, however, that the significant (1,1) term is scaled by  $1/M^2$  as it is in all of the preconditioning systems studied here. Recall that the perturbation analysis revealed that this is the crucial control that must be exercised at the low Mach limit. Thus, all the preconditioning systems are philosophically related and “work” for the same basic reasons.

We note that the van Leer system, like Turkel’s matrix with the  $\alpha$  terms, also possesses a condition number of unity at the low Mach number limit. While specific performance improvements over the other systems have not been reported in this regime, the tighter conditioning may be advantageous when explicit algorithms are employed. Implicit algorithms usually operate at higher CFL numbers and tend not to be as sensitive to small changes in the condition number.

The advantage with the van Leer system is that its formulation also allows eigenvalue control in the transonic regime to relieve the stiffness caused by the  $u - c$  eigenvalue. Convergence improvements in the transonic regime have been demonstrated by [40] for explicit algorithms. Again, we anticipate that the gains would be relatively modest with implicit algorithms. Further, the transonic stiffness is usually not a major problem since, in typical transonic computations, only a few grid points are close to a Mach number of unity. For these reasons, the Choi-Merkle and Turkel preconditioners have been used more widely for practical computations. Moreover, the additional complexity of the van Leer system makes it more difficult to manipulate, particularly with respect problems with the stagnation point (see Section 2.4), viscous-dominated flows (see Chapter 3) and unsteady flows (see Chapter 5).

## 2.3 Stability and Convergence Studies

In this section, we check the performance of the preconditioning system in practice. We first do stability analyses of the system for representative central and upwind schemes. We then verify our stability findings by performing simple diagnostic computations using a two-dimensional preconditioned Euler code.

### 2.3.1 Stability Results

Stability results using the central-difference ADI scheme are given in Fig. 2.1 for  $M = 0.1$  and  $M = 0.001$ . In both cases, we select  $CFL_{\lambda_3} = 5$ , which is the CFL corresponding

to the  $u + c$  eigenvalue for the preconditioned system. Because all the CFL numbers are of comparable magnitudes, this selection ensures that all error modes are handled optimally. Indeed, for both low Mach number cases, the stability results show reasonably good damping properties throughout the wavenumber domain. The amplification factor plot is, in fact, independent of the Mach number and is also very similar to the  $M = 0.5$  results shown in Fig. 1.2. Also, note the dramatic improvement when compared with the low Mach number results using the original system (Fig. 1.3). Finally, we remark that just as in the transonic case, the ADI scheme possesses an optimum CFL, that is typically in the range of 5 to 10. At lower CFL numbers, the slower wave speeds lead to reduced damping, while at higher CFL numbers, the influence of the AF error terms cause the amplification factor to approach unity.

Stability results for the upwind-DDLGS4 scheme (discussed in Section 1.2.5) are given in Fig. 2.2. Here, results are shown for  $M = 0.001$  with and without low Mach number preconditioning. When preconditioning is not used, the original Euler solver provides little or no damping over the entire wavenumber domain. This is a consequence of choosing  $CFL_{u+c} = 10$ , an optimal choice for transonic flow (see Fig. 1.10), but one that leads to sub-optimal values for the particle CFL numbers ( $CFL_u$  and  $CFL_v$ ) at low Mach numbers. On the other hand, when preconditioning is used, the stability plot for  $CFL_{\lambda_3} = 10$  shows excellent damping over the entire wavenumber space. Indeed, the latter set of results are very similar to the results for the original scheme under transonic conditions given in Fig. 1.10.

These stability results verify that our derivation of preconditioning system from perturbation theory indeed provides significant convergence benefits in the context of a practical CFD algorithm. In the following section, we further test these concepts by carrying out representative computations using a preconditioned CFD code.

### 2.3.2 Convergence Studies

We consider convergence results for simple model problems to verify the capability of the preconditioning method for computing low Mach number flows. Convergence studies of more practical problems are presented in Chapter 4. Specifically, we consider uniform inviscid flow in a straight duct, with constant mean flow as the desired steady-state solution. We commence the computations by specifying an arbitrary distribution of error in the velocity field as the initial condition and then track the convergence of the solution as the errors are propagated and damped by the time-marching algorithm. The use of this model problem allows us to single out the Mach number as a parameter and catalog the convergence as a function of this parameter. Although the computational problem is simple, we note that it contains all the low-speed physical phenomena of interest to us, and, consequently, the convergence process is non-trivial.

Convergence results using the original system are presented in Fig. 2.3 for Mach numbers of 0.5, 0.1 and 0.001. The results are for central-difference ADI with  $CFL_{u+c} = 3$ . At  $M = 0.5$ , the eigenvalues of the original time-marching system are well-conditioned and good convergence is obtained. For the central-difference ADI algorithm shown here,

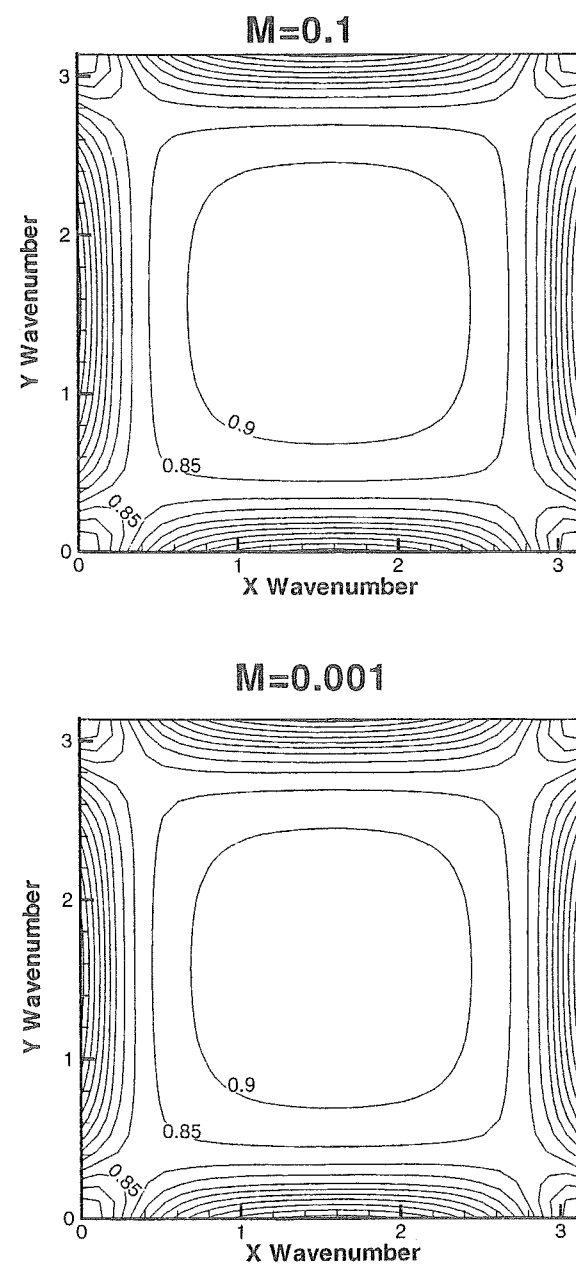


Figure 2.1: Stability results for the preconditioned Euler equations with central difference ADI scheme. CFL=5.

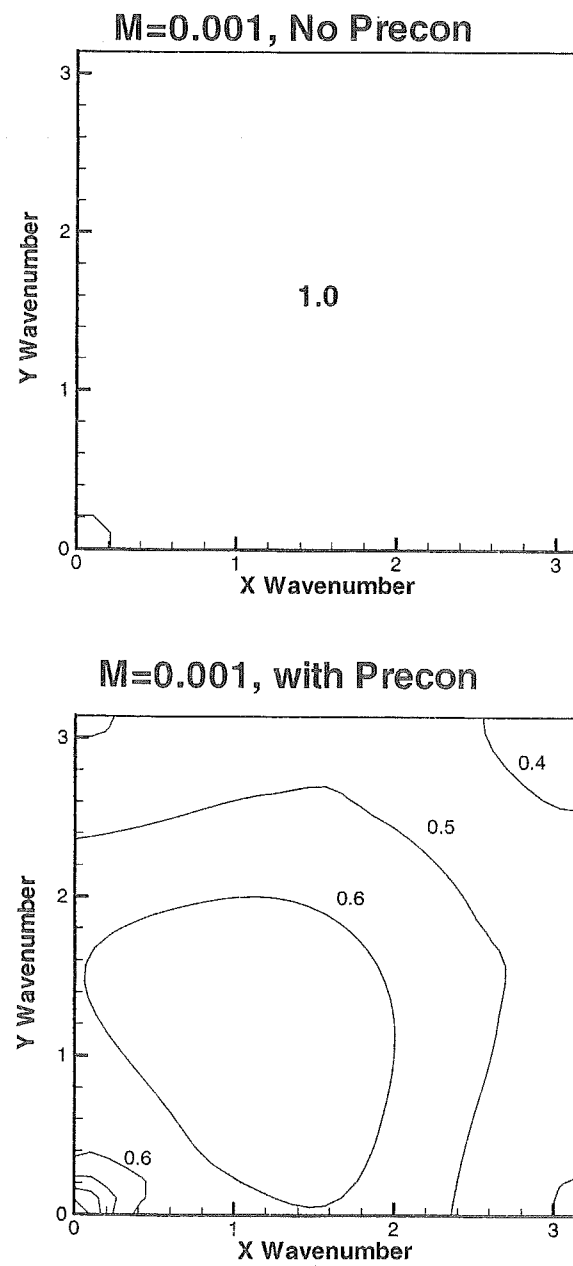


Figure 2.2: Stability results for the original and preconditioned Euler equations with I/III upwind-DDLGS4 scheme. CFL=10.

residual convergence to  $10^{-12}$  is attained in about 1000 iterations. At the lower Mach numbers shown, the convergence rate is observed to degrade seriously, a consequence of the ill-conditioned eigenvalues. In both cases, there is a two or three order of magnitude drop in the residual at the start of the convergence process, followed by a much slower asymptotic convergence rate. This is due to the initial damping of the acoustic error modes, which are handled efficiently by the algorithm. After this initial drop in residual, however, the stiffness of the particle modes dictates the overall convergence rate. We note that, even at the relatively high Mach number of 0.1, the asymptotic convergence rate indicates only about one order of magnitude drop in the residual over about 1000 iterations. At the lower Mach number of 0.001, it would take two or three thousand iterations for an order drop in the residual magnitude. For more complicated problems, this would essentially mean non-convergence of the solution.

Convergence results using preconditioning for the same series of Mach numbers are given in Fig. 2.4. The results are again for the central-difference ADI scheme with  $CFL_{\lambda_+} = 3$ , which is consistent with the previous choice. With preconditioning, we observe that all the Mach numbers converge efficiently. In fact, the  $M = 0.1$  and  $0.001$  cases converge faster than the  $M = 0.5$  case, which is because of a small improvement in the condition number for the low speed cases. It is also noteworthy that the convergence rates for  $M = 0.1$  and  $0.001$  are virtually identical, which agrees very well with the stability results in Fig. 2.1. From these results, it is clear that low Mach preconditioning can offer orders of magnitude improvement in computational performance at low speeds. Convergence results for the upwind algorithms are considered in Chapter 4.

## 2.4 Non-Linear Considerations

Preconditioned algorithms yield significant speed-ups of convergence rates for low Mach numbers (as seen above), viscous-dominated flows, high aspect ratio cells and unsteady flows (as discussed in the coming chapters). At low Mach numbers, we have seen that preconditioning introduces pseudo-acoustic speeds, which are the same order of magnitude as the particle speeds. In other words, preconditioning allows the algorithms to operate at much larger time-steps, so that the slow particle waves are handled optimally. The use of larger time-steps, however, may lead to solution instability during the initial, non-linear stages of a computation and, thereby, result in reduced overall robustness. A fundamental observation in this respect is the increased sensitivity of preconditioning algorithms to pressure disturbances. Preconditioned systems are unstable in the presence of pressure fluctuations that are large compared to the “dynamic” pressure, or  $\rho u^2$ . In contrast, the standard Euler system becomes unstable only when pressure fluctuations are large compared to the “thermodynamic” pressure, or  $\rho c^2$ . In complex problems, involving a wide range of flow speeds, it is possible that the local pressure fluctuations are much larger than the local magnitude of  $\rho u^2$ , leading to instability when preconditioning is used.

It is apparent that the pressure instability is a non-linear phenomenon. Preconditioning is normally applied to the non-linear version of the equations (i.e., before linearization),

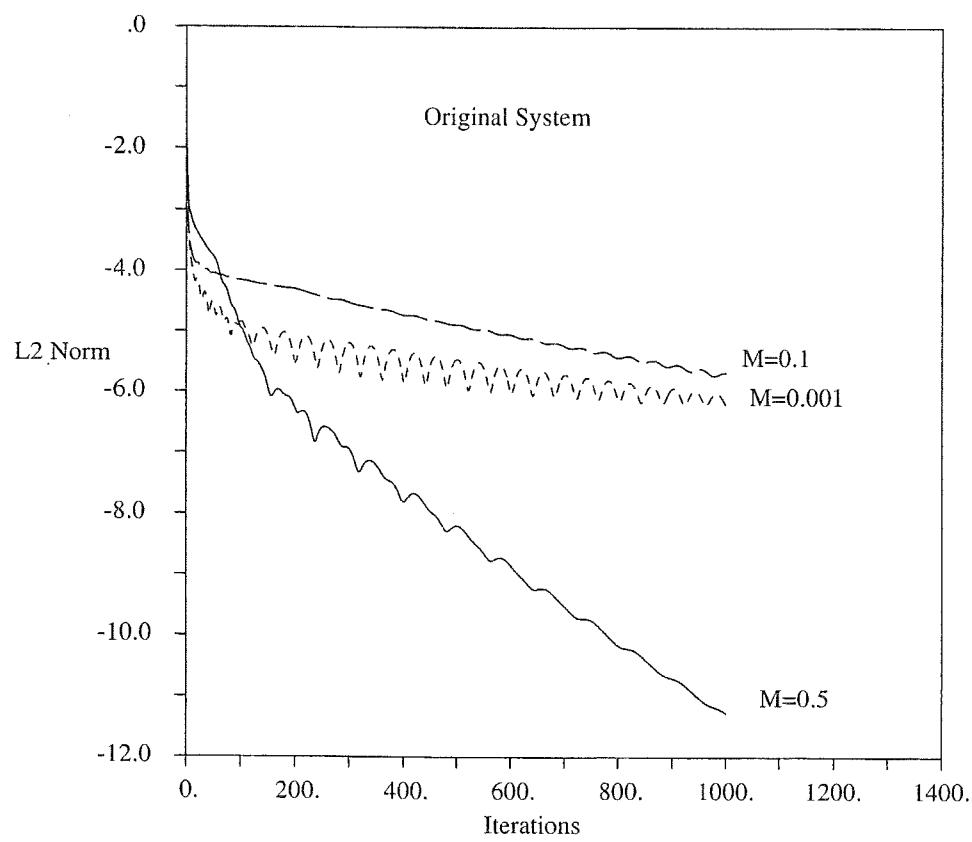


Figure 2.3: Convergence results for central-difference ADI. Inviscid flow in duct.

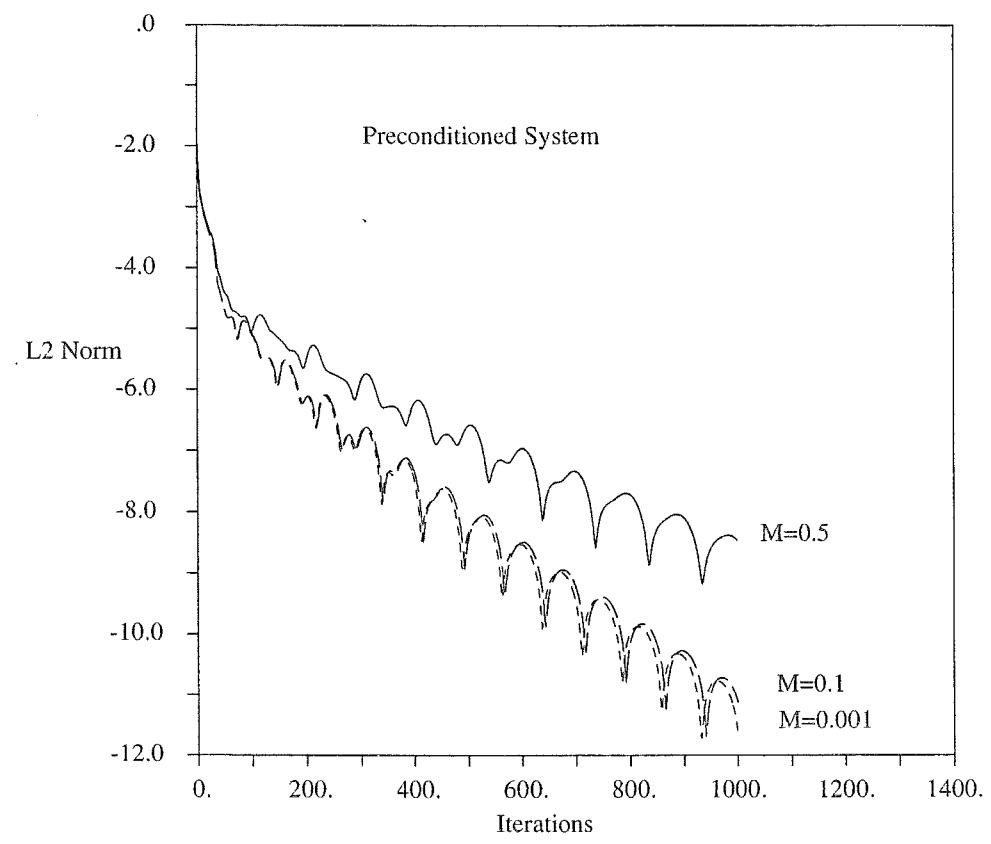


Figure 2.4: Convergence results for central-difference ADI. Inviscid flow in duct.

which renders the system susceptible to the instability. This observation suggests two possible courses of action—the preconditioning may be modified to account for the size of the pressure fluctuations, or the preconditioning may be introduced at the linear solver level (i.e., after linearization). Weiss *et al.* and Darmofal and Siu [55, 43] have considered the former option, while the present authors have investigated the latter [17]. We review both approaches in the current section. In particular, the linearized preconditioning algorithm is implemented within a dual-time framework, with the standard time-derivatives utilized at the outer ‘non-linear’ level and the preconditioned time-derivatives introduced at the inner, ‘linear’ level. Apart from the gains in robustness, this dual-time approach promises significant gains in computational efficiency as well.

#### 2.4.1 Stability and Robustness Issues

It is useful to consider the low Mach number perturbation system derived in Section 2.1 to gain insight into the nature of the preconditioned system’s increased sensitivity to pressure fluctuations. It is evident that the perturbation procedure is valid only as long as pressure fluctuations are of the order of  $\epsilon_i p_1$ . Since  $p_1$  is of order unity (due to the non-dimensionalization), this means that non-dimensional pressure fluctuations should be of the order  $\epsilon_i = \gamma M_r^2$ , or the dimensional pressure fluctuations should be of the order  $\rho u^2$ . When the pressure fluctuations are larger, the perturbation expansion breaks down and it is no longer appropriate to take that the zeroth order pressure ( $p_0$ ) as a constant. Indeed, as we see in Section 2.4.3, the preconditioned scheme becomes unstable when pressure fluctuations exceed the local magnitude of  $\rho u^2$  (i.e., the dynamic pressure). In contrast, the non-preconditioned system is stable for fluctuations of the order of  $\rho c^2$  (i.e., the thermodynamic pressure).

A related difficulty with preconditioning is the lack of robustness in the neighborhood of stagnation points (particularly for inviscid flows). One of the aspects of the stagnation region is that the flow velocities are much smaller than the free-stream velocities, with the velocity going to zero at the stagnation point. The pressure in this region, on the other hand, increases in proportion to the squared of the free-stream velocity (i.e.,  $p_{stag} = p_\infty + \rho_\infty u_\infty^2$ ). There is, therefore, a proclivity for the pressure fluctuations to exceed the “local”  $\rho u^2$ , thereby leading to instability. This point was appreciated by Darmofal and Schmid [41], who also note that, in the low Mach number limit, the eigenvectors of the preconditioning system become degenerate. Further, van Leer and Lee [42] suggest that the ill-defined flow angle in the vicinity of the stagnation point exacerbates the problem. We note that the evidence indeed seems to suggest that the stagnation point problem is a combination of these effects. Thus, to “fix” one of these issues may not be sufficient for eliminating the difficulty.

The standard approach for handling the stagnation point problem has been to use the freestream velocity to define the preconditioning parameter ( $\beta$  in artificial compressibility and  $\rho'_p$  in our system). The difficulty with this approach is that the definition of the preconditioning becomes “non-local”, and it may not be possible to optimize the system for complex problems wherein a mixture of flow regimes may occur. Further, for many

complex problems, well-defined free-stream conditions may not exist.

In the following sections, we consider two approaches that have been developed to handle the sensitivity to pressure fluctuations. One approach devised by Weiss and Smith [55] is to modify the definition of the preconditioning parameter by introducing a term that is proportional to the pressure fluctuations. This method appears to work well for the stagnation point problem (see also [43]), but our experience is that it is not always effective for large pressure fluctuations arising in other situations. The second approach is to use a linearized implementation of the preconditioning procedure [17]. This method provides robustness to pressure fluctuations similar to the non-preconditioned method (because the method is not preconditioned at the non-linear equation level). However, it does not eliminate the stagnation point problem. Although this has not yet been investigated, it should be possible to combine the two approaches for greater overall robustness.

#### 2.4.2 Modification of Preconditioning Definition

We noted earlier that when the pressure perturbations are larger than the local  $\rho u^2$ , the  $\epsilon_i$  parameter in the perturbation expansions is no longer small. In other words, the choice of the perturbation parameter needs to be modified, which will in turn modify the preconditioning parameter ( $\rho'_p$  or  $V_p$ ). One particular manner of modifying the preconditioning parameter is [55],

$$V_p = \text{Min}[\text{Max}(V_{inv}, V_{pgr}), c] \quad (2.34)$$

where  $V_{inv} = \sqrt{u^2 + v^2}$  is the original inviscid choice given earlier, and  $V_{pgr}$  is the new pressure-gradient based velocity scale. This the new scale is given by,

$$V_{pgr} = \sqrt{\frac{|\Delta p|}{\rho}}$$

The modified value of velocity parameter,  $V_p$  (or equivalently, the preconditioning Mach number parameter,  $M_p$ ) is employed in the definition of Eqns. 2.27 and 2.28. The quantity  $|\Delta p|/\rho$  may be obtained in a convenient fashion by computing the quantity across each of the faces of the cell. For a given cell, the term is computed by using either the maximum for the cell-faces or an average of these values.

It should be noted that the above definition partially (or, in extreme cases, completely) “undoes” the preconditioning locally and thereby increases the robustness to pressure fluctuations. For instance, consider the situation when the pressure fluctuations are of the order of  $\rho c^2$ . We noted earlier that the original equations are stable for pressure fluctuations of that magnitude, but the preconditioned equations are only stable to magnitudes of the order of  $\rho u^2$ . In this case, the above definition would select the preconditioned sound speed velocity to be equal to the physical speed of sound. This would then “un-precondition” the equations on a local basis and thereby stabilize the algorithmic response to the fluctuation.

### 2.4.3 Linearized Dual-Time Preconditioning Method

An alternate strategy is to introduce the preconditioning at the linear solver stage since the pressure instability is a non-linear phenomenon. We implement this via a dual-time algorithm, similar to those developed for incompressible flow [59, 58]. Standard time-derivatives are used at the outer, non-linear level, while preconditioned time-derivatives are introduced at the inner, linear level. The overall time-marching problem thus remains stable for “large” pressure fluctuations, while the inner time-marching problem optimizes the convergence process. In this section, we present the details of this dual-time, linearized, preconditioning scheme.

#### Formulation of Linearized Dual-Time Method

We begin with the non-preconditioned governing equations (Appendix A.1.2). Expressing the Euler implicit scheme in the delta form, we get:

$$\left[ \frac{\Gamma_e^n}{\Delta t} + \frac{\partial A^n}{\partial x} + \frac{\partial B^n}{\partial y} \right] \Delta Q_p = -\mathcal{R}^n \quad (2.35)$$

$\Delta Q_p = Q_p^{n+1} - Q_p^n$  and  $\Gamma_e$  is the transformation Jacobian,  $\partial Q / \partial Q_p$ . It is obtained by setting  $\rho'_p = \rho_p$  ( $M_p = 1$ ) and  $\rho'_T = \rho_T$  (or  $\delta = 1$ ) in the definition of  $\Gamma_p$  (Eqn. 2.24). Note that an infinite time-step would correspond to full Newton linearization. We, however, retain the time-step term for generality.

For efficient solution of the above linear operator, we devise an iterative procedure by introducing a new time-derivative. To distinguish this ‘inner’ time-derivative from the outer one, we use  $\tau$  to represent the ‘inner’ time variable. This procedure is akin to the multi-sweep relaxation methods discussed in Chapter 1.2.4 except that we introduce a second time-derivative. Further, the inner time-derivative may be preconditioned to optimize the inner convergence rate. The preconditioned dual-time system may be written as,

$$\Gamma_p^n \frac{Q_p^{n+1,k+1} - Q_p^{n+1,k}}{\Delta \tau} + \left[ \frac{\Gamma_e^n}{\Delta t} + \frac{\partial A^n}{\partial x} + \frac{\partial B^n}{\partial y} \right] \Delta Q_p^{k+1} = -\mathcal{R}^n \quad (2.36)$$

where  $k$  is the index for the inner iteration time-level and  $\Delta Q_p^{k+1} = (Q_p^{n+1,k+1} - Q_p^n)$ . Expressing the inner-iterative solution procedure in delta form gives:

$$\begin{aligned} & \left[ \frac{\Gamma_p^n}{\Delta \tau} + \frac{\Gamma_e^n}{\Delta t} + \frac{\partial A^n}{\partial x} + \frac{\partial B^n}{\partial y} \right] (Q_p^{n+1,k+1} - Q_p^{n+1,k}) = -\mathcal{R}^n - \\ & \left[ \frac{\Gamma_e^n}{\Delta t} + \frac{\partial A^n}{\partial x} + \frac{\partial B^n}{\partial y} \right] (Q_p^{n+1,k} - Q_p^n) \end{aligned} \quad (2.37)$$

Equation 2.37 can now be solved using any standard iterative procedure—implicit or explicit. For purposes of demonstration, we employ the standard ADI approximate factorization here,

$$\left[ \mathcal{S} + \frac{\partial A^n}{\partial x} \right] \mathcal{S}^{-1} \left[ \mathcal{S} + \frac{\partial B^n}{\partial y} \right] (Q_p^{n+1,k+1} - Q_p^{n+1,k}) = -\mathcal{R}^n -$$

$$\left[ \frac{\Gamma_e^n}{\Delta t} + \frac{\partial A^n}{\partial x} + \frac{\partial B^n}{\partial y} \right] (Q_p^{n+1,k} - Q_p^n) \quad (2.38)$$

where  $\mathcal{S} = \frac{\Gamma_p^n}{\Delta \tau} + \frac{\Gamma_e^n}{\Delta t}$ . Note that when the ADI inner iterations converge, the RHS residual, which is Eqn. 2.35 is satisfied.

The above dual-time method represents a generalized formulation for the solution of the governing equations. It represents a “direct” solution method when the inner iterations are performed to convergence at each outer time-step level. On the other hand, when only one inner iteration is performed, the method reverts to the standard (‘non-linear’) preconditioning scheme. Implementation of the dual-time ‘direct’ method deserves further discussion and is considered in the following section.

### Implementation Issues

The dual-time procedure closely resembles the multi-sweep relaxation schemes considered in Section 1.2.4. The difference lies in the introduction of the second inner time-step ( $\Delta \tau$ ), which optimizes the inner iterations and, thereby, removes any restrictions in the outer time-step size that the linear solver may otherwise impose. The outer time-step may then be selected independent of the linear-iterative strategy. Further, the dual-time approach allows flexibility in the order of accuracy of the linearized operators. We discuss these implementation issues here.

**Order of Accuracy.** In Eqn. 2.38, the order of accuracy of solution is represented in the computation of the residual,  $\mathcal{R}$ . In addition, there are two implicit operators—the “outer” and “inner” implicit operators on the RHS and LHS respectively. It is not necessary for either of these operators to be of the same order as the solution. For central differences, it is convenient to employ second-order differences for both the implicit operators (consistent with the residual  $\mathcal{R}$ ) and likewise for first-order upwind schemes.

For higher-order upwind differences, on the other hand, the residual  $\mathcal{R}$  is typically evaluated with third-order upwind-biased differences. Two approaches are then possible for the implicit operators. In the first, the outer operator is III order so that the outer iterations are Newton-like, while the inner operator is I order to take advantage of the diagonal dominance in the choice of solution method. The inner iteration scheme would then correspond to a I/III upwind scheme (as discussed in Section 1.2.3). This set of choices corresponds to that used usually in preconditioned Newton-GMRES techniques [73]. The second approach involves selecting both outer and inner operators to be first order. This would mean that the outer iterations represent a I/III upwind scheme, while the inner iterations would be I/I. This approach is commonly used by the algebraic multigrid community [55].

**Artificial Dissipation Models.** Careful formulation of the artificial dissipation terms for the discretization of the flux derivatives is important for maintaining accuracy. Specifically, accuracy constraints at low Mach numbers demand the use of the preconditioned system in devising the artificial dissipation models (Section 2.1.5). This requirement pro-

vides the curious result that the formulation of the flux terms at the non-linear level are influenced by the choice of preconditioning system at the linear level. In general, it may be possible to devise schemes with two sets of preconditioning matrices with the non-linear preconditioning being selected for preserving accuracy in the flux formulation, and the linear-level preconditioning being selected to maximize convergence of the linear iterations. However, we have not yet attempted such refinements in practice and our present procedure corresponds to selecting the same matrix at both levels. The formulation of the convective flux terms using flux-difference splitting is summarized in Appendix C.1.

**Stability and Convergence of the Inner Iterations.** We note that Eqn. 2.38 closely resembles the preconditioned dual-time formulation for unsteady computations [62] (see Chapter 5). The stability properties of the scheme are, therefore, identical with the results given in Chapter 5. Further, when the outer time-step is infinity (see below), which is frequently the case, the inner iteration stability properties become identical to those of the steady-state preconditioning system (Section 2.3.1). The selection of the inner time-step,  $\Delta\tau$ , is then prescribed by the properties of the inner-iterative scheme. For explicit schemes, it should satisfy the prescribed stability criterion based upon  $CFL_\tau$  (and, for viscous problems, the viscous time-step), while for the ADI scheme considered here, the optimal choice is obtained by selecting  $CFL_\tau$  to be about 5. More details of the time-step selection for ADI schemes are given in Chapter 4. Finally, we note that proper selection of the preconditioning matrix is evidently important to optimize inner iteration convergence. For the inviscid case, the form and definition of the preconditioning matrix are the same as in Eqn. 2.24.

**Outer Time-Step Selection.** As mentioned earlier, if the inner iterations are fully converged, the scheme reverts to a direct method. The choice of outer time-step size ( $\Delta t$ ) is then limited only by non-linearities. With a good initial condition, it is usually possible to choose  $\Delta t$  to be infinity, facilitating rapid outer convergence. Moreover, full convergence of the inner iterations is usually unnecessary. Our results show that one to two orders of residual reduction at the linear level are sufficient to obtain rapid outer iteration convergence.

**Storage Requirements.** Since the inner iterations are completely linear, the residual  $R$  and Jacobians  $\Gamma_p$ ,  $\Gamma_e$ ,  $A$  and  $B$  are all evaluated at time-level  $n$ . There is, therefore, no need to recompute them during the inner-iterative process, provided these variables are stored. There are two sets of quantities to be stored—the first set is the non-linear implicit operator that is on the RHS of Eqn. 2.38, while the second set is the block tridiagonal inversion of the LHS. The associated storage requirements can be significant, and depend upon the order of accuracy of the discretizations used in each operator. Further, storage requirements for larger equation systems such as reacting flows are proportionately greater. However, computational results indicate that dramatic savings in CPU time are possible. Typically, storing the Jacobians contributes about a factor of two savings in CPU time, while storing the block tridiagonal decomposition yields a further factor of

four to five in savings. Total savings, therefore, can be as high as a factor of eight to ten. These numbers are based upon computations using flux-differenced discretizations and the implicit-ADI scheme on a single CRAY-J916 processor. With the advent of parallel processing, the storage overhead appears to be quite affordable even for large problems.

In summary, the linearized, preconditioned, dual-time scheme promises increased robustness because the outer, non-linear time-derivatives are not preconditioned. The inner iterations need to be performed only until the large pressure disturbances are eliminated. Beyond that, the method may be reduced to the standard preconditioned iterative procedure by performing only one set of inner iterations. On the other hand, the method also offers the flexibility to be used as a “direct” method, if the linear iterations are converged adequately. These sub-iterations are extremely inexpensive if the associated Jacobians and block tridiagonal decompositions are stored, avoiding recomputing them. As the results in the following section demonstrate, significant savings in CPU time are possible with the linearized method. Further, the linear formulation would also facilitate the inclusion of other linear equation convergence acceleration techniques such as multigrid [56, 43] and GMRES [73].

## Computational Results

**Inviscid Straight Duct.** As the first test case, we select the simple case of uniform flow in an inviscid straight duct with perturbed pressure and velocity fields as the initial condition. We examine the performance of the linearized, preconditioned scheme with regard to both CPU-efficiency as well as robustness. In the latter instance, we carry out convergence studies for different levels of pressure perturbation and examine the stability behavior of the scheme. The studies are carried out using a 61x61 uniform grid, with a flow Mach number of  $1 \times 10^{-3}$ .

Figure 2.5 shows convergence results for the overall solution plotted against outer-iteration number. These results are for ‘small’ amplitudes of pressure disturbance ( $0.5\rho u^2$ ). In this case, we anticipate the standard (non-linear) preconditioning algorithm to be stable. Indeed, the results in Fig. 2.5 for one inner iteration at each outer time-step (corresponding to the standard formulation) show steady convergence, with machine zero being attained in about 1600 iterations.

The other plots on Fig. 2.5 correspond to the cases with progressively larger number of inner iterations performed at each outer time-step. These cases correspond to different realizations of the linearized preconditioning scheme. When a large number of inner iterations are performed, the scheme corresponds to direct inversion. Here, we show results for 5, 10, 20 and 50 inner iterations per outer iteration. Five inner iterations correspond to a little less than an order of magnitude reduction in the inner iteration residual, while 50 inner iterations correspond to between two and three orders of residual reduction. It is observed that even a modest number of inner iterations increases outer-level convergence rate dramatically. At 50 inner iterations, machine zero convergence is attained in less than 50 outer time-steps. Even faster outer convergence results when

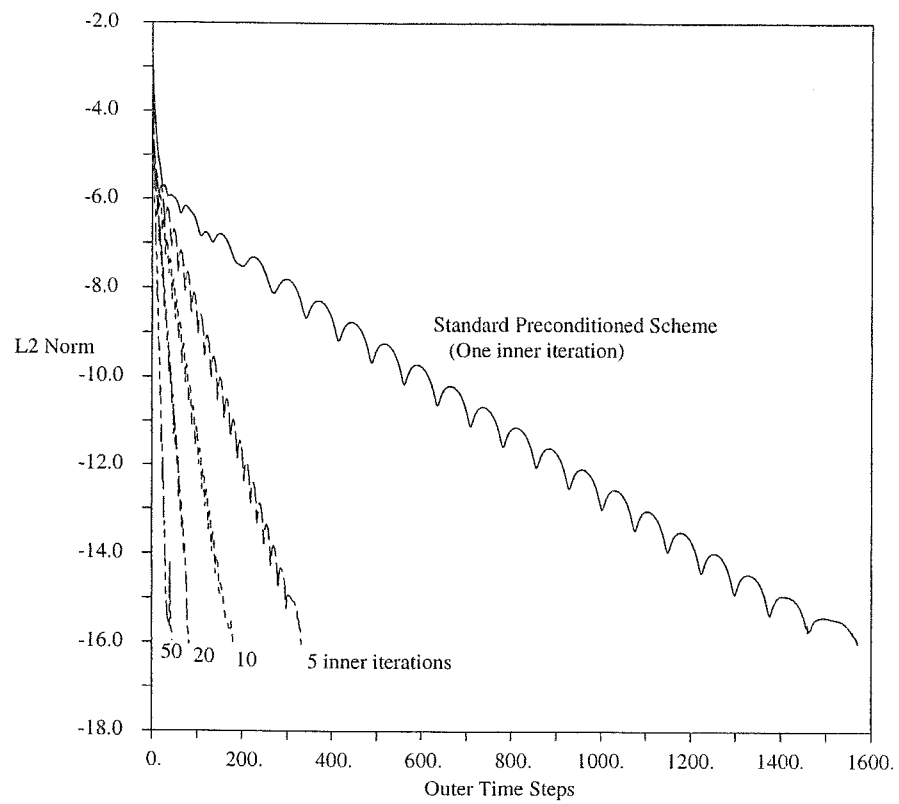


Figure 2.5: Convergence results vs outer iteration time step for inviscid straight duct.  
 $M = 1 \times 10^{-3}$ .

increased numbers of inner iterations are performed, but the increased CPU time starts to offset the gains.

The same convergence results are shown in terms of CPU time (on a CRAY-J916 processor) in Figure 2.6. The standard preconditioning scheme takes about 800 CPU seconds, while the linearized scheme with 50 inner iterations takes less than 90 seconds, a speed-up of about a factor of nine. As mentioned earlier, performing additional inner iterations starts to take more CPU time and the 50-iteration case more or less represents the optimum performance of the scheme.

Figure 2.7 shows convergence results for different amplitudes of the initial pressure disturbance. Results are shown for four different amplitudes, namely  $0.5\rho u^2$ ,  $0.5 \times 10^2 \rho u^2$ ,  $0.5 \times 10^4 \rho u^2$  and  $0.5 \times 10^6 \rho u^2$ . The last case corresponds to  $0.5\rho c^2$  since the flow Mach number is  $1 \times 10^{-3}$ . Convergence results for the standard non-preconditioned scheme is observed to be stable for all the imposed disturbances, although convergence is very slow. In contrast, the standard, preconditioned scheme (not shown) is stable only for the smallest disturbance magnitude (as shown in Figs. 2.5 and 2.5) and is violently unstable for the other cases. Note that these results are in agreement with the theoretical arguments presented earlier.

Convergence results for the linearized, preconditioned scheme are observed to be both stable and efficient. It should be pointed out that the larger the magnitude of the initial disturbance, the larger the number of inner iterations that are necessary to obtain stable convergence behavior. For the largest disturbance magnitude, about 400 inner iterations are required. Of course, the increased inner iterations are required only in the initial computational stages, until the pressure disturbances are reduced in magnitude. In the later stages, fewer iterations (about 50 iterations are the optimum for this case) may be used to maximize the CPU time benefits.

**Flat Plate Boundary Layer.** For a more practical example, we consider the classical Blasius boundary layer solution. For the purposes of the present discussion, it is sufficient to note that the preconditioning is selected to provide optimal convergence for this problem. Further details are deferred until Chapter 4. The objective here is to examine the efficiency of the linearized formulation compared to the standard formulation. We employ a 61x61 grid, a free-stream Mach number of  $1 \times 10^{-3}$  and  $Re_x = 100$ . Figure 2.8 shows convergence results in terms of outer iteration step. Again, the results for one inner iteration at each outer time-step corresponds to the standard formulation, while the other results correspond to different realizations of the linearized formulation.

The convergence results show that the standard scheme requires about 800 iterations for machine zero convergence. With the enhanced scheme, even a modest number of inner iterations dramatically reduces the number of outer iterations. For 50 inner iterations per outer step, machine zero convergence is attained in only 24 outer iterations. Figure 2.9 shows the same convergence results in terms of CPU time. The standard scheme takes about 400 CPU seconds to reach machine zero, while with 50 inner iterations, the same convergence level is attained in about 50 seconds, yielding a speed-up of about eight times.

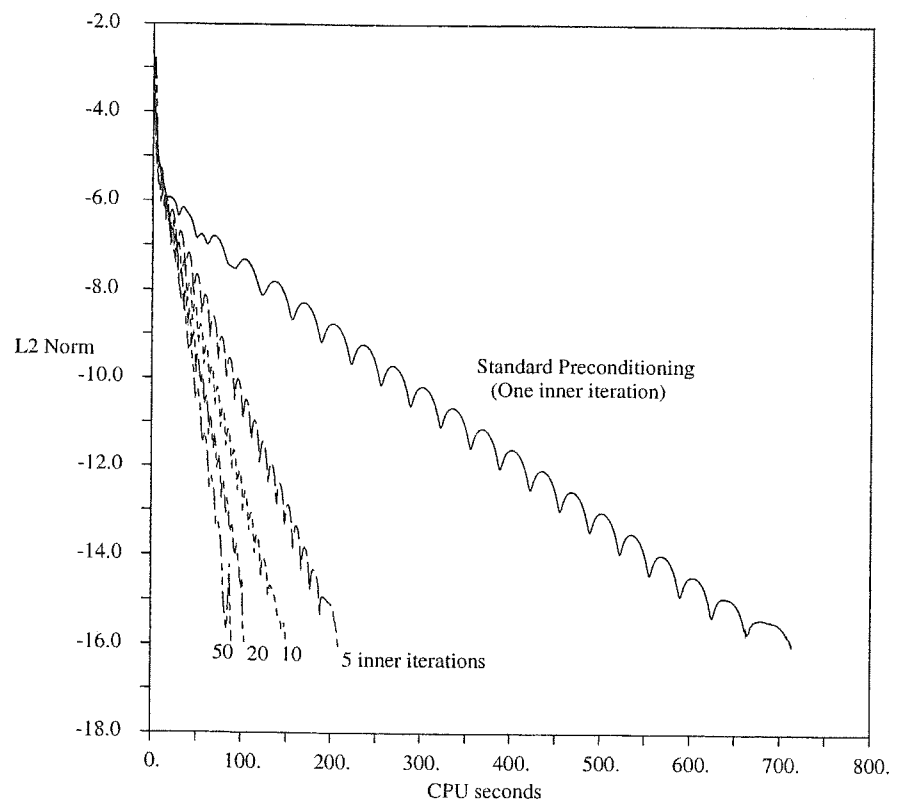


Figure 2.6: Convergence results vs CPU time (CRAY-J916) for inviscid straight duct.  
 $M = 1 \times 10^{-3}$ .

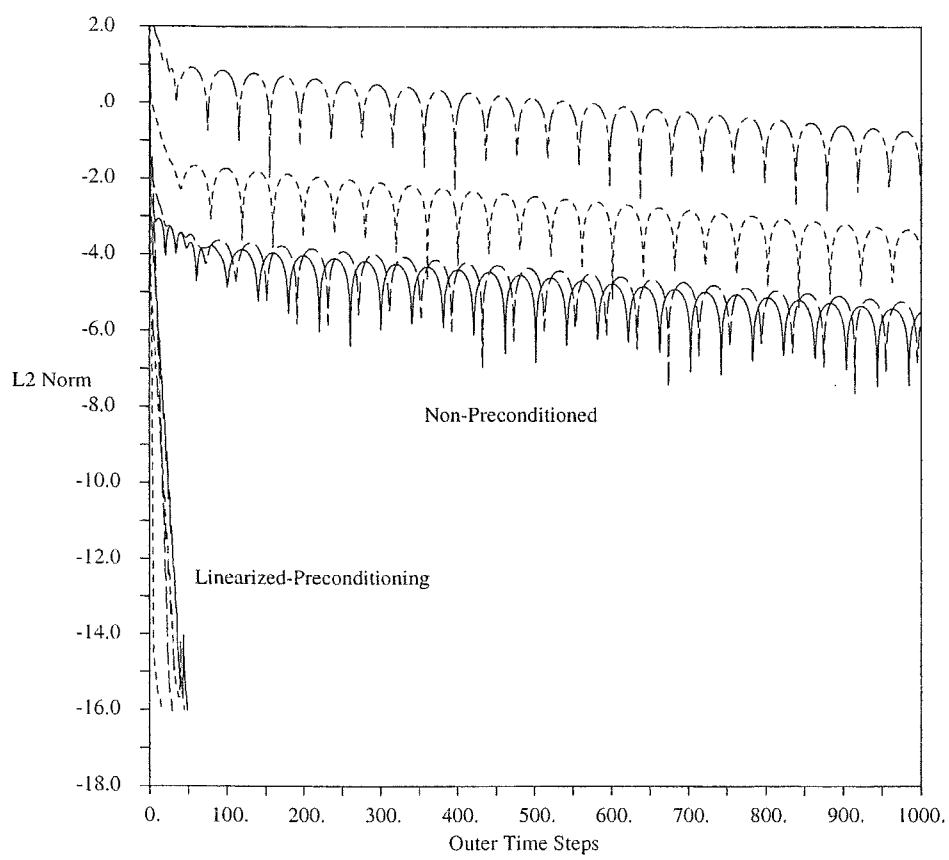


Figure 2.7: Convergence results vs outer iteration time step for inviscid straight duct with different magnitudes of imposed pressure disturbances as initial condition.  $M = 1 \times 10^{-3}$ .

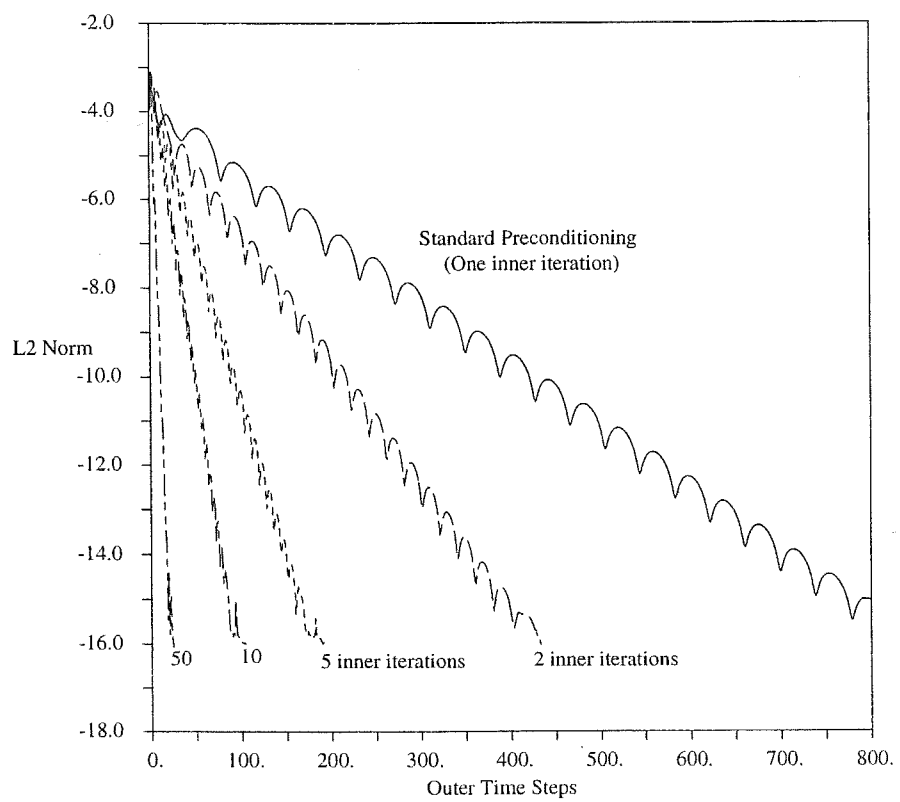


Figure 2.8: Convergence results vs. outer iteration time-step for flat plate boundary layer.  
 $M = 1 \times 10^{-3}$  and  $Re_x = 100$ .

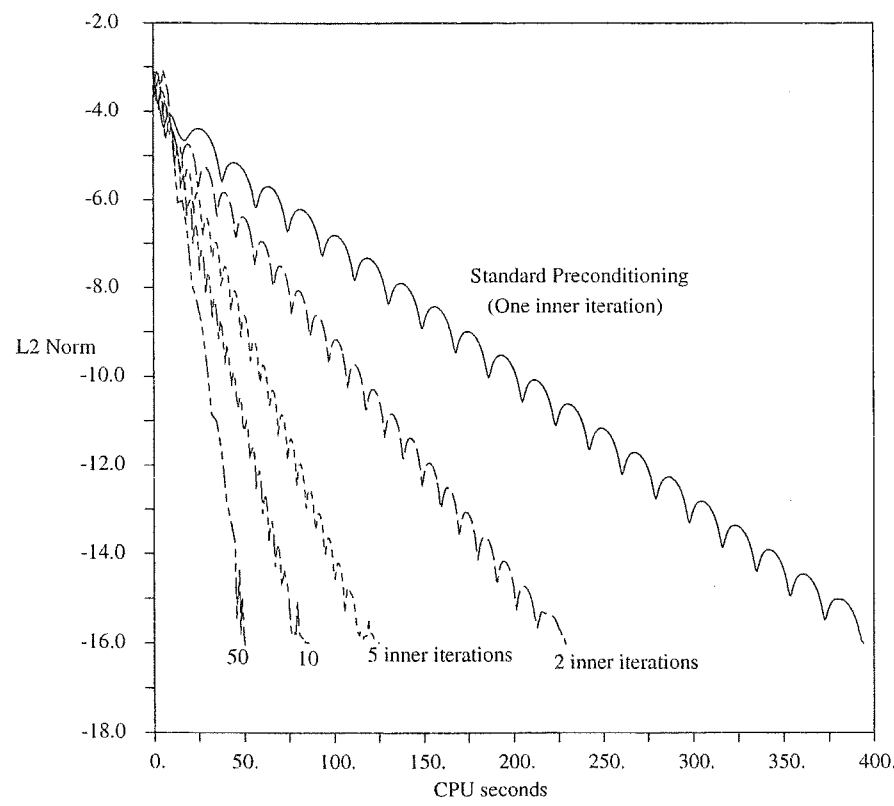


Figure 2.9: Convergence results vs. CPU time (CRAY-J916) for flat plate boundary.  
 $M = 1 \times 10^{-3}$  and  $Re_x = 100$ .

# Chapter 3

## Preconditioning for the Navier-Stokes Equations

We have discussed the difficulties that time-marching algorithms face with the Euler equations at low Mach numbers and how preconditioning techniques may be devised to alleviate the problems. We now turn to the more complicated Navier-Stokes equations. It may be anticipated that at high Reynolds numbers the dominant characteristics controlling the solution of the Navier-Stokes equations are the same as those of the Euler equations. However, by the same token, we would expect the situation to be markedly different at low Reynolds numbers. Diffusion-dominated flows are frequently of interest in industrial applications—some examples include plasma flows, chemical vapor deposition, natural convection, metal extrusion, etc. Further, even in high Reynolds number problems, we frequently encounter boundary layer or shear layer flows, wherein the Reynolds number is large in the streamwise direction, but is usually small in the cross-stream directions. Such problems are typically characterized by the use of highly stretched grid cells to accommodate the disparate spatial scales. In this chapter, we analyze the Navier-Stokes equations. Specifically, we consider the low Reynolds number limit of the equations by applying similar perturbation procedures and then consider appropriate preconditioning techniques. High grid aspect ratio issues are the subject of the following chapter.

### 3.1 Analytical Solution of the Navier-Stokes Equations

The physical processes underlying the convergence behavior of the Navier-Stokes equations are not as well understood as those of the Euler equations. In the case of the Euler equations, errors are convected out of the system by particle and acoustic waves. For the Navier-Stokes equations, it is evident that the viscous terms introduce damping modes, but the effects of these terms differ for the particle and acoustic waves. In order to more precisely explain the nature of the controlling physics, we obtain an analytical solution of the one-dimensional Navier-Stokes equations in linearized form [45].

### 3.1.1 Standard Navier-Stokes Equations

We begin with the Navier-Stokes equations written in their standard vector form,

$$\frac{\partial Q}{\partial t} + \frac{\partial E}{\partial x} = \frac{\partial V}{\partial x} \quad (3.1)$$

where the inviscid and viscous fluxes are provided in Appendix A.1.2. Further, in the present analysis, we will assume that the fluid obeys the ideal gas law.

In order to examine the transient behavior of the Navier-Stokes equations in the low Reynolds number limit, we consider linearized solutions of the constant coefficient version of Eqn. 3.1,

$$\Gamma_e \frac{\partial Q_p}{\partial t} + A \frac{\partial Q_p}{\partial x} = \frac{\partial}{\partial x} R_{xx} \frac{\partial Q_p}{\partial x} \quad (3.2)$$

where  $\Gamma_e = \partial Q / \partial Q_p$  and  $A$  and  $R_{xx}$  have their usual definitions.

We seek solutions of the form  $Q_p(x, t) = \hat{Q}_p e^{i\omega t} e^{-ikx}$ . Substituting the expression into the governing equations, we obtain a general dispersion relation linking the complex frequency  $\omega$  and the wave number  $k$ ,

$$\det [ \Gamma_e(i\omega) - A(ik) + R_{xx}(k^2) ] = 0 \quad (3.3)$$

For the case of  $Pr = 1$  and neglecting viscous dissipation, we can obtain the following roots for the complex frequency,

$$\begin{aligned} \omega_1/k &= u(1 + i/Re) \\ \omega_{2,3}/k &= u \left[ 1 - \frac{i\gamma}{2Re} \left( -1 \pm \sqrt{1 - \frac{4Re^2}{\gamma^2 M^2}} \right) \right] \end{aligned} \quad (3.4)$$

where the Reynolds number is defined using  $1/k$  as the length scale, i.e.,  $Re = u/k\nu$ .

We are interested in the limiting values of these roots under various Mach/Reynolds number conditions. Table 3.1.1 lists these limiting values. For instance, in the high Reynolds number limit, we note that the first root becomes  $\omega_1/k = u$ , while the remaining two reduce to  $\omega_{2,3}/k = u \pm c$ , thereby giving the familiar particle and acoustic eigenvalues of the Euler equations.

When the flow is viscous-dominated (i.e., low Reynolds number), two possible situations may arise depending on the magnitude of a second parameter, the “acoustic” Reynolds number,  $Re_c = c/\nu k = Re/M$ . When the acoustic Reynolds number is high (which is often the case when the flow speed is very low, i.e.,  $M \ll Re$ ), the first expression yields an imaginary root,  $\omega_1/k = iu/Re$ , while the second expression remains real,  $\omega_{2,3}/k = u \pm c$ . The first root indicates viscous damping of the particle wave, while the second and third roots indicate acoustic propagation at  $u \pm c$ . This result suggests that acoustic wave propagation processes remain dominant under this low Reynolds number limit, even though the viscous processes dominate the other modes of the solution.

The second situation that arises in the limit of low Reynolds number corresponds to when the acoustic Reynolds number is also small in comparison to unity, i.e., when

Reynolds no. limits	$\omega_1/k$	$\omega_2/k$	$\omega_3/k$	condition #
$Re \gg 1$	$u$	$u + c$	$u - c$	$1 + 1/M$
$Re \ll 1, Re/M \gg 1$	$\frac{iu}{Re}$	$u + c$	$u - c$	$(1 + 1/M) Re$
$Re \ll 1, Re/M \ll 1$	$\frac{iu}{Re}$	$u$	$\frac{iu\gamma}{Re}$	$\gamma/Re$

Table 3.1: Original Navier-Stokes

$Re/M$  is small. In this case, the first root remains imaginary,  $\omega_1/k = iu/Re$ ; however, the term under the square-root in the second expression now tends to unity—the root with the negative sign then gives a complex root ( $\omega_2/k = iu\gamma/Re$ ), while the root with the positive sign remains real,  $\omega_3/k = u$ . The first two roots then correspond to viscous damping modes while the third root indicates a wave that propagates at the particle velocity. The two imaginary roots apparently arise from the viscous terms in the momentum and energy conservation equations, while the real root appears to correspond to the continuity equation (which does not contain any viscous terms).

From this simple analysis, it is apparent that the behavior of the Navier-Stokes equations is rich in complexity. The controlling physical processes vary significantly in character depending on the the Mach number and particle/acoustic Reynolds numbers. In particular, some of the inviscid modes (corresponding to acoustic wave propagation) remain relevant even when the problem is viscous-dominated. Table 3.1.1 also lists the associated condition numbers of the system, which are an indication of the stiffness of the system and may be defined as,

$$\sigma = \frac{\text{Max}(|\omega_1/k|, |\omega_2/k|, |\omega_3/k|)}{\text{Min}(|\omega_1/k|, |\omega_2/k|, |\omega_3/k|)} \quad (3.5)$$

When  $\sigma$  is near unity, the system is well-conditioned and when it is much larger than unity, the system becomes stiff and poor convergence is observed. It is therefore evident that the Navier-Stokes equations become stiff at low Mach numbers and at low Reynolds numbers.

### 3.1.2 Preconditioned Navier-Stokes Equations

In the previous chapter, we derived a preconditioning system based upon the inviscid characteristics of the Euler equations. We have demonstrated that the Euler preconditioning

system offers significant savings in computational time for low Mach number computations. It is interesting to see how this preconditioned system performs in the presence of viscous terms. We therefore determine the analytical solution for the linearized constant coefficient version of the preconditioned equations,

$$\Gamma_p \frac{\partial Q_p}{\partial t} + A \frac{\partial Q_p}{\partial x} = \frac{\partial}{\partial x} R_{xx} \frac{\partial Q_p}{\partial x} \quad (3.6)$$

where all the terms are the same excepting the preconditioning matrix  $\Gamma_p$ . For purposes of this analysis, we make the further assumption of ideal gas and, for the preconditioning parameters, we set  $\rho'_p = 1/\epsilon_p c^2$  and  $\rho'_T = 0$ . This gives us the original Choi-Merkle system [34] with  $\epsilon_p = M_p^2 = \text{Min}(M^2, 1)$ .

The complex roots of the corresponding dispersion relation are given as,

$$\begin{aligned} \omega_1/k &= u(1 + i/Re) \\ \omega_{2,3}/k &= \frac{u}{2} \left\{ \left[ (1 + M_p^2) + i/Re \right] \pm \right. \\ &\quad \left. \sqrt{(1 - M_p^2)^2 + 4M_p^2/M^2 - 1/Re^2 + 2i/Re[1 - M_p^2(2\gamma - 1)]} \right\} \end{aligned} \quad (3.7)$$

Table 3.1.2 summarizes the limiting forms of these roots along with their condition numbers. The tabulated results are for subsonic flow, i.e.,  $M_p = M$ . For high Reynolds numbers, as anticipated, the inviscid preconditioning significantly improves the conditioning of the system. However, at low Reynolds number, the condition number becomes progressively larger, increasing as  $1/Re^2$ . In fact, the condition number at low Reynolds numbers is actually worse than that of the original system (Table 3.1.1). Note also that this result is not dependent upon the acoustic Reynolds number, which no longer appears as a parameter. Selection of the preconditioning based upon the acoustic and particle wave speeds is therefore not physically relevant in the viscous limit. This result is important because it says that a low Mach number preconditioned code would perform extremely poorly under low Reynolds number conditions. It is thus necessary to devise an appropriate preconditioning strategy for the Navier-Stokes equations that is well-behaved at all Reynolds numbers. In the following section, we use perturbation expansions to probe the limiting behavior of the Navier-Stokes equations.

### 3.2 Perturbation Expansions of the Low Reynolds Number Limit

As we did in the Euler equations case, we employ asymptotic expansions to relate the behavior of the Navier-Stokes equations under low Reynolds number limiting conditions. We then devise properly scaled pseudo-time derivative terms to balance the dominant physical terms and show that the resulting preconditioning has well-conditioned Navier-Stokes characteristics. We also use the perturbation equations to assess the conditioning

Reynolds no. limits	$\omega_1/k$	$\omega_2/k$	$\omega_3/k$	condition #
$Re \gg 1$	$u$	$\frac{u}{2} (1 + \sqrt{5})$	$\frac{u}{2} (1 - \sqrt{5})$	2.61
$Re \ll 1$	$\frac{\hat{u}}{Re}$	$\frac{\hat{u}}{Re}$	$\frac{5}{4} (\hat{u} Re)$	$\frac{5}{4} \frac{1}{Re^2}$

Table 3.2: Preconditioned Navier-Stokes,  $\epsilon_p = M^2$

of the artificial dissipation terms and their influence on solution accuracy under such limiting conditions.

### 3.2.1 Perturbation Expansion and Viscous Preconditioning

We begin with the one-dimensional Navier-Stokes equations given in Appendix A.1.1. Following the procedure in Section 2.1.1, we re-write the equations in terms of the primitive variable set  $Q_p$ , transform to non-conservative form and non-dimensionalize the variables. The resulting set of non-dimensionalized equations in non-conservative form are given as,

$$\begin{aligned}
 & \left( \frac{L}{\tau_r u_r} \right) \left( \tilde{\rho}_p \frac{\partial p}{\partial \tau} + \tilde{\rho}_T \frac{\partial T}{\partial \tau} \right) + \frac{\partial \rho u}{\partial x} = 0 \\
 & \left( \frac{Re_r L}{\tau_r u_r} \right) \rho \frac{\partial u}{\partial \tau} + Re_r \rho u \frac{\partial u}{\partial x} + \left( \frac{Re_r p_r}{\rho_r u_r^2} \right) \frac{\partial p}{\partial x} = \frac{\partial}{\partial x} \left( \mu \frac{\partial u}{\partial x} \right) \\
 & \left( \frac{Re_r Pr_r L}{\tau_r u_r} \right) \left[ - \left( \frac{p_r}{\rho_r h_r} - \rho \tilde{h}_p \right) \frac{\partial p}{\partial \tau} + \rho \tilde{h}_T \frac{\partial T}{\partial \tau} \right] + Re_r Pr_r \rho u \frac{\partial h}{\partial x} - \left( \frac{Re_r Pr_r p_r}{\rho_r h_r} \right) u \frac{\partial p}{\partial x} \\
 & \quad = \frac{\partial}{\partial x} \left( \kappa \frac{\partial T}{\partial x} \right) - \frac{Pr_r u_r^2}{h_r} \mu \left( \frac{\partial u}{\partial x} \right)^2
 \end{aligned} \tag{3.8}$$

where we have now written the terms in the momentum and energy equations such that the diffusion terms are unity. As a result, some of the dimensionless quantities that appeared in Eqn. 2.5 have been modified. In addition, we have introduced several new dimensionless quantities. The Reynolds number,  $Re_r = \rho_r u_r L / \mu_r$ , and the Prandtl number,  $Pr_r = \kappa_r T_r / \mu_r h_r$ , are parameters used to define the flow conditions. In addition, we also have a dimensionless kinetic energy term,  $(u_r^2 / h_r)$ .

We now consider the regime in which the local Reynolds number is small or, in other words, the viscous effects dominate the convective effects. Specifically, we require that the Reynolds number be order one or smaller. Analogous to the low Mach number perturbation procedure, we predicate our viscous analysis on ensuring that the equations

remain well-balanced in the viscous limit. In the momentum equations, for example, the required balance is no longer between the convective terms and the pressure gradient, but is between the diffusive terms and the pressure gradient. Further, we will also require that the time derivative be of the same order as the dominant physical terms to be effective in removing errors from the flowfield.

We again start with the momentum equation and expand the pressure in a perturbation series,

$$p = p_0 + \epsilon_v p_1 + \dots \quad (3.9)$$

where we have used a different small parameter,  $\epsilon_v$ , which will be determined by balancing the pressure gradient with the diffusion term.

Inserting the pressure expansion into the momentum equation, we get,

$$\left(\frac{Re_r L}{\tau_r u_r}\right) \rho \frac{\partial u}{\partial \tau} + Re_r \rho u \frac{\partial u}{\partial x} + \left(\frac{Re_r p_r}{\rho_r u_r^2}\right) \epsilon_v \frac{\partial p_1}{\partial x} = \frac{\partial}{\partial x} \left(\mu \frac{\partial u}{\partial x}\right) \quad (3.10)$$

where we again conclude that the zeroth order pressure must be constant.

The requirement that the pressure gradient balance the diffusive term is ensured by choosing  $\epsilon_v$  so that the coefficient of the pressure term in Eqn. 3.10 becomes unity. Therefore, we get,

$$\epsilon_v = \frac{\rho_r u_r^2}{p_r} \frac{1}{Re_r} \quad (3.11)$$

Along with the condition that  $Re_r \leq \mathcal{O}(1)$ , the viscous perturbation procedure then implies that  $\epsilon_v \ll 1$ . Note that for ideal gases, we get  $\epsilon_v = \gamma M_r^2 / Re_r$ . Thus, the limiting condition of interest is obtained when  $M_r^2 \ll Re_r$  and  $Re_r \leq \mathcal{O}(1)$ . We point out that other perturbation expansions are possible for the limit where  $Re_r \ll M_r^2$  and  $Re_r \leq \mathcal{O}(1)$ . Here, the perturbation expansion would need to include the first-order velocity. While such conditions may exist for transonic and hypersonic, viscous-dominated flows, our current analysis is aimed at low-speed, viscous-dominated flows.

We further note that we continue to define the reference pressure,  $p_r$ , as the thermodynamic pressure and the reference enthalpy,  $h_r = p_r / \rho_r$ . Under these conditions, these choices would imply that the dimensionless term,  $(u_r^2 / h_r)$ , which is the coefficient of the viscous dissipation terms in the energy equation, would be vanishingly small. Finally, we require that the time-derivative term in Eqn. 3.10 also be order one to adequately balance the diffusion and pressure gradient terms. This condition gives,

$$\tau_r = \frac{L}{u_r} Re_r = \frac{\rho_r L}{\mu_r} \quad (3.12)$$

Thus, the characteristic time scale for the viscous limit is the diffusion time scale.

Applying Eqns. 3.11 and 3.12 to the momentum equation, Eqn. 3.10, we get,

$$\rho \frac{\partial u}{\partial \tau} + Re_r \rho u \frac{\partial u}{\partial x} + \frac{\partial p_1}{\partial x} = \frac{\partial}{\partial x} \left(\mu \frac{\partial u}{\partial x}\right) \quad (3.13)$$

Again, the presence of the first-order pressure term in the pressure implies that we need a means of updating it.

Turning now to the continuity equation, we note that the equation is,

$$\frac{1}{Re_r} \left( \tilde{\rho}'_p \epsilon_v \frac{\partial p_1}{\partial \tau} + \tilde{\rho}_T \frac{\partial T}{\partial \tau} \right) + \frac{\partial \rho u}{\partial x} = 0 \quad (3.14)$$

where the  $1/Re_r$  scale pre-multiplying the time-derivative appears as a consequence of the time-scale definition (Eqn. 3.12). Note that we have also introduced  $\tilde{\rho}'_p$  in place of the physical property derivative in anticipation of re-scaling the time-derivative. For now, we take  $\tilde{\rho}'_p = \tilde{\rho}_p$ . From the definition of  $\epsilon_v$ , it is evident that the pressure time-derivative is multiplied by a term of  $\mathcal{O}(M_r^2/Re_r^2)$  (for compressible flow), which approaches zero if  $M_r \ll Re_r$ . Note that the latter condition is less stringent than our limiting condition ( $M_r^2 \ll Re_r$ ). When  $M_r$  and  $Re_r$  are of comparable magnitude, we expect the system to be well-behaved. However, when  $M_r \ll Re_r$ , the equation does not provide an adequate means of updating the first-order pressure and it becomes necessary to modify the time-derivatives.

We further note that if inviscid preconditioning were used under these circumstances,  $\tilde{\rho}'_p = (k_i p_r / \rho_r u_r^2)$ , which is  $\gamma M_r^2$  for ideal gases. Then, the coefficient of the pressure time-derivative becomes  $\mathcal{O}(1/Re_r^2)$ . Although this provides a means of updating the pressure, the large magnitude of this term at low Reynolds numbers indicates that the system will become stiff. Again, this suggests the need for an alternate preconditioning definition for the viscous limit.

To properly define the artificial property term,  $\tilde{\rho}'_p$ , we require that the coefficient of the time-derivative be the same order as the divergence of  $\rho u$ . This gives,

$$\tilde{\rho}'_p = k_v \frac{Re_r}{\epsilon_v} = k_v \frac{Re_r^2 p_r}{\rho_r u_r^2} \quad (3.15)$$

where  $k_v$  is a constant of order one. In dimensional form, this parameter is  $\rho'_p = k_v Re_r^2 / u_r^2$ . For ideal gases, this is equivalent to  $\rho'_p = k_v Re_r^2 \rho_p / \gamma M_r^2$ , where  $\rho_p = 1/RT$ . We employ this definition for Reynolds numbers less than unity. When the Reynolds number is unity, the definition becomes the same as the definition of the inviscid preconditioning parameter (Eqn. 2.14). At Reynolds numbers greater than unity, we no longer exercise the viscous control given in Eqn. 3.15, but transition to the inviscid definition in Eqn. 2.14.

There is usually no further need to alter the time-derivatives of the energy equation since for most fluids  $Pr_r$  is order one. However, if the Prandtl number is much greater or less than unity, it should be possible to re-scale the  $\tilde{h}_T$  property derivative as follows,

$$h'_T = \frac{k_h}{Pr_r} h_T \quad (3.16)$$

where  $k_h$  is a constant of order one.

### 3.2.2 Characteristics of the Preconditioned System

The viscous perturbation equations may be written in vector form as,

$$\tilde{\Gamma}_p \frac{\partial \tilde{Q}_p}{\partial \tau} + \tilde{A} \frac{\partial \tilde{Q}_p}{\partial x} = \frac{\partial}{\partial x} \left( \tilde{R}_{xx} \frac{\partial \tilde{Q}_p}{\partial x} \right) \quad (3.17)$$

where the matrices are defined as,

$$\tilde{\Gamma}_p = \begin{pmatrix} \frac{1}{Re_r} \tilde{\rho}'_p \epsilon_v & 0 & \frac{1}{Re_r} \tilde{\rho}_T \\ 0 & \rho & 0 \\ -Pr_r(1 - \rho \tilde{h}_p) \epsilon_v & 0 & Pr_r \rho \tilde{h}_T \end{pmatrix}$$

and

$$\tilde{A} = \begin{pmatrix} u \tilde{\rho}_p \epsilon_v & \rho & u \tilde{\rho}_T \\ 1 & Re_r \rho u & 0 \\ -Re_r Pr_r(1 - \rho \tilde{h}_p) \epsilon_v & 0 & Re_r Pr_r \rho u \tilde{h}_T \end{pmatrix} \quad \tilde{R}_{xx} = \begin{pmatrix} 0 & 0 & 0 \\ 0 & \mu & 0 \\ 0 & 0 & \kappa \end{pmatrix}$$

where we have dropped the viscous dissipation terms in the energy equation. Further, in the viscous limit of interest here, all the  $\epsilon_v$  terms in the above equations are small and may be dropped, with the exception of the pressure time-derivative in the continuity equation. As discussed in the previous section, viscous preconditioning procedures ensure that this term is order one.

To ensure that the viscous preconditioning procedure yields a well-conditioned system for time-marching computations, we now obtain linearized solutions of the above perturbation form of the Navier-Stokes equations. The procedure is similar to that followed in Section 3.1.1. We start with the linearized constant coefficient version of Eqn. 3.17 and use the following Fourier decomposition,

$$Q_p(x, t) = \hat{Q}_p \exp[ik(x - \alpha t)]$$

where  $k$  is the Fourier wavenumber and  $\alpha$  is the complex phase speed. The real part of  $\alpha$  contains the phase velocity, while the imaginary part describes growth or decay of the perturbation. When the imaginary part of  $\alpha$  is negative, the solution decays with time and convergence is possible.

The roots of the dispersion relation, obtained by substituting the Fourier decomposition into Eqn. 3.17, are given as,

$$\alpha_1 = u Re_r \left(1 - i \frac{(k \Delta x)}{Pr_r Re_{\Delta x}}\right) \quad (3.18)$$

and

$$\alpha_{2,3} = \frac{u Re_r}{2} \left[ \left(1 - i \frac{(k \Delta x)}{Re_{\Delta x}}\right) \pm \sqrt{\left(1 - i \frac{(k \Delta x)}{Re_{\Delta x}}\right)^2 + \frac{4}{Re_r \epsilon_v \tilde{\rho}'_p}} \right]$$

These roots control the phase speed and the rate of damping of solutions of the Navier-Stokes equations in the viscous limit.

The first root is the particle mode, which has the particle velocity as the real part. At low Reynolds number, the imaginary part assumes greater importance and, because of the negative sign, we observe that this term corresponds to a damping mode. In particular, the damping mode scales as  $1/Re_{\Delta x}$ , which means that the smaller the Reynolds number, the greater the damping. The remaining two roots are the “acoustic” modes,

which represent a more complex mixture of propagation and damping characteristics. By examining the roots, it is possible to discern that, at low Reynolds numbers, the acoustic modes also scale as  $1/Re_{\Delta x}$  if the preconditioning parameter,  $\tilde{\rho}'_p = Re_r/\epsilon_v$ . With this viscous preconditioning choice, all the modes are therefore convected or damped at commensurate rates, which indicates good conditioning and reliable convergence behavior. Other choices of  $\tilde{\rho}'_p$  results in poor scaling of the acoustic modes and, hence, in unreliable convergence behavior.

### 3.2.3 Analysis of Artificial Dissipation Models

We have hitherto employed the perturbation equations to investigate the convergence behavior in the viscous limit. We have derived the proper form of the viscous preconditioning terms in this limit and shown that it renders the system well-conditioned for time-marching computations. In this section, we employ the perturbation equations to verify that the artificial dissipation terms are well-behaved as well. Although we are investigating the viscous limit, the form of the artificial dissipation terms are still important for ensuring accuracy. Specifically, we note that the selection of the viscous preconditioning parameter influences the definition of the artificial dissipation terms and it is necessary to verify that this is beneficial or, at least, not deleterious to solution accuracy. As we did in the case of the low Mach number limit, we first discuss central difference schemes and then consider upwind flux-difference schemes.

#### Central Difference Schemes

The central difference scheme with fourth-order artificial dissipation added is the same as Eqn. 2.17, except that we now have the physical viscous terms as well (see Eqn. 3.17). The dissipation terms in the continuity, momentum and energy equations take the following form:

$$\begin{aligned} AD_{\text{cont}} &= \epsilon_e^4 \Delta x^3 |a_r| [\tilde{\rho}'_p \frac{\epsilon_v}{Re_r} \frac{\partial^4 p_1}{\partial x^4} + \tilde{\rho}_T \frac{1}{Re_r} \frac{\partial^4 T}{\partial x^4}] \\ AD_{\text{mom}} &= \epsilon_e^4 \Delta x^3 |a_r| \rho \frac{\partial^4 u}{\partial x^4} \\ AD_{\text{energy}} &= \epsilon_e^4 \Delta x^3 |a_r| Pr_r \rho \tilde{h}_T \frac{\partial^4 T}{\partial x^4} \end{aligned} \quad (3.19)$$

where we have dropped the small  $\epsilon_v$  terms in the energy equation.

We note that the eigenvalues of the Jacobian,  $\tilde{\Gamma}_p^{-1} \tilde{A}$ , are  $uRe_r$  and  $\lambda_{\pm}$ , where,

$$\lambda_{\pm} = \frac{1}{2} [uRe_r \pm \sqrt{(uRe_r)^2 + \frac{4Re_r}{\epsilon_v \tilde{\rho}'_p}}] \quad (3.20)$$

Typically, the spectral radius of the Jacobian,  $|a_r| = \lambda_+$ .

Without preconditioning,  $\tilde{\rho}'_p$  is order one and  $|a_r|$  is  $\mathcal{O}(Re_r/M_r)$ . Thus, depending upon whether  $Re/M \gg 1$  or  $\ll 1$ , we may add too much or too little dissipation. In

particular, when  $Re/M \gg 1$ , we add too much artificial dissipation in the momentum equation and too little for the pressure field in the continuity equation. In other words, the artificial dissipation terms may overwhelm the physical dissipation terms in the momentum equation, while in the continuity equation, the pressure field develops odd-even splitting errors because there are no physical dissipation terms present.

When inviscid preconditioning is used,  $\tilde{\rho}'_p = 1/\gamma M_r^2$  (for ideal gases), which means the velocity scale,  $|a_r|$  goes as  $Re_r$ . In that case, the coefficient of the pressure derivative in the continuity equation scales as  $1/Re$ , which means that too much dissipation is added in the continuity equation. Indeed, we have experienced difficulties with conserving global mass for viscous-dominated problems with this choice of preconditioning.

Finally, when viscous preconditioning is used,  $\tilde{\rho}'_p = Re_r^2/\gamma M_r^2$ , which means that  $|a_r|$  is order one. The coefficient of the pressure derivative term in the continuity equation is also order one as is the dissipation term in momentum and energy. Thus, all the dissipation terms are well-proportioned when the appropriate preconditioning is used and, in general, accuracy is better preserved when compared with the other preconditioning choices. Practical computations have verified these findings.

### Upwind Flux-Difference Schemes

The upwind difference representation of the convective terms in the Navier-Stokes equations is similar to that given in Eqn. 2.19. The matrix dissipation term corresponding to the equations in the viscous limit are given by,

$$\tilde{\Gamma}_p |\tilde{\Gamma}_p^{-1} \tilde{A}| = \begin{pmatrix} \frac{2}{S} & \frac{\rho u}{S} Re_r & u \tilde{\rho}_T \\ \frac{u h_r}{S} & \frac{\rho}{2S}(u^2 Re_r^2 + S^2) & 0 \\ 0 & 0 & \rho u \tilde{h}_T Re_r Pr_r \end{pmatrix} \quad (3.21)$$

where  $S = \sqrt{u^2 Re_r^2 + \frac{4Re_r}{\tilde{\rho}'_p \epsilon_v}}$ .

Again, we observe that if  $\tilde{\rho}'_p$  is selected according to the viscous preconditioning choice,  $S$  is order one and, consequently, all the terms in the matrix are order one or smaller. On the other hand, for other preconditioning choices, one or more terms become too large or too small leading to solution inaccuracies.

#### 3.2.4 Complete Viscous Preconditioning System

The viscous perturbation equations (Eqn. 3.17) may be re-transformed back to the standard conservative form taking care that the system remains applicable at all flow regimes and not just under the limiting conditions. The procedure is the same as for the Euler equations and was described in Section 2.1.6. In fact, the final preconditioned Navier-Stokes equations are identical to Eqn. 2.23 except that we have the diffusion terms in addition. The form of the preconditioning matrix is also identical to that given in Eqn. 2.23. The definition of  $\rho'_p$  is of course different as we have seen in previous sections. In the following section, we consider the practical implementation issues with regard to the definition of the viscous preconditioning parameter.

### 3.3 Implementation of Viscous Preconditioning

The preconditioned Navier-Stokes equations in two dimensions are given as,

$$\Gamma_p \frac{\partial Q_p}{\partial \tau} + \frac{\partial E}{\partial x} + \frac{\partial F}{\partial y} = \mathcal{L}(Q_p) \quad (3.22)$$

where the preconditioning matrix,  $\Gamma_p$  is defined in Eqn. 2.24 and the flux vectors are given in Appendix A.1.2. The definition of the preconditioning parameter  $\rho'_p$  has to be modified to include the diffusion terms and is discussed below.

#### 3.3.1 Definition of the Viscous Preconditioning Parameter

In Section 2.2.2, we defined the preconditioning parameter,  $\rho'_p$ , by specifying an artificial speed of sound,  $(\rho h_T / d')$ . Here, we modify this definition to account for the viscous scales of the problem. As discussed in the previous sections, viscous preconditioning involves scaling the inviscid preconditioning by the Reynolds number squared. Analysis shows that the proper Reynolds number scale to use is the cell-Reynolds number,  $Re_{\Delta x} = u \Delta x / \nu$ . We can incorporate these definitions in the following manner,

$$\frac{\rho h_T}{d'} = V_p^2 \quad (3.23)$$

where the preconditioned velocity scale is given as,

$$V_p = \text{Min}[ \text{Max}(V_{inv}, V_{pgr}, V_{vis}), c ]$$

Here,  $V_{inv}$  is the inviscid velocity scale choice given in Eqn 2.27, while  $V_{pgr}$  is the pressure gradient velocity scale that is defined in Eqn. 2.34.  $V_{vis}$  is the new viscous velocity scale that is given by,

$$V_{vis} = \frac{V}{Re_{\Delta x}} = \frac{\nu}{\Delta x}$$

which is evidently a “diffusion” velocity scale. Note that we may equivalently express the preconditioning through an artificial Mach number,  $M_p = \text{Min}[\text{Max}(M_{inv}, M_{vis}, M_{pgr}), 1]$  with corresponding definitions for the inviscid, viscous and “pressure-gradient” based scales.

Examination of the above expression reveals that the viscous preconditioning essentially “undoes” the inviscid preconditioning making the artificial “sound” speed ( $V_p$ ) approach the physical sound speed. Again, when the velocity scale  $V_p$  exceeds the physical sound speed ( $c^2 = \rho h_T / d$ ), the preconditioned sound speed ( $\rho h_T / d'$ ) is set equal to the physical sound speed (and  $M_p = 1$ ).

#### 3.3.2 Viscous Preconditioning and Time-Step Definition

A useful way to interpret the preconditioning definition is by considering the time-step definition. Typically, CFD codes select the time-step size through a CFL number specification. For viscous problems, when the Reynolds number is low, it is often necessary

to enforce a further restriction on the time-step size by using a viscous time-step or von Neumann number (*e.g.*,  $VNN_x = \nu\Delta\tau/\Delta x$ ). When the wave propagation and viscous damping scales are very disparate, the CFD algorithm is optimized only for the more dominant modes. However, in Section 3.1, we observed that both particle damping modes and acoustic propagation modes remain important for the convergence process in the low-speed, viscous limit. The situation is thus similar to the stiffness problem between particle waves and acoustic waves at low Mach numbers. In the viscous case, it is the stiffness between the acoustic scales and the particle damping scales that causes a convergence slowdown.

Viscous preconditioning is a method of simultaneously optimizing the viscous processes with acoustic wave propagation. To illustrate this, consider the CFL definition,

$$CFL_{\lambda_+} = \frac{\lambda_+ \Delta t}{\Delta x} \quad (3.24)$$

where  $\lambda_+$  is given in Eqn. 2.26. For simplicity, we have considered only the  $x$  direction. At any rate, this does not influence our results very much as long as we limit our discussion to regular sized grids ( $\Delta x = \Delta y$ ). (We will consider high aspect ratio grids ( $\Delta x \gg \Delta y$ ) in the following chapter.)

We note that the magnitude of  $\lambda_+$  is approximately the same as that of the preconditioned velocity,  $\rho h_t/d' = V_p$ . Substituting this term into Eqn. 3.24, we get,

$$CFL_{\lambda_+} \approx \frac{V_p \Delta t}{\Delta x} \quad (3.25)$$

In the low-speed, viscous limit,  $V_p = V_{vis}$ , which is given in Eqn. 3.23. Substituting for  $V_p$  in Eqn. 3.25, we get,

$$CFL_{\lambda_+} \approx \frac{\nu \Delta t}{\Delta x^2} = VNN_x \quad (3.26)$$

Thus, by setting the pseudo-acoustic speed to the viscous “velocity” scale, viscous preconditioning approximately equalizes the acoustic-CFL number with the VNN number. It is interesting to contrast this observation with the fact that, for low Mach number flows, the inviscid preconditioning procedure equalizes the acoustic-CFL number with the particle-CFL number.

In the following section, we use these ideas to further refine the selection of the viscous preconditioning parameter.

### 3.3.3 Enhanced Definition of Viscous Preconditioning Parameter

Equation 3.23 represents a useful manner of defining the viscous preconditioning parameter. However, its limitation is that it controls the time scales indirectly. In particular, CFD algorithms typically have optimal CFL and VNN numbers for best performance. For instance, the ADI algorithm has an optimum CFL number in the range of 5 to 10, while the optimum VNN number is typically between 10 and 100. The explicit four-stage

Runge-Kutta algorithm, on the other hand, has a maximum allowable CFL number of  $2\sqrt{2}$ , while the maximum VNN number is around  $1/3$ . It is therefore desirable to define the viscous preconditioning in such a manner that the relevant time-steps are controlled directly.

To derive the viscous preconditioning, we start from the time-step definitions. Thus, we have,

$$CFL_x = \frac{\lambda_+^x \Delta\tau}{\Delta x} \quad VNN_x = \frac{\nu \Delta\tau}{\Delta x^2} \quad (3.27)$$

Equating the time-step from each expression and substituting for the acoustic eigenvalue in the  $x$  direction ( $\lambda_+^x$ ), we get,

$$\frac{\rho h_T}{d'} = \frac{\alpha(\alpha - 1)}{\alpha - 1 + \frac{\rho h_T}{du^2}} \left( \frac{\rho h_T}{d} \right) \quad (3.28)$$

where  $\frac{\rho h_T}{d} = c^2$  is the physical sound speed squared and  $\alpha$  is defined as,

$$\alpha = \frac{CFL}{VNN} \frac{1}{Re_{\Delta x}}$$

with  $Re_{\Delta x} = u\Delta x/\nu$ .

The above definition specifies the value of the viscous velocity scale,  $V_{vis}$ , by maintaining  $CFL_x$  and  $VNN_x$  at their optimum values. It is the appropriate choice when the dominant time scales are in the  $x$  direction, which is normally the case when the grid aspect ratio ( $AR = \Delta x/\Delta y$ ) is less than unity. When the aspect ratio is greater than unity, the dominant scales are typically in the  $y$  direction and  $CFL_y$  and  $VNN_y$  are the relevant scales to be optimized. Based on these two situations, we may combine the definitions as,

$$V_{vis}^2 = \text{Max} \left[ \frac{\alpha(\alpha - 1)}{\alpha - 1 + \frac{\rho h_T}{du^2}}, \frac{\beta(\beta - 1)}{\beta - 1 + \frac{\rho h_T}{du^2}} \right] \left( \frac{\rho h_T}{d} \right) \quad (3.29)$$

where  $\beta$  is defined as,

$$\beta = \frac{CFL}{VNN} \frac{1}{Re_{\Delta y}}$$

and  $Re_{\Delta y} = v\Delta y/\nu$ .

Equation 3.29 is used in concert with Eqn. 3.23 to define the viscous preconditioning parameter. It is straightforward to confirm that Eqn. 3.29, in fact, approaches  $V^2/Re^2$  in the limit that  $M^2/Re$  is small. The definition given here is appropriate for explicit schemes, but for implicit schemes, we will see in Chapter 4 that additional refinements may be used to further optimize the viscous preconditioning, particularly in the presence of high aspect ratio grid cells.

### 3.4 Analytical Solution of Viscous Preconditioning System

In this section, we present the analytical solution for the preconditioned linearized system following the procedure outlined in Section 3.1. This will enable us to verify that the viscous preconditioning procedures are indeed effective in improving the conditioning of the system. Computational results of practical problems are presented elsewhere in the text (see Chapters 4 and 6).

We follow the same procedure outlined for the preconditioning system in Section 3.1.2, except that we use the viscous preconditioning definition of the parameter, given in Eqn. 3.28, i.e., we write  $\epsilon_p$  as,

$$\epsilon_p = \frac{\alpha(\alpha - 1)}{\alpha - 1 + c^2/u^2} \quad (3.30)$$

and  $\alpha$  is defined in Eqn. 3.28.

Examination of the above expression for  $\epsilon_p$  yields the following limiting circumstances. When  $M^2/Re^2 \ll 1$ ,  $\epsilon_p \rightarrow M^2/Re^2$ , and when  $M^2/R \gg 1$ ,  $\epsilon_p \rightarrow 1/Re$ . We recognize that the former case, which is encountered in low-speed viscous-dominated flows, is the one that we are particularly interested in. We note that  $\epsilon_p$  approaches the correct limiting value for the viscous preconditioning parameter under these circumstances. The second situation arises for viscous-dominated transonic and hypersonic flows and we include it because the results are interesting.

The complex roots of the dispersion relation are the same as those given in Eqn. 3.7. Table 3.4 summarizes the forms that these roots take for different Reynolds and Mach number limits, where the high Reynolds number (inviscid preconditioning) limit has also been included for completeness. We note that for high-Re, all the modes are propagating modes and the inviscid preconditioning choice,  $M_p^2 = M^2$ , ensures good conditioning between the modes. In the low-speed viscous limit ( $Re \leq 1$ ,  $M^2/Re \ll 1$ ), the viscous preconditioning choice,  $M_p^2 = M^2/Re^2$ , causes the particle wave to become a pure damping mode, while the acoustic modes are mixed convective/damping modes. Again, the preconditioning choice ensures good conditioning between these modes. Finally, at the high-speed viscous limit ( $Re \leq 1$ ,  $M^2/Re \gg 1$ ), the preconditioning choice,  $M_p^2 = 1/Re$ , again yields damping modes for the particle waves and mixed modes for the acoustic waves. While the conditioning of the modes are good, it is noteworthy that one of the acoustic modes has a negative damping term, indicating instability. For this reason, this choice may not be reliable in practice. In our implementation, we therefore introduce an upper “cut-off” value to ensure that the equations are not preconditioned in this limit. In other words, the preconditioning parameter  $M_p$  cannot exceed unity and, correspondingly,  $V_p$  cannot exceed the physical sound speed. This choice is reflected in Eqn. 3.23.

Re # limits	$M_p$	$\omega_1/k$	$\omega_2/k$	$\omega_3/k$	Cond. #
$Re \gg 1$	$M^2$	$u$	$\frac{u}{2} (1 + \sqrt{5})$	$\frac{u}{2} (1 - \sqrt{5})$	2.61
$Re \ll 1, \frac{Re}{M^2} \gg 1$	$\frac{M^2}{Re^2}$	$\frac{\hat{u}}{Re}$	$\frac{u}{2Re} (\hat{i} + \sqrt{3})$	$\frac{u}{2Re} (\hat{i} - \sqrt{3})$	1
$Re \ll 1, \frac{Re}{M^2} \ll 1$	$\frac{1}{Re}$	$\frac{\hat{u}}{Re}$	$\frac{u}{2Re} (-0.34 + \hat{i}2.34)$	$\frac{u}{2Re} (2.34 - \hat{i}0.34)$	1.18

Table 3.3: Preconditioned Navier-Stokes

# Chapter 4

## Effects of High Grid Aspect Ratio on Convergence

High aspect ratio grids are commonly encountered in high-Reynolds number wall-bounded flows, wherein the grid must be refined very tightly in the direction normal to the wall to resolve the steep velocity gradient. A second type of problem in which high grid aspect ratio cells are encountered is in flowfields that are very long in relation to their cross-sectional dimensions, for example, internal flows in ducts. In both instances, the high aspect ratio of the grid causes a strong disparity in the wave propagation speeds (or, more precisely, in the grid-crossing time scales) in the two coordinate directions causing serious convergence deterioration. In this chapter, we examine grid aspect ratio effects on convergence. We use stability analysis to investigate the grid aspect ratio performance of several classes of schemes ranging from central-difference ADI to upwind Gauss-Seidel relaxation methods. We further determine how aspect ratio effects may be addressed through proper definition of the time-step and preconditioning.

### 4.1 The Problem of High Aspect Ratios

High grid aspect ratios are commonly encountered when solving high Reynolds number flows of practical interest. For example, boundary layers and shear layers often require strong grid stretching in one coordinate direction in order to resolve the high gradient regions. This local grid stretching often results in very large grid aspect ratios within the thin viscous layer. The magnitude of these grid aspect ratios may be on the order of 100 to 1000, but can reach values of  $1 \times 10^6$  for high Reynolds number, turbulent flows.

For two-dimensional problems, the grid aspect ratio (AR) may be defined as,

$$AR = \frac{\Delta x}{\Delta y}$$

In the case of three-dimensional problems, the added dimension gives rise to several types of high aspect ratio grid cells. For purposes of interpretation three high aspect ratio cell

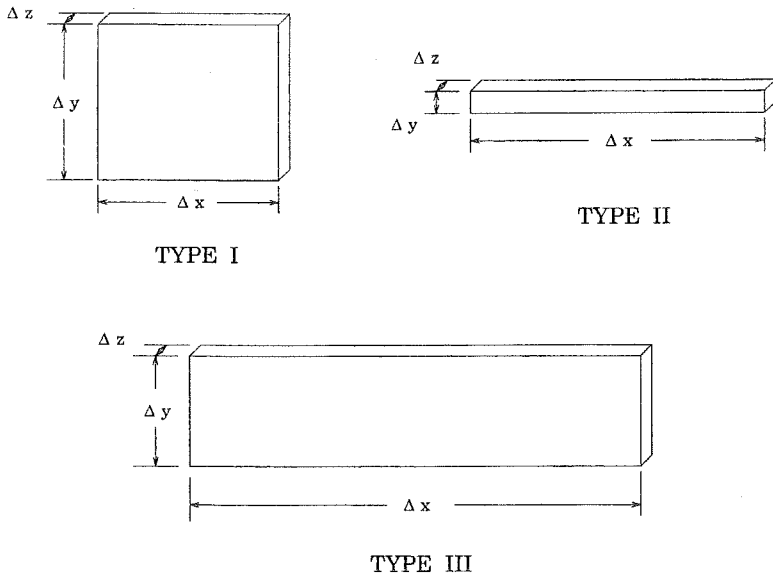


Figure 4.1: Three types of high aspect ratio cells for three-dimensional problems.

types are defined as follows: Type I, where the cell dimensions are small in one direction and large in the other two ( $\Delta x \& \Delta y \gg \Delta z$ ); Type II, where  $\Delta x \gg \Delta y \& \Delta z$ ; and Type III, where  $\Delta x \gg \Delta y \gg \Delta z$ . For completeness, a fourth type of grid cell is defined as a Type 0 cell. This is the base case where all three cell dimensions are commensurate. Representative examples of these types of three-dimensional high aspect ratio cells are given in Figure 4.1.

The problem with high grid aspect ratios is coupled to the choice of numerical algorithm. Explicit schemes such as Lax-Wendroff or the multi-stage Runge-Kutta schemes have strict stability criteria which require the time-step size to be based on the most restrictive coordinate direction. When the cell aspect ratios are very large, this can lead to exceedingly small time steps, poor damping of errors and very slow convergence. Fully implicit methods that use direct inversion of the left-hand-side (LHS) operator are generally not affected by the stiffness associated with high aspect ratio cells. Their optimum time step is infinite, and the stiffness is readily offset by taking all non-dimensional time steps sufficiently large. Unfortunately, direct inversion of the left-hand-side operator is prohibitively expensive for most multi-dimensional applications and approximate inversion methods have to be used. As we have seen in Chapter 1, most of these approximate methods have optimum time-step sizes, while some others are conditionally stable and have time-step restrictions. These stability restrictions give rise to the stiffness associated with the high aspect ratio cells, which is manifest in slow propagation of errors and poor damping characteristics in one or more coordinate directions.

This effect may be readily understood by considering the CFL definitions in each of the coordinate directions. Local time-stepping is commonly employed to specify a different time step at every grid point. This is generally done by setting the dominant or maximum CFL number at any grid location to a specified “optimum” number. Mathematically,

this max-CFL definition is obtained by computing the minimum time step in the two directions,

$$\Delta t = \text{Min} \left[ \frac{CFL\Delta x}{\lambda_x}, \frac{CFL\Delta y}{\lambda_y} \right] \quad (4.1)$$

Here,  $\lambda_x$  and  $\lambda_y$  are the acoustic eigenvalues in the respective coordinate directions. The CFL number is typically taken to be between 5 and 10 for optimum convergence.

The time step definition in Eq. 4.1 illustrates the problem experienced with high aspect ratio grids. A CFL number can be defined for each coordinate direction:  $CFL_x = \lambda_x \Delta t / \Delta x$  and  $CFL_y = \lambda_y \Delta t / \Delta y$ . Equation 4.1 will set the most restrictive (*i.e.* maximum) of these two CFL's equal to the chosen value of CFL. When the aspect ratio is much greater than unity, the maximum CFL ( $CFL_y$  in this case) is maintained at the optimum value while  $CFL_x$  is very small (*i.e.*,  $CFL_y = \text{CFL}$  and  $CFL_x \approx \text{CFL}/AR$ , assuming that  $\lambda_x$  and  $\lambda_y$  are of the same order). This small value of  $CFL_x$  results in very poor damping (and propagation) of error modes in the  $x$ -direction. The converse situation exists for aspect ratios that are much less than unity. Here,  $CFL_x = \text{CFL}$  and  $CFL_y \approx AR \cdot \text{CFL}$  and errors exhibit poor damping (and propagation) in the cross-stream direction.

In the following sections, we will examine the stability properties of different classes of CFD algorithms. Our primary focus is on implicit methods, although we make some comments regarding the stability and convergence characteristics of explicit schemes as well.

## 4.2 Two-Dimensional ADI Scheme

Von Neumann vector stability analysis is used to determine the stability properties of the centrally-difference ADI scheme in the presence of high grid aspect ratios and to suggest any modifications. This will be followed by numerical test cases to reveal any further difficulties, and to test the performance of the enhancements. To illuminate the separate contributions of the convective and diffusive terms, we first consider the Euler equations and treat the convective terms alone. We then turn to the complete Navier-Stokes equations where both convective and diffusive effects are present. Following the analysis of the central-difference ADI scheme, approximate factorization techniques for various candidate upwind schemes will be investigated in a similar manner [50].

### 4.2.1 Euler Equation Stability Analysis

The stability characteristics of the preconditioned Euler equations (Eqn. 2.24 based on the ADI approximate factorization scheme (Eqn. 1.8) were given in Fig. fig:2.1 for a grid aspect ratio of unity. Corresponding high aspect ratio stability results (for  $AR = 100$ ) are given in Figs. 4.2 and 4.3. Here, the CFL numbers in each coordinate direction ( $CFL_x$ ,  $CFL_y$ ) must be distinguished. The standard time-step definition given in Eqn. 4.1 places an upper bound on the value of the CFL number in either coordinate direction. Therefore, this time-step definition will be referred to as the max-CFL definition. Thus,

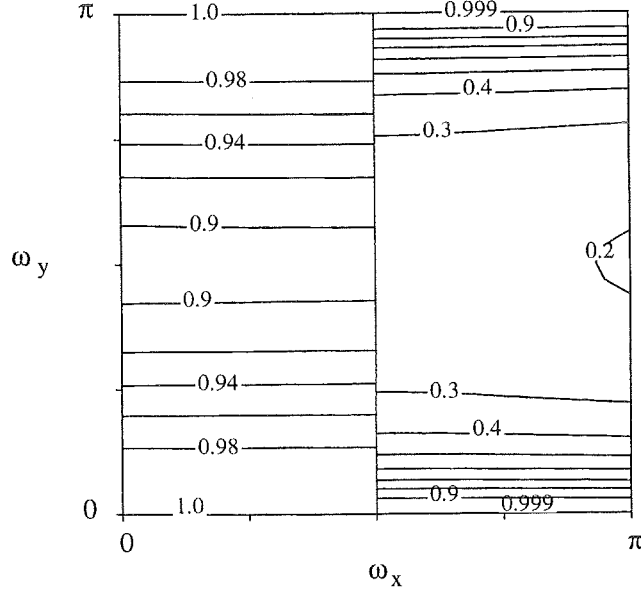


Figure 4.2: Euler stability for the preconditioned, 2-D centrally-differenced ADI scheme with  $AR=100$ ,  $M=0.001$ ,  $v/u=1$ . Left side:  $CFL_x=0.01$ ,  $CFL_y=1$ ; Right side:  $CFL_x=0.1$ ,  $CFL_y=10$ .

Fig. 4.2 shows the results for max-CFL of 1 (left half) and 10 (right half). This results in  $CFL_x=0.01$  and  $CFL_y=1$  for the left half of the figure, and  $CFL_x=0.1$ ,  $CFL_y=10$  for the right half of the figure.

For both of the cases in Fig. 4.2, the amplification factor approaches unity along the abscissa of the stability diagram. These results imply that the scheme possesses fairly good damping of cross-stream disturbances but very poor damping of longitudinal (or streamwise) disturbances, a consequence of the low  $CFL_x$  values. It is interesting that, in spite of the higher CFL on the right half in Fig. 4.2, the effect of approximate factorization is not evident as it is in Fig. 2.1.

Stability results for max-CFL=100 and 300, are shown in Fig. 4.3. Here,  $CFL_x=1$ ,  $CFL_y=100$  on the left half and  $CFL_x=3$ ,  $CFL_y=300$  on the right half. Despite the high max-CFL value, the amplification factors on the left still show little evidence of the approximate factorization error. The amplification factor is, in fact, well-conditioned not only over the mid wave-numbers but is now also well-conditioned for purely longitudinal waves. This latter result is a consequence of the fact that  $CFL_x$  is unity. In the right half of Fig. 4.3, the effect of approximate factorization is more apparent, but the amplification factors still suggest good damping, with improved damping of longitudinal modes. At still higher CFL numbers (not shown), the AF errors start to have more impact and eventually cause the amplification factor to approach unity over the entire wavenumber domain.

The above results suggest that the optimum CFL number is function of the aspect ratio. Thus, for an aspect ratio of 100, the optimum max-CFL (i.e.  $CFL_y$ ) lies between 100 and 1000. The corresponding optimum  $CFL_x$  lies between 1 and 10. As a further

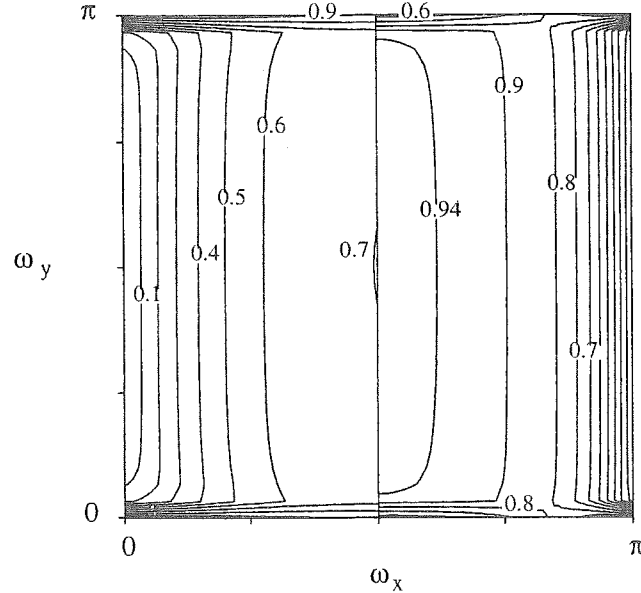


Figure 4.3: Euler stability for the preconditioned, 2-D centrally-differenced ADI scheme with AR=100, M=0.001,  $v/u=1$ . Left side:  $\text{CFL}_x=1$ ,  $\text{CFL}_y=100$ ; Right side:  $\text{CFL}_x=3$ ,  $\text{CFL}_y=300$ .

check of this conclusion, results are presented for an aspect ratio of  $1 \times 10^4$  in Figure 4.4, where  $\text{CFL}_y=3 \times 10^4$  and  $\text{CFL}_x=3$ . Again, the stability suggests good damping, and the amplification factors are almost identical to the AR=100 results shown in the right half of Fig. 4.3. Thus, if the optimum max-CFL is 3 for an aspect ratio of unity, then for AR=100, it would be 300 and for AR= $1 \times 10^4$ , the optimum max-CFL would be  $3 \times 10^4$ .

For all of the above cases, the optimum time step size may equivalently be obtained by choosing the minimum CFL (*i.e.*,  $\text{CFL}_x$ ) to be about 3. In particular, this surprising result indicates that, if the local time step is chosen carefully, the ADI scheme will not suffer convergence deterioration at any grid aspect ratio. The conclusion from these results is that the constant value of CFL which should be used for all aspect ratios is the one based on the minimum of  $\text{CFL}_x$  and  $\text{CFL}_y$ , not the maximum. Mathematically, this time-step definition may be enforced by selecting the maximum  $\Delta t$  in the two directions rather than the minimum (as in Eqn. 4.1):

$$\Delta t = \text{Max} \left[ \frac{\text{CFL} \Delta x}{\lambda_x}, \frac{\text{CFL} \Delta y}{\lambda_y} \right] \quad (4.2)$$

Hereafter, this definition will be referred to as the min-CFL time-step in contrast the more commonly used max-CFL definition in Eqn. 4.1. Note that the min-CFL definition automatically accounts for both longitudinally and transversely stretched grids.

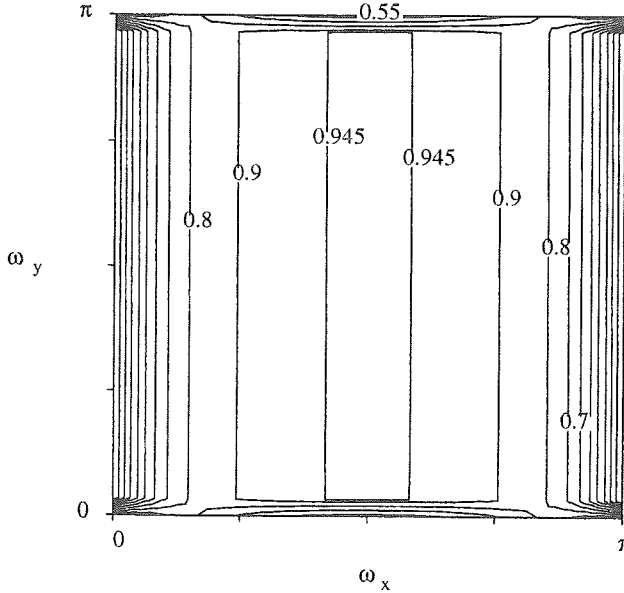


Figure 4.4: Euler stability for the preconditioned, 2-D centrally-differenced ADI scheme with  $AR=1 \times 10^4$ ,  $M=0.001$ ,  $v/u=1$ .  $CFL_x=3$ ,  $CFL_y=3 \times 10^4$ .

#### 4.2.2 Euler Convergence Studies

The findings from the stability analyses are now investigated by considering the seemingly trivial problem of the solution of the Euler equations for uniform flow in a straight channel. By varying the aspect ratio of the channel while maintaining a fixed grid size ( $41 \times 41$ ), the local grid aspect ratio is arbitrarily increased from unity to  $1 \times 10^4$  (see Fig. 4.5). The initial condition used for all calculations is uniform flow plus a 10% perturbation pressure pulse in the center of the domain.

Figure 4.6 shows convergence using the max-CFL time-step definition (Eqn. 4.1) with the max-CFL=3 for grid aspect ratios ranging from unity to 100. It is clear from the figure, that the convergence deteriorates rapidly as the aspect ratio is increased. An examination of the residual errors for pressure, as seen in Fig. 4.7, reveals that the longitudinal modes are controlling the convergence. This supports the above stability results (Fig. 4.2) which showed that cross-stream disturbances are well-damped while streamwise (or longitudinal) modes remain stiff when using moderate values of the max-CFL. The rapid decrease in error at the onset occurs because the transverse errors are being damped more rapidly as the AR increases.

The convergence for this case can be improved by simply choosing the max-CFL to be on the order of the grid aspect ratio, or by fixing the min-CFL to be around 3-4 for all aspect ratio cases. The convergence results for min-CFL=3 are shown in Fig. 4.8 for aspect ratios ranging from unity to  $1 \times 10^4$ . As suggested by the stability analysis, the convergence rate is essentially independent of the grid aspect ratio (for 2D computations) when using the min-CFL time-step definition. In closing, we note that, although these results were

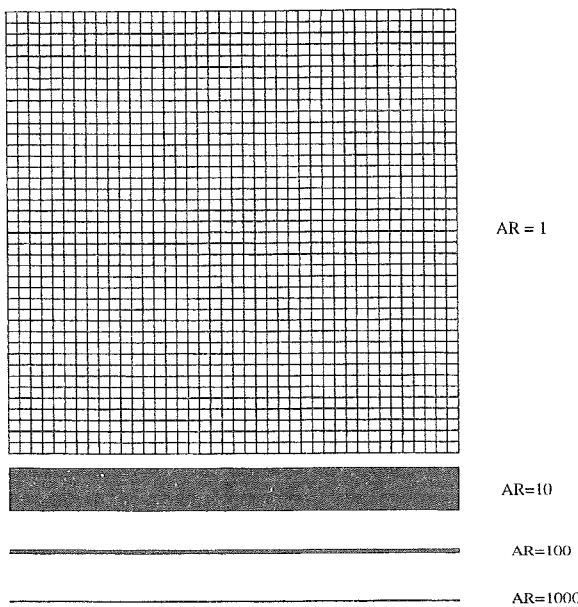


Figure 4.5: Grid geometry ( $41 \times 41$ ) for the straight channel cases showing aspect ratios from unity to 1000.

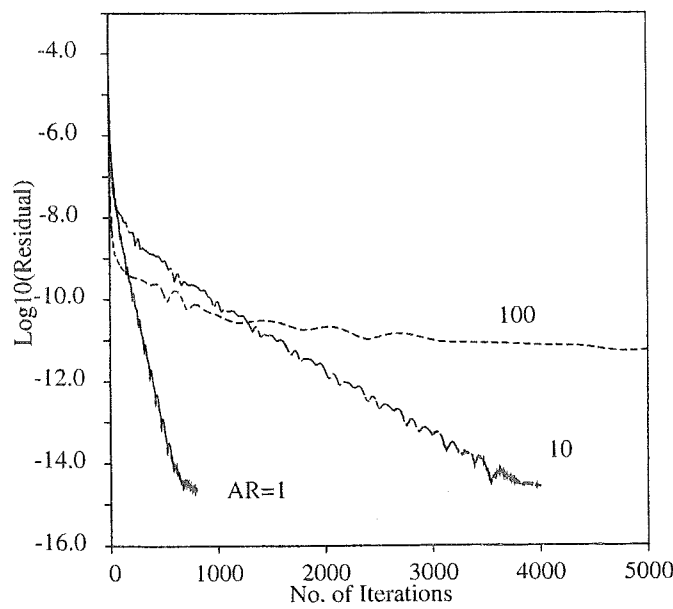


Figure 4.6: Convergence for the inviscid straight channel cases at aspect ratios from unity to 100, using  $\text{max-CFL}=3$ .

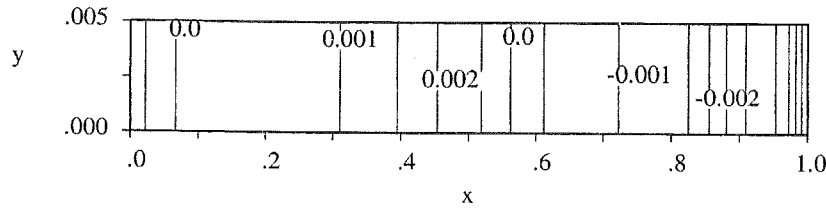


Figure 4.7: Contours of the residual errors for the pressure for the AR=100 case, using max-CFL=3. Errors are purely one-dimensional, longitudinal modes.

obtained at low Mach numbers using the preconditioned equations, the conclusions remain the same for flows at all Mach numbers.

#### 4.2.3 Navier-Stokes Stability Analysis

An important issue in high aspect ratio Navier-Stokes computations is the significance of viscous preconditioning. High aspect ratio problems are generally dominated by viscous processes in the cross-stream direction (this is why highly stretched grids are employed), even when the stream-wise Reynolds number is high. The purpose of viscous preconditioning is to optimize the inviscid and viscous modes of the problem simultaneously. For regular-sized grids, the maximum inviscid and viscous time scales are optimized by the viscous preconditioning parameter given in Eqn. 3.29. For high aspect ratio grids, the question of which scales must be optimized is not as clear, especially in light of the above findings for the inviscid equations. In this section, the definition of the viscous preconditioning parameter is considered for high aspect ratio situations.

Both scalar and vector analyses of the inviscid equations indicate that the optimum CFL number may be obtained for all grid aspect ratios by fixing the minimum CFL rather than the maximum. A similar analysis of a scalar diffusion equation shows that the optimum  $VNN$  is likewise properly determined by the minimum  $VNN$ . Furthermore, for a combined scalar convection-diffusion equation, the optimum time step may be determined by choosing the more restrictive among the min-CFL and min- $VNN$  time steps. Unfortunately this simple redefinition of the time step does not carry over directly to the Navier-Stokes equations.

Stability results for the full Navier-Stokes equations are given in Fig.4.9 for AR=1000 using this min-CFL/min- $VNN$  definition. This condition may be enforced by selecting the minimum viscous preconditioning choice in Eqn. 3.29 rather than the maximum choice. The conditions used in Fig. 4.9 are  $M = 0.001$  and a stream-wise cell-Reynolds number ( $Re_{\Delta x}$ ) of 100. Also,  $CFL_x=1$ ,  $VNN_x=1$  ( $CFL_y=1000$  and  $VNN_y=1 \times 10^6$ ). The result shows good damping over most of the wave-number domain except for a stiff region at the top of the domain around the  $(\pi/2, \pi)$  point where the amplification factor approaches unity.

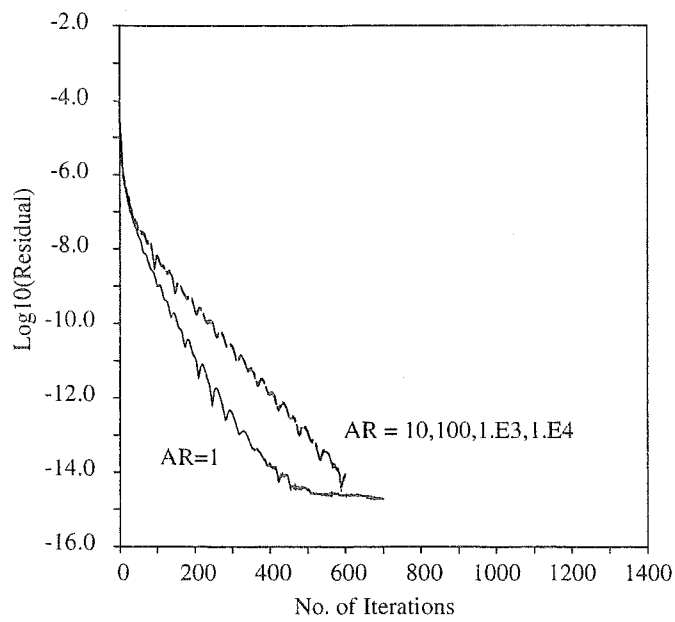


Figure 4.8: Convergence for the inviscid straight channel cases at aspect ratios from unity to  $1 \times 10^4$ , using min-CFL=3.

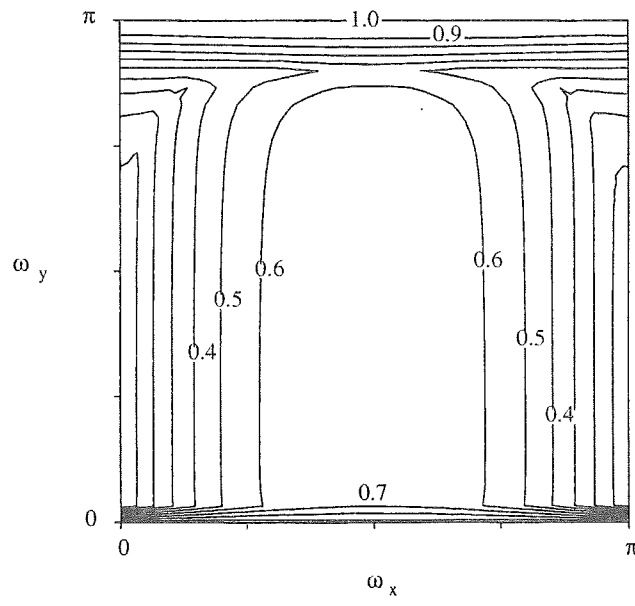


Figure 4.9: Contours of the maximum absolute eigenvalue of the amplification matrix for the preconditioned Navier-Stokes stability of the 2-D central difference ADI scheme. AR=1000, M=0.001,  $v/u=1$ ,  $Re_{\Delta x}=100$ ,  $CFL_x=1$ ,  $VNN_x=1$ .

Careful examination of the approximate factorization errors of the Navier-Stokes algorithm reveals that the source of this stiffness is the error term arising from the cross-product of the streamwise inviscid term and the cross-stream viscous term. The magnitude of this error term is approximately indicated by the product of  $CFL_x$  and  $VNN_y$ . Because  $VNN_y$  is large, the error term dominates the other terms in the equation. Exact analysis is difficult for the vector system but this indicates that scalar results do not always carry over to the vector system.

Experiments with a preconditioned Navier-Stokes code for high aspect ratio viscous channel flow indicate that the min-CFL/min-VNN time-step definition indeed does not perform well. In fact, solutions often diverge. It is possible that the instability is related to lack of robustness due to the large values of the cross-stream VNN number, but the stiffness problem probably exacerbates the situation. Indeed, we have had moderate success with the min-CFL/min-VNN condition if a good initial condition is provided for the problem. In practice, this means that, during the initial computational stages, it is preferable to use a more conservative definition, such as the max-CFL/max-VNN combination, or perhaps, the min-CFL/max-VNN definition suggested below. Once the solution “settles” down, it becomes possible to switch to the more aggressive min-CFL/max-VNN combination.

The observation regarding the source of the difficulty suggests, however, that the error term may be minimized by reducing  $VNN_y$ . This is achieved by specifying the maximum-VNN rather than the minimum, while continuing to specify the minimum-CFL number. Such a definition, which will be referred to as min-CFL/max-VNN, retains the benefits of the min-CFL definition for the ‘inviscid’ modes of the problem while maintaining the conventional restriction on the maximum allowable VNN for the ‘viscous’ modes.

The min-CFL/max-VNN specification involves selecting the viscous preconditioning so that the appropriate CFL and VNN numbers are optimized. In other words, for high aspect ratios ( $\Delta x \gg \Delta y$ ),  $V_{vis}$  is chosen to maintain  $CFL_x$  and  $VNN_y$  at their specified optimum values, while for small aspect ratios,  $V_{vis}$  is selected to specify  $CFL_y$  and  $VNN_x$ . This condition may be expressed as,

$$V_{vis}^2 = \text{Max} \left[ \frac{\alpha(\alpha - 1)}{\alpha - 1 + \frac{\rho h_T}{du^2}}, \frac{\beta(\beta - 1)}{\beta - 1 + \frac{\rho h_T}{du^2}} \right] \left( \frac{\rho h_T}{d} \right) \quad (4.3)$$

where  $\alpha$  and  $\beta$  are defined as,

$$\alpha = \frac{CFL}{VNN} \frac{AR^2}{Re_{\Delta x}} \quad \beta = \frac{CFL}{VNN} \frac{1}{AR^2 Re_{\Delta y}}$$

with  $AR = \Delta x / \Delta y$ ,  $Re_{\Delta x} = u \Delta x / \nu$  and  $Re_{\Delta y} = v \Delta y / \nu$ .

Stability results for the Navier-Stokes equations using this new min-CFL/max-VNN definition are shown in Fig. 4.10 for AR=1000. The amplification factors are for  $CFL_x=1$  and  $VNN_y=1$  ( $CFL_y=1000$ ,  $VNN_x=1 \times 10^{-6}$ ) and are seen to be well-conditioned except for the region along the abscissa where they approach unity. The stiffness in this region is caused by the small viscous time step in the stream-wise direction and not the approximate factorization error. While this represents a potential problem for high aspect ratio

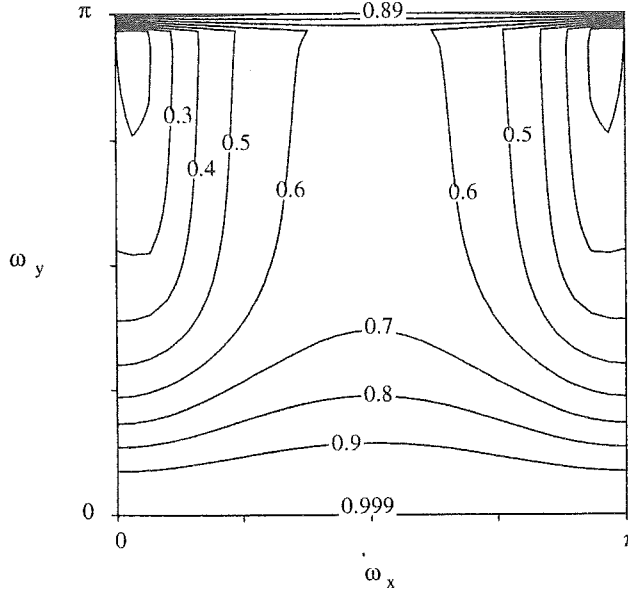


Figure 4.10: Contours of the maximum absolute eigenvalue of the amplification matrix for the preconditioned Navier-Stokes stability of the 2-D central difference ADI scheme. AR=1000, M=0.001,  $v/u=1$ ,  $Re_{\Delta x}=100$ ,  $CFL_x=1$ ,  $VNN_y=1$ .

Navier-Stokes computations, numerical experiments (shown later) indicate that efficient convergence is obtained using this min-CFL/max-VNN time-step.

The success of the min-CFL/max-VNN definition in spite of the longitudinal viscous mode stiffness suggests that these modes may not be important for Navier-Stokes computations. A possible reason for this may be related to the fact that typically, in viscous calculations, the velocity is known along the surface of the wall (because of the no-slip condition). Therefore, longitudinal error modes are eliminated by the boundary condition specification and the algorithm is not called upon to damp out these modes. Indeed, some numerical experiments with strongly stretched grids in non-wall bounded flows have indicated convergence slowdown with the min-CFL/max-VNN choice, lending credence to this theory. In such cases, it is sometimes helps to initiate the computations with the min-CFL/max-VNN definition and then switch to the min-CFL/min-VNN definition as described earlier.

#### 4.2.4 Navier-Stokes Convergence Studies

##### Fully Developed Flow in Straight Channel

Convergence results are again presented to check on the findings from the above stability analyses. Fully-developed viscous flow in a straight channel is computed using a  $41 \times 41$  grid, and the grid aspect ratios are varied from unity to  $1 \times 10^4$  by decreasing the width of the channel while keeping the length constant. Aspect ratios of  $1 \times 10^4$  and higher are

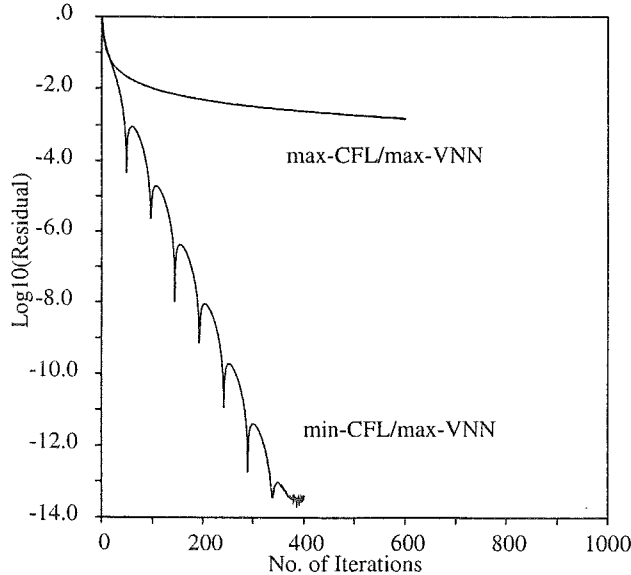


Figure 4.11: Convergence for the fully-developed viscous straight channel case at aspect ratio of 1000 with viscous preconditioning. Standard time-step definition (max-CFL/max-VNN), and improved time-step definition (min-CFL/max-VNN).

often encountered locally in Navier-Stokes computations of turbulent flow. The velocity profile at the inlet is taken to be parabolic, obviating the need for grid stretching near the wall. The Mach number of the flow is  $1 \times 10^{-3}$  and the stream-wise cell Reynolds number,  $Re_{\Delta x}$ , is 100. The cross-stream cell Reynolds number,  $Re_{\Delta y}$ , ranges from 100 to  $10^{-2}$  depending on the grid aspect ratio.

Figure 4.11 shows a comparison of convergence rates for the algorithm with the standard time-step definition based on the max-CFL and the max-VNN, and the algorithm with the min-CFL/max-VNN time-step definition. Viscous preconditioning was used in both cases, and the grid aspect ratio was set to 1000. The improved algorithm with the min-CFL/max-VNN definition converges faster than the standard algorithm by a factor of about 500. Convergence at aspect ratios ranging from unity to  $1 \times 10^4$  are shown in Figure 4.12 using the min-CFL/max-VNN definition. At all aspect ratios the algorithm converges extremely well.

### Multi-Species Shear Layer

Having established the performance of the enhanced algorithm for simple cases, more realistic flow-fields are now considered. The first case is a multi-species, non-reacting shear-layer. The shear-layer consists of co-flowing streams of hydrogen and oxygen. The Mach number of both streams is 0.1 and the grid size is  $61 \times 61$ . Grid stretching is employed at the interface between the two streams to resolve the shear layer and different values of the stretching parameter are used for different Reynolds numbers. The solutions

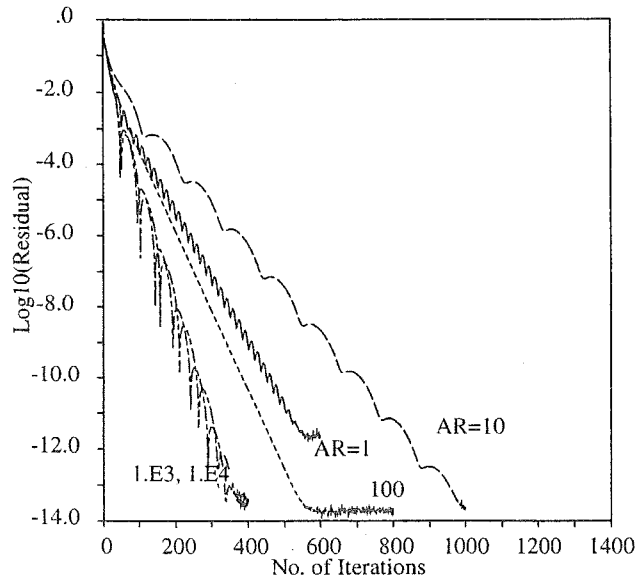


Figure 4.12: Convergence for the fully-developed viscous straight channel cases at aspect ratios from unity to  $1 \times 10^4$ , using min-CFL/max-VNN.

for three different Reynolds numbers (200, 2000 and 20,000 based on the width of the oxygen stream) are shown in Fig. 4.13. The corresponding maximum grid aspect ratios are 30, 60, and 100 respectively. The hydrogen profiles in Fig. 4.13 at a given axial location of the flow-field show the extent of species diffusion for the three Reynolds numbers.

The convergence histories for the shear layer are shown in Fig. 4.14. For the enhanced algorithm (min-CFL/max-VNN and MOC II boundary conditions), the convergence for all three cases is seen to be very good reaching machine zero in about 1200 iterations. In particular, the different grid aspect ratios (shown in parenthesis) for the three cases have no effect on the convergence rate.

The other convergence curves shown in Fig. 4.14 are for the  $Re = 200$  case with one or more aspects of the enhanced algorithm turned off. Curve II is for the standard preconditioned algorithm (max-CFL/max-VNN). The corresponding convergence is about a factor of three slower even though the maximum grid aspect ratio for this case is only 30. Thus, even for this simple case, the savings in CPU time can be quite substantial. The remaining convergence plots in Fig. 4.14 are obtained with the min-CFL time step definition but without viscous preconditioning (curve III) and without any preconditioning (curve IV). These results once again demonstrate the importance of doing “everything” right in order to obtain convergence that is independent of grid aspect ratio.

### Flat Plate Boundary Layers

As a further Navier-Stokes example, we consider both laminar and turbulent flat plate boundary layer flow-fields. Because of the steep velocity gradients near the wall, strong

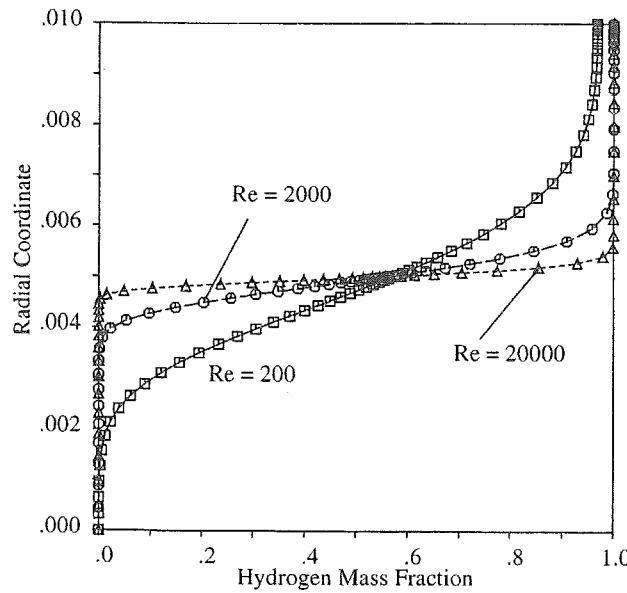


Figure 4.13: Shear layer hydrogen mass fraction profiles

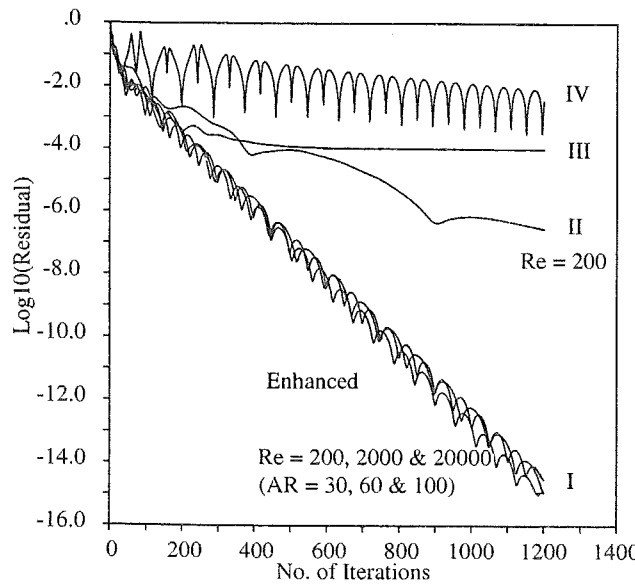


Figure 4.14: Convergence for multi-species shear layer for standard and enhanced algorithms. I – min-CFL/max-VNN and MOC II boundary conditions with viscous preconditioning; II – max-CFL/max-VNN, MOC II, viscous preconditioning; III – min-CFL/max-VNN, MOC II, with inviscid preconditioning but no viscous preconditioning; IV – no preconditioning.

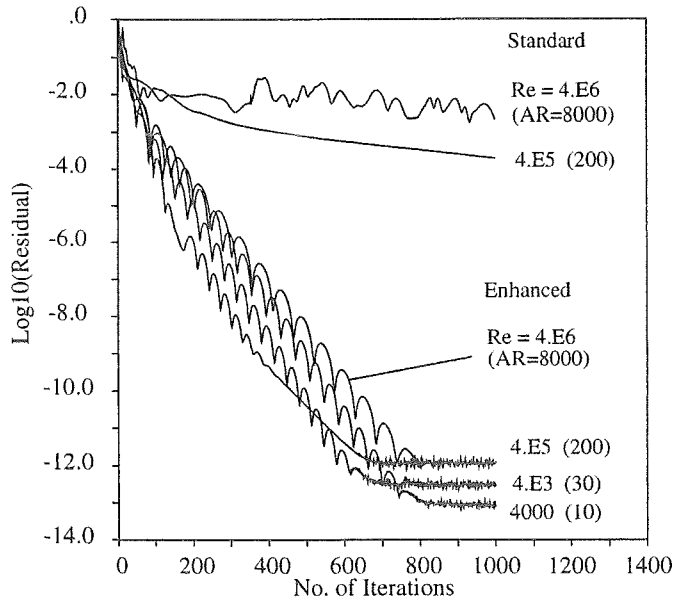


Figure 4.15: Convergence for flat plate boundary layer for standard and enhanced algorithms

grid stretching is required at high Reynolds numbers. This wall-stretching gives rise to high aspect ratio grids adjacent to the wall, while the grids away from the wall are more or less regular-sized. Slug flow was specified at the inflow boundary, with a constant back-pressure (1 atmosphere) at the outflow boundary, and a constant wall temperature of 500 K.

Convergence results using the enhanced algorithm are given in Fig. 4.15 for four different Reynolds numbers using grids with correspondingly different extents of wall grid stretching. The three lower Reynolds numbers ( $4 \times 10^4$ ,  $4 \times 10^4$  and  $4 \times 10^5$ ) are laminar computations and the corresponding maximum grid aspect ratios (located adjacent to the wall) are 10, 30 and 200, with corresponding stretching parameters of  $\beta=1.05$ , 1.01, and 1.001. The highest Reynolds number ( $4 \times 10^6$ ) is a turbulent computation and the maximum grid aspect ratio for this case is 8000 ( $y^+$  is less than one), with a stretching parameter of  $\beta=1.00002$ . In all cases, the flow Mach number is 0.1, and the grid size is  $61 \times 61$ . For the turbulent boundary layer computation, the algebraic Baldwin-Lomax turbulence model is employed.

The convergence in Fig. 4.15 using the enhanced algorithm is extremely good for all four Reynolds numbers. Despite the different aspect ratios of the grid cells for each of the cases, the convergence rates are almost identical reaching machine zero is about 800 iterations. For comparison, the convergence of one of the laminar cases ( $Re = 4 \times 10^5$ ) and of the turbulent case ( $Re = 4 \times 10^6$ ) using the standard algorithm (max-CFL/max-VNN) are also shown in Fig. 4.15. For the laminar case, the residuals drop just over an order of magnitude for every 1000 iterations requiring about 15,000 iterations to reach machine

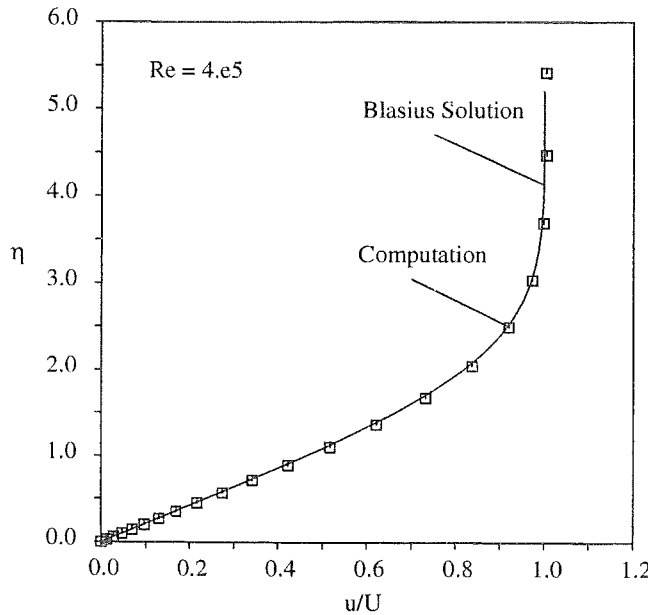


Figure 4.16: Laminar boundary layer solution

zero. The corresponding convergence speed-up of the enhanced algorithm is a factor of about 20. The turbulent computation in Fig. 4.15 reflects a convergence speed-up of about 100 times.

The velocity profiles obtained for the  $Re = 4 \times 10^5$  laminar calculation and the  $Re = 4 \times 10^6$  turbulent calculation are shown in Figs. 4.16 and 4.17. The laminar solution is compared with the Blasius profile, while the turbulent profile is plotted against the law of the wall and the log-law profiles. In both instances, there is good agreement between the numerical predictions and theory. The deviation of the computational results from the log-law for  $y^+ > 1000$  is characteristic of the outer-region. The extent of the deviation is related to the pressure gradient in the stream-wise direction. For stronger adverse pressure gradients, the deviation will increase.

### Converging-Diverging Nozzle

The final case is high Reynolds number turbulent flow through a converging-diverging nozzle with cooled walls. The grid geometry ( $141 \times 121$ ) and flow-field solution are shown in Fig. 4.18. The incoming gas is at a stagnation temperature of 3500 K while the wall is maintained at 700 K. Of particular interest for this case is the accurate prediction of the heat flux to the nozzle wall. Because of the extremely thin boundary layer in the throat region, very strong grid stretching is necessary to maintain a minimum  $y^+$  of about one along the wall. Accordingly, the corresponding maximum grid aspect ratio is  $2 \times 10^6$ .

The convergence results are shown in Fig. 4.19. With the enhanced algorithm, rapid convergence is obtained with machine zero being reached in less than 2000 iterations. With the standard algorithm, the convergence is fairly good for about four orders of

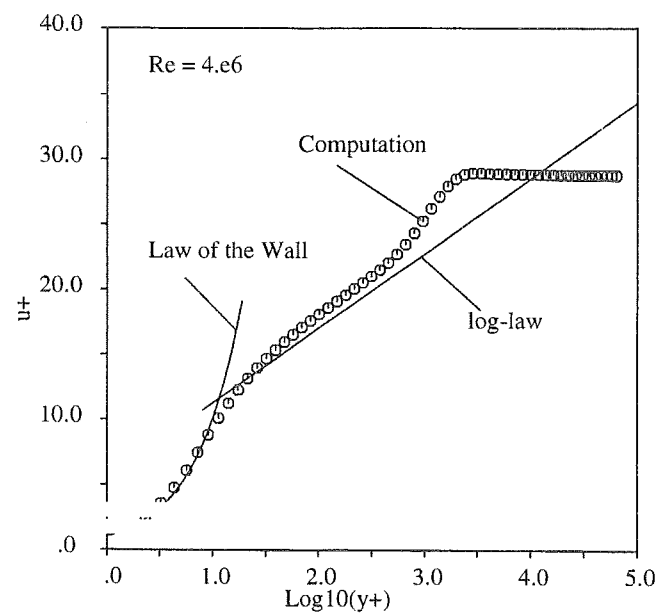


Figure 4.17: Turbulent boundary layer solution

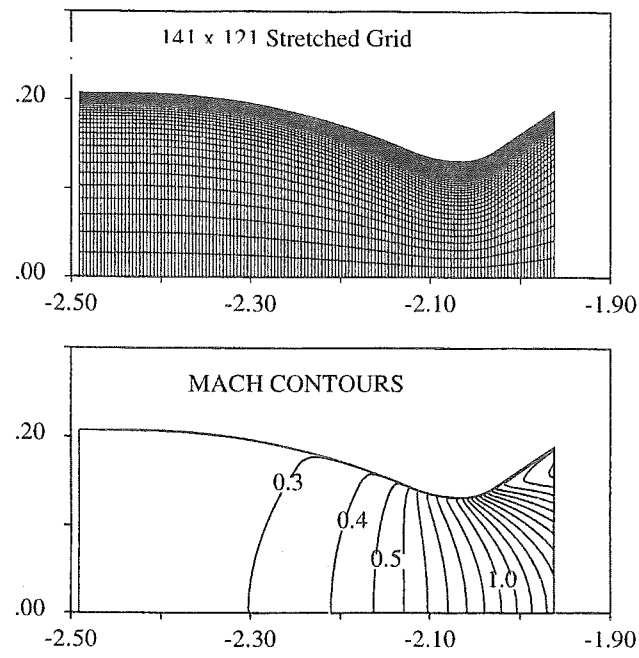


Figure 4.18: Stretched grid and Mach contours for the turbulent nozzle computation.

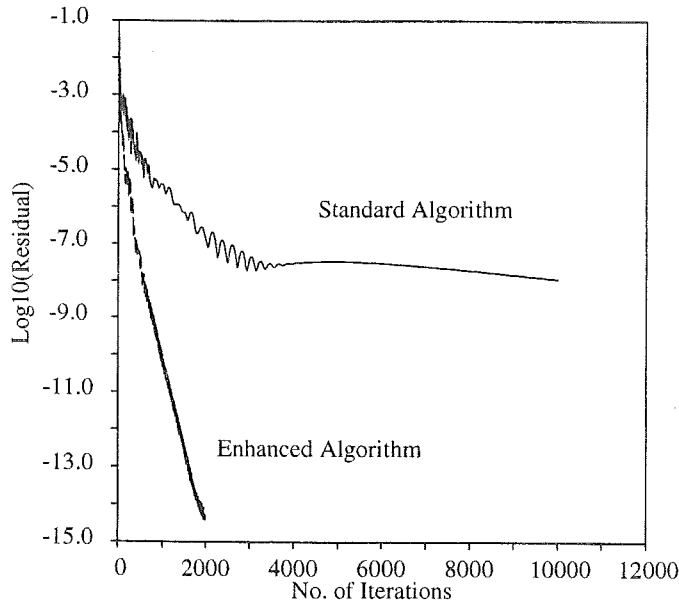


Figure 4.19: Convergence for nozzle computations with the standard algorithm (without aspect ratio control) and the enhanced algorithm (min-CFL/max-VNN).

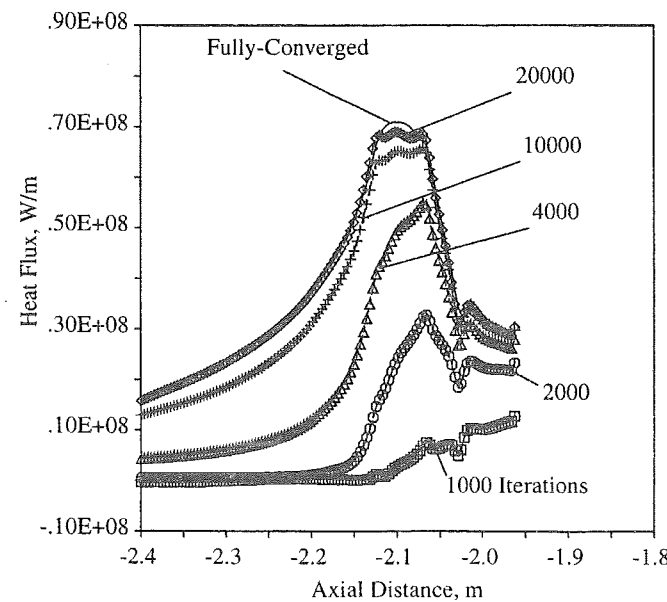
magnitude reduction in the residual, beyond which it becomes very poor. Examination of the residuals indicates that the initial portion corresponds to solution convergence in the central portion of the flow-field where the grids are more or less regular, while the latter portion is due to poor convergence in the high aspect ratio, near-wall region. This is also readily apparent by observing the temporal convergence of the wall heat flux shown in Fig. 4.20 for both the standard and enhanced algorithms.

The results in Fig. 4.20 for the standard algorithm without aspect ratio control indicate that after a three order-of-magnitude reduction in the residual (after 2000 iterations), the wall heat flux is far from converged. Converging the flow-field an additional order of magnitude (after 4000 iterations) causes the wall heat flux to change by almost a factor of two. It requires roughly 20,000 iterations (about six orders of magnitude convergence) for the heat flux to be approximately the same as the fully converged result. On the other hand, with the enhanced algorithm, the wall heat flux converges at the same rate as the overall flow-field and a three order-of-magnitude reduction in residual (less than 400 iterations) is sufficient to give wall heat flux to engineering accuracy. Thus, the convergence enhancement methods can significantly impact realistic flow computations.

### 4.3 Three-Dimensional Issues

Results presented in the previous sections demonstrated that for two-dimensional implicit schemes, the convergence degradation due to high aspect ratio cells can be removed. In fact, it was demonstrated that with proper time-step definition and preconditioning the

Standard Algorithm



Enhanced Algorithm

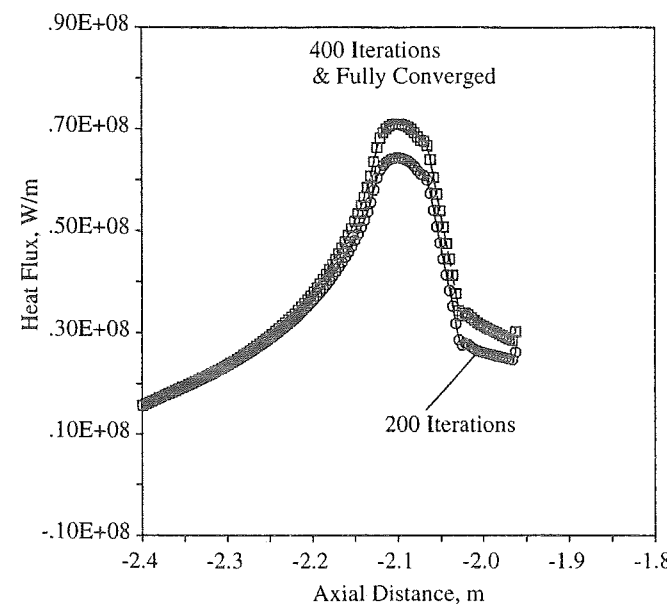


Figure 4.20: Temporal convergence of the heat flux along the nozzle wall for both the standard algorithm and the enhanced algorithm.

central-difference ADI and upwind ADI and DDLGS [50] algorithms provide uniform convergence at all grid aspect ratios (to  $10^6$ ). These methods, however, deal only with two-dimensional algorithms. In three dimensions, grid aspect ratio problems become much more complex. In this section, we make some remarks regarding three-dimensional issues.

As pointed out earlier, in three dimensions, we can categorize several kinds of high aspect ratio cells (see Fig. 4.1). Type 0 cells are defined as those where all three cell dimensions are commensurate and both  $\frac{\Delta x}{\Delta y}$  and  $\frac{\Delta x}{\Delta z}$  are of order one. Problems of Type I are defined as those where one cell dimension is small while the other two are large. Type II problems are those where two cell dimensions are small while the third is large. Type III cells are defined as those where all three cell dimensions are non-commensurate in size (*e.g.*  $\Delta x \ll \Delta y \ll \Delta z$ ). The presence of these three generic kinds of high aspect ratio cells is responsible for the additional complexity involved in mitigating AR effects in three-dimensional applications.

Besides these complexities encountered in 3-D high aspect ratio problems, the central-difference ADI algorithm suffers another short-coming that limits its performance in three dimensions. While the ADI algorithm is unconditionally stable in two dimensions, it becomes conditionally stable in three dimensions (and then only marginally so with maximum CFL's on the order of unity). This conditional stability becomes particularly limiting at high aspect ratios as will be shown.

The implicit, upwind algorithms (ADI, LU, LGS) have found considerable favor among CFD practitioners for three-dimensional problems; however, they, too, suffer in the presence of three-dimensional high aspect ratio cells. The conditional stability of these algorithms in two-dimensions (see Section 1.2) extends to three-dimensional problems and further exacerbates the difficulty in finding a solution to the 3-D high aspect ratio stiffness problem.

Recall that in standard CFD algorithms, the definition of the local time step is typically based on the smallest grid dimension. The CFL number associated with this direction is thus specified at an optimum value, while the CFL numbers corresponding to the longer cell dimensions are forced to be very small. As a result, flow-field disturbances propagate slowly and are damped ineffectively in the longer cell direction, which results in poor convergence. In 2-D, the factorized, implicit algorithms allow the local time-step size to be specified on the basis of the largest grid dimension. Thereby, the CFL numbers in both directions are maintained at optimum levels and the degradation in performance at high aspect ratios is avoided.

This attractive property does not readily extend to 3-D problems. As noted above, the three-factor ADI scheme is conditionally stable. It displays reasonable convergence properties for Type I cells, but not for Type II cells. In the latter case, the time step needs to be based on the two smaller dimensions resulting in a small CFL number in the longer cell dimension.

The three-factor ADI scheme may be written as:

$$\left[ \Gamma + \Delta t \frac{\partial}{\partial x} A \right] \Gamma^{-1} \left[ \Gamma + \Delta t \frac{\partial}{\partial y} B \right] \Gamma^{-1} \left[ \Gamma + \Delta t \frac{\partial}{\partial z} C \right] \Delta Q_p = -\Delta t \mathcal{R}^n \quad (4.4)$$

Examination of the approximate factorization errors shows that these are essentially combinations of products of the Jacobian matrices. Thus, we would anticipate the sizes of the errors to be controlled by the products of the various CFL numbers, *i.e.*,  $CFL_xCFL_y$ ,  $CFL_yCFL_z$ ,  $CFL_zCFL_x$  as well as  $CFL_xCFL_yCFL_z$ .

Examination of these error terms reveals the source of the difficulties with Type II cells. Type II cells involve two small sides and one long side, which means that two of the CFL numbers are much larger than the third. Therefore, to maintain the smallest CFL number of order one, the other two CFL numbers need to become much greater than unity. This means some of the AF error products will become much greater than any of the physical terms on the LHS operator. As a result, when the min-CFL time-step definition is used, the amplification factor approaches unity for any reasonable selection of the minimum CFL number. On the other hand, if the maximum CFL number is specified, the modes along the longitudinal direction languish on account of the low CFL number in that direction.

This brief consideration of three-dimensional issues thus indicates that the high aspect ratio problems are not handled very effectively by any of the implicit algorithms. Although further research in this area may offer some hope of an improved factorization or relaxation algorithm, it appears that multigrid techniques being developed by several researchers [56, 53, 54, 55, 43] may offer the best potential for solving this problem effectively.

# Chapter 5

## Preconditioning for the Unsteady Equations

Engineering problems frequently involve the resolution of unsteady fluid dynamic processes. These unsteady processes are governed by a wide variety of time-scales ranging from high-frequency processes that are characterized by propagation of acoustic waves and low frequency problems that are characterized by eddies and vortices that propagate at particle velocities. Such a wide range of time scales poses a challenge to even the most advanced time-accurate CFD algorithms. Algorithms that are effective for transonic and supersonic flows are also effective for high-frequency acoustics problems, but are inefficient for low speed and incompressible flows. On the other hand, algorithms that are effective for low speed and incompressible flows are usually incapable of handling acoustics and compressibility effects. Furthermore, none of the methods are particularly well-suited for low-speed compressible flowfields such as diffusion flames. With the growing demand for detailed flowfield simulations and, particularly, with recent advances in Large Eddy Simulations (LES) and Direct Numerical Simulations (DNS), there is a pressing need for a unified approach for solving unsteady flow problems.

The dual-time framework is preferred approach for the time-accurate solution of the Euler and Navier-Stokes equations, and is a popular choice for incompressible and low speed compressible flows. These methods utilize a second set of artificial time-derivatives for marching the physical unsteady equations in pseudo-time in order to obtain a converged solution at each physical time-step. The dual-time iterations serve as an iterative device to eliminate linearization and approximate factorization errors from the time-accurate equations. Since the main function of the pseudo-time derivatives are to drive out the transient errors, they can be preconditioned to optimize the rate of convergence. In this chapter, we analyze the performance of preconditioned dual-time schemes using perturbation analyses, stability theory and computational test cases. Specifically, we examine the limiting behavior of the unsteady equations under low speed and viscous-dominated conditions and devise appropriate preconditioning procedures to enhance performance.

## 5.1 Algorithms for Unsteady Computations

We begin by considering standard CFD approaches for computing unsteady flows. Our interest is primarily on implicit iterative approaches such as the approximate-Newton method and the dual-time stepping method. We employ von Neumann stability analyses to probe the performance behavior of the basic algorithms for different kinds of flow situations. The stability results reveal the basic strengths and weaknesses of these methods.

### 5.1.1 Unsteady Governing Equations

The unsteady Navier-Stokes equations in two dimensional cartesian coordinates are given in their standard vector form,

$$\frac{\partial Q}{\partial t} + \frac{\partial E}{\partial x} + \frac{\partial F}{\partial y} = \mathcal{L}(Q_p) \quad (5.1)$$

where the inviscid and viscous flux vectors are defined in Appendix A.1.2. Although our interest is on the Navier-Stokes equations, we focus primarily on the Euler equations subset to elucidate the concepts. Where it is appropriate, we discuss any additional issues that are unique to the diffusion terms.

For the discretized version of the equations, the physical time scales associated with the wave speeds of the Euler equation system are given by the different CFL numbers. For example in the  $x$  direction, we have  $CFL_u = u\Delta t/\Delta x$  and  $CFL_{u\pm c} = (u \pm c)\Delta t/\Delta x$ . These CFL numbers are of fundamental importance for the numerical solution of unsteady Euler problems. In particular, the physical time-step size should be selected based on whether acoustic processes or particle waves need to be resolved. For acoustics problems, it is generally necessary to maintain  $CFL_{u+c}$  of order unity (or less) to ensure temporal accuracy. Likewise, for unsteady flows governed by the particle wave speeds,  $CFL_u$  should be of order unity (or less). In practical situations, however, the time scales (or CFL numbers) are likely to vary significantly within the solution domain because of local grid-stretching. Further, in some instances, the viscous time-steps (or the von Neumann numbers, VNN) may also play significant role in the evolution of unsteady processes. In the following sections, we examine the role that the physical time scales play in the numerical solution of unsteady problems.

Both explicit and implicit algorithms are commonly used for unsteady computations. When applied as non-iterative, time-marching methods, these algorithms frequently lose temporal accuracy unless extremely small physical time-steps are used. This is particularly true for complex flowfields involving strong non-linear behavior such as shock waves and combustion problems. Furthermore, stability criteria impose further limitations on physical time-step size especially for explicit algorithms. Similar time-step restrictions also exist for implicit algorithms in multi-dimensions because of errors associated with the approximate-inversion methods that are typically used. Particularly, in the presence of strong local grid-stretching or in low Mach number flows, such time-step restrictions may severely impair the usefulness of the algorithm. For these reasons, unsteady algorithms usually adopt some sort of an iterative procedure at each physical time-level, which

ensures temporal accuracy and, in the case of implicit schemes, also serves to eliminate linearization and approximate-factorization errors. Importantly, these methods potentially allow the selection of the physical time-step size according to the governing physical processes, rather than by considerations of numerical stability.

Two iterative approaches are in common use—namely, the approximate-Newton iterative procedure [57] or the dual-time-stepping approach [59, 58, 62]. Both methods employ “inner” or “sub” iterations at each physical time-level and are, in fact, closely related. The dual-time-stepping method is the more general approach and the approximate Newton method may be shown to be a subset of it. The dual-time method introduces a pseudo-time derivative (in addition to the physical time derivative), which acts as an agent to drive out errors in the physical transient and ensure convergence in the inner iterations. The advantage of the method lies in the fact that the pseudo-time derivatives may be chosen so as to optimize the convergence of the inner iterations. The selection of the pseudo-time derivatives may be achieved through the use of an appropriate preconditioning matrix that is tuned to the unsteady dual-time formulation.

We first discuss the stability properties of the approximate-Newton method and then consider the more general dual-time procedure.

### 5.1.2 Approximate-Newton Method

In the approximate-Newton method, Eqn. 5.1 is solved iteratively at each physical time-level. The inner iterations at each time-level eliminate the linearization and approximate-factorization errors and thereby ensure temporal accuracy. Typically, the spatial derivatives are treated using either second-order central differences or third-order upwind-biased differences, while the temporal derivatives are treated using second-order accurate backward differences in time. The two-dimensional implicit operator resulting from the Euler implicit linearization of the fluxes is inverted approximately using one of several methods, such as ADI, symmetric point-Gauss Seidel or line-Gauss Seidel methods as discussed in Section 1.2.

For simplicity, we present only the ADI scheme, which we present in the following generic form for both central and upwind schemes,

$$\left[ \frac{3}{2}I + \Delta t \frac{\partial A}{\partial x} \right] \frac{2}{3} \left[ \frac{3}{2}I + \Delta t \frac{\partial B}{\partial y} \right] \Delta Q = -\Delta t \mathcal{R}^k \quad (5.2)$$

Here, term  $\mathcal{R}^k$  represents the residual error of the complete unsteady equation at the  $k$  inner iteration level,

$$\mathcal{R} = \frac{3Q^k - 4Q^n + Q^{n-1}}{2\Delta t} + \frac{\partial E^k}{\partial x} + \frac{\partial F^k}{\partial y} + \mathcal{L}(Q_p^k)$$

$\Delta Q = Q^{k+1} - Q^k$ . Equation 5.2 is the approximately factored expression that describes the inner iteration for the solution at time-level  $n + 1$ . At the first inner iteration,  $Q^0$  is set equal to  $Q^n$ , the solution at time level  $n$ . Upon convergence,  $\Delta Q \rightarrow 0$  and the

unsteady equations are clearly satisfied. The solution at the time level  $n + 1$  is then given by  $Q^{n+1} = Q^k$ . If only one inner iteration is performed at each time level, the scheme reduces to the standard non-iterative time-marching method. Note the similarity of the approximate-Newton method with the multi-sweep relaxation methods described in Section 1.2.4.

The convergence characteristics of the inner iterations are obviously dependent on the size of the physical time-step. In particular, the approximate-factorization error in Eqn. 5.2 is given by  $[\frac{\Delta t^2}{\Delta x \Delta y} A B]$  and its magnitude is related to magnitudes of the physical CFL numbers (and VNN numbers for viscous flows). When the CFL numbers become much larger than unity, the factorization errors may dominate and preclude convergence. For acoustic problems and transonic and supersonic Mach numbers, the maximum physical CFL (i.e.,  $CFL_{u+c}$ ) is typically around unity and there is no difficulty with convergence. In fact, in the limit of small CFL's, Eqn. 5.2 becomes strongly sink-dominated (corresponding to the time-derivative term), which is extremely favorable to convergence. Experience with such problems shows that convergence to machine zero is typically attained in fewer than ten iterations. On the other hand, for low-speed problems, when it is desired to track particle waves,  $CFL_u$  is around unity while  $CFL_{u+c}$  can be several orders of magnitude larger. In such cases, we may anticipate convergence problems, as is indeed observed in practice.

Von Neumann stability analysis of the approximate-Newton method in Eqn. 5.2 is an effective method of analyzing the convergence behavior of the inner iterations. Figure 5.1 shows the maximum amplification factor as a function of wave-number space for  $M = 0.5$  and  $CFL_{u+c} = 1$ . All the other CFL numbers are therefore less than unity. The extremely small values of the amplification factor suggests excellent damping properties, an indication that Eqn. 5.2 is dominated by the sink-like temporal derivative at this condition.

Figure 5.2 shows the stability results for a low Mach number situation ( $M = 0.001$ ) for two values of physical CFL— $CFL_{u+c} = 1$  and  $CFL_u = 1$ . The former choice of time-step is appropriate for resolving acoustic scales and since the corresponding  $CFL_u = 1 \times 10^{-3}$ , all the AF errors are small. Again, excellent damping properties are observed. This choice of time-step is, however, not suitable for tracking particle waves since tens of thousands of ‘outer’ (i.e., physical) time steps are necessary to advance the wavefront through the flowfield.

The second set of results for  $M = 0.001$  and  $CFL_u = 1$  represent an appropriate choice of physical time-step for resolving particle wave speeds. The amplification factors are, however, observed to be near unity over the entire wavenumber domain, suggesting very slow convergence rates in the inner iterations. This extremely stiff stability result is due to the large values of the acoustic-CFL number ( $CFL_{u+c} = 1000$ ), which means that the approximate factorization errors dominate over the physical terms in Eqn. 5.2.

Stability results (not shown) for the approximate-Newton method using upwind-based differences with the ADI, DDLU or DDLGS schemes all show similar trends. In these schemes, the stiffness in the amplification factors (for low Mach number problems) is generally limited to the low wavenumber regions, while the inherent dissipation of these

$M=0.5, CFL_{u+c}=1$

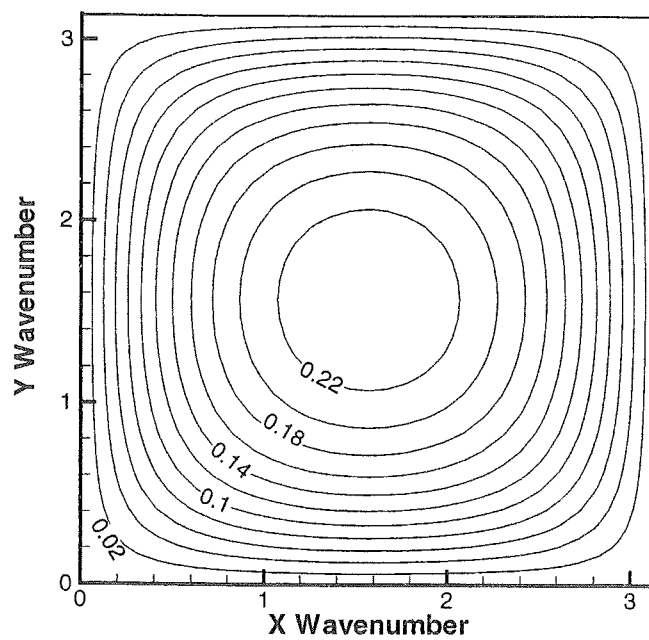


Figure 5.1: Stability Results. Approximate-Newton Scheme. Central-Difference ADI.  
 $M=0.5, CFL_{u+c} = 1$ .

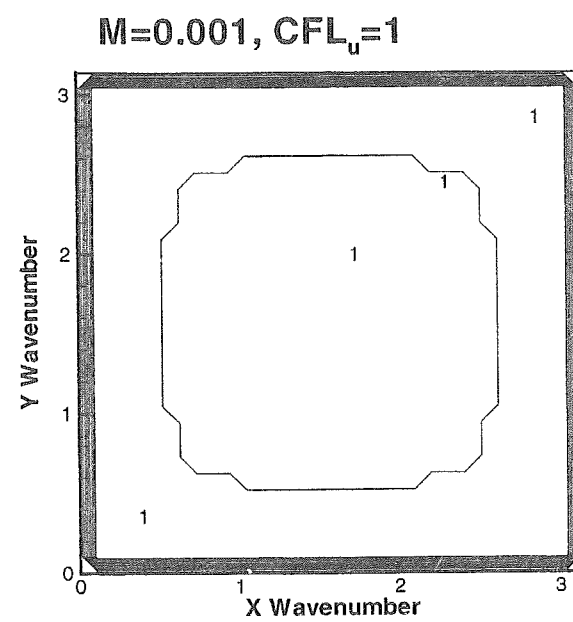
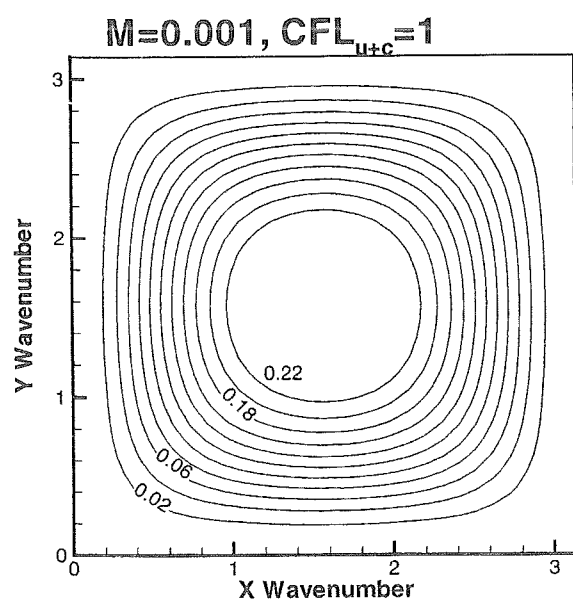


Figure 5.2: Stability Results. Approximate-Newton Scheme. Central-Difference ADI.  
 $M=0.001$ ,  $CFL_{u+c} = 1$  and  $CFL_u = 1$ .

schemes provides adequate damping of the mid and high wave numbers (similar to the steady-state stability results in Section 1.2.5). Experience indicates that convergence behavior is usually controlled by the stiff low wavenumbers. Thus, for low-speed problems such as unsteady mixing layers or diffusion flames, where the time scales are characterized by the particle velocity, one is faced with either taking a large number of outer steps with rapid inner-iteration convergence or taking few outer steps with slow inner-iteration convergence. In most instances, neither solution is practical. In the following section, we consider the dual-time stepping approach and evaluate its convergence characteristics.

### 5.1.3 Dual-Time Stepping Scheme

A second and related approach for the solution of unsteady flowfields is the dual-time technique [59, 58], wherein an artificial time-derivative is introduced in addition to the physical time-derivative in Eqn. 5.2

$$\Gamma_p \frac{\partial Q_p}{\partial \tau} + \frac{\partial Q}{\partial t} + \frac{\partial E}{\partial x} + \frac{\partial F}{\partial y} = 0 \quad (5.3)$$

where  $\Delta\tau$  is the pseudo-time step and  $\Gamma_p$  is the preconditioning matrix pre-multiplying the pseudo-time derivative. Note that we continue to express the pseudo-time derivative in terms of the primitive variables set,  $Q_p = (p, u, v, T)^T$ . This new time-derivative is then responsible for the inner or sub-iterations at each physical time level. By judicious selection of the preconditioning for the second time derivative, convergence of the inner iterations may be optimized under different conditions. Note the similarity of the method with the linearized preconditioning scheme discussed in Section 2.4.3.

For now, we will take the definition of the preconditioning matrix to be the same as that developed with regard to the steady state system (see Appendix B.1). Later in this chapter, we will devise the proper definition of the preconditioning terms, in particular, that of the preconditioning parameter,  $\rho'_p$ .

The dual time-stepping scheme with ADI approximate factorization may be expressed as,

$$\left[ S + \Delta\tau \frac{\partial A}{\partial x} \right] S^{-1} \left[ S + \Delta\tau \frac{\partial B}{\partial y} \right] \Delta Q_p = -\Delta\tau \mathcal{R}^k \quad (5.4)$$

Note that Eqn. 5.4 has been derived by linearizing the governing equations in terms of the new dependent vector  $Q_p$  and the Jacobians  $A$  and  $B$  should be interpreted accordingly. Also,  $S$  is given by:

$$S = \Gamma_p + \frac{\Delta\tau}{\Delta t} \frac{3}{2} \Gamma_e$$

and  $\Gamma_e$  represents the Jacobian  $\frac{\partial Q}{\partial Q_p}$ . Again, upon convergence of the inner iterations,  $\Delta Q_p \rightarrow 0$  and the residual  $\mathcal{R}^k$  of the full unsteady equation is satisfied.

It is easy to see that when  $\Gamma_p = \Gamma_e$  and  $\Delta\tau \rightarrow \infty$ , the dual-time scheme in Eqn. 5.4 becomes identical to the approximate-Newton scheme in Eqn. 5.2. Indeed, for unsteady transonic flow problems and acoustic problems, these are indeed optimum choices for these

parameters. However, for unsteady low-speed problems involving slower characteristic time scales, we have seen that these choices are ineffective. Under such conditions, it is desirable to specify  $\Gamma_p$  and  $\Delta\tau$  in a manner that guarantees optimum convergence. It is this inherent flexibility of the dual-time approach that makes it an attractive basis for the construction of improved unsteady algorithms.

One possible definition of  $\Gamma_p$ , which has been used by previous researchers [26, 61], is to use steady state choice. We consider stability results using the steady-state preconditioning system in Fig. 5.3 for  $M = 0.001$  and the same physical CFL's as in Fig. 5.2. The pseudo-CFL ( $CFL_\tau = \lambda_+^p \Delta\tau / \Delta x$ ,  $\lambda_+^p$  being the maximum eigenvalue of the preconditioned system) in both cases is taken to be 3, the optimum value for the ADI scheme. The results for  $CFL_{u+c} = 1$  and  $CFL_u = 1 \times 10^{-3}$  is seen to be extremely stiff. For this case, the physical CFL numbers are all small and Eqn. 5.4 is sink-dominated (i.e., dominated by the physical time-derivative). Preconditioning the pseudo-time derivative according to the characteristics of the spatial derivatives is then inappropriate and leads to the poor stability map. In other words, the introduction of the pseudo-sound speed,  $(\rho'_p/d)$  negates the favorable damping characteristics of the sink term. As noted earlier, the approximate-Newton method performs well for this method and this may be recovered by setting  $\Gamma_p = \Gamma_e$  and  $CFL_\tau$  to infinity. This choice tunes the pseudo-time derivative to the sink term and maximizes the damping of errors in the physical transient.

On the other hand, the steady preconditioning system performs reasonably well for  $CFL_u = 1$  and  $CFL_{u+c} = 1000$ . Under these conditions, the spatial derivatives are more dominant, a consequence of the large acoustic CFL's. Thus, the selection of  $\Gamma_s$  is more appropriate. Note, however, that the low wave-number regions still show some residual stiffness (i.e., amplification factors are close to one). This suggests that convergence of the inner iterations may still be quite slow. If still larger physical time-steps are used, the stability improves further until it eventually resembles the steady-state stability diagram. The convergence of the inner iterations will then resemble steady-state convergence. In general, this limit is not of much importance for unsteady calculations.

From these results for low Mach numbers, it appears that different choices of the preconditioning matrix are required for the two limits of small and large physical time-steps. Furthermore, neither choice does particularly well for intermediate choices of time-step size (not shown). In problems involving strong grid-stretching, a wide range of physical CFL's are encountered. Thus, the proper selection of the preconditioning matrix is essential for the optimum solution of realistic flowfields. In the next section, we will employ perturbation expansions to further probe the limiting behavior of the unsteady equations.

## 5.2 Perturbation Analysis of the Unsteady Equations

As in the case of the Euler and Navier-Stokes equations, we perform perturbation expansions of the governing equations and examine the limiting conditions. We then devise appropriate preconditioning procedures so that the equations remain well-conditioned

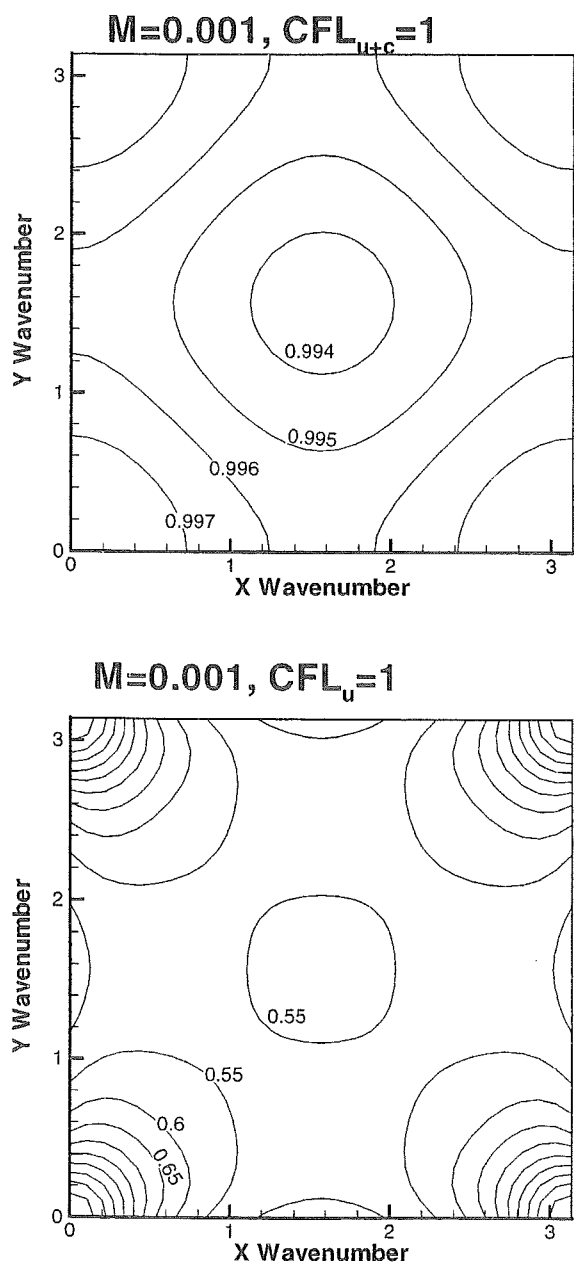


Figure 5.3: Stability Results for Dual Time Scheme, Central-Difference ADI, Steady Preconditioning.  $M=0.001$ ,  $CFL_\tau = 3$ ,  $CFL_{u+c} = 1$  and  $CFL_u = 1$ .

under all limits.

We begin with the one-dimensional Navier-Stokes equations given in Appendix A.1.1. In addition to the physical time-derivatives, we add a set of pseudo-time derivatives, which will allow us to investigate the dual-time iterative algorithm discussed earlier. Following the procedure in Section 2.1.1, we re-write the equations in terms of the primitive variable set  $Q_p$ , transform to non-conservative form and non-dimensionalize the variables. The resulting set of non-dimensionalized equations in non-conservative form are given as,

$$\begin{aligned} \left(\frac{\chi_r L}{\tau_r u_r}\right) \left( \tilde{\rho}_p \frac{\partial p}{\partial \tau} + \tilde{\rho}_T \frac{\partial T}{\partial \tau} \right) + \rho \frac{\partial u}{\partial t} + \chi_r \frac{\partial \rho u}{\partial x} &= 0 \\ \left(\frac{\chi_r L}{\tau_r u_r}\right) \rho \frac{\partial u}{\partial \tau} + \rho \frac{\partial u}{\partial t} \chi_r \rho u \frac{\partial u}{\partial x} + \left(\frac{\chi_r p_r}{\rho_r u_r^2}\right) \frac{\partial p}{\partial x} &= \frac{\chi_r}{Re_r} \frac{\partial}{\partial x} \left( \mu \frac{\partial u}{\partial x} \right) \quad (5.5) \\ \left(\frac{\chi_r L}{\tau_r u_r}\right) \left[ -\left(\frac{p_r}{\rho_r h_r} - \rho \tilde{h}_p\right) \frac{\partial p}{\partial \tau} + \rho \tilde{h}_T \frac{\partial T}{\partial \tau} \right] + \rho \frac{\partial h}{\partial t} - \left(\frac{p_r}{\rho_r h_r}\right) \frac{\partial p}{\partial t} + \chi_r \rho u \frac{\partial h}{\partial x} - \left(\frac{\chi_r p_r}{\rho_r h_r}\right) u \frac{\partial p}{\partial x} \\ &= \frac{\chi_r}{Re_r Pr_r} \frac{\partial}{\partial x} \left( \kappa \frac{\partial T}{\partial x} \right) - \frac{\chi_r u_r^2}{Re_r h_r} \mu \left( \frac{\partial u}{\partial x} \right)^2 \end{aligned}$$

where we have now written the terms such that the physical time-derivative terms are unity. Note that we have introduced a new reference time,  $t_r$ , for the physical time term. As a result, we have also introduced a new dimensionless parameter,  $\chi_r = t_r/(L/u_r)$ , which is the ratio of the physical time scale to the convective time-scale. Note also that the ratio,  $\chi_r/Re_r$  likewise represents a ratio of the physical time scale to the diffusion time scale.

As a limiting condition, we consider the regime in which the unsteady effects are important and dominate the convective and diffusive effects. Unsteady effects are characterized by the size of the time-scale ratio,  $\chi_r$ . For acoustic wave problems, the physical time scales are characterized by the physical acoustic speeds and  $\chi_r$  approaches  $M_r$ . On the other hand, for vortex propagation problems, the physical time scales are defined by the particle wave speed and the ratio  $\chi_r$  is close to unity. Finally, for unsteady viscous-dominated problems, the characteristic physical time scale would be the diffusion time-scale, then  $\chi_r \rightarrow Re_r$ . Thus, we are specifically interested in cases where the physical time ratio,  $\chi_r \leq 1$ .

We again start by expanding the pressure in a perturbation series,

$$p = p_0 + \epsilon_u p_1 + \dots \quad (5.6)$$

where we use yet another small parameter,  $\epsilon_u$ . The definition of  $\epsilon_u$  will be determined by balancing the pressure gradient with the physical time derivative term in the momentum equation.

Inserting the pressure expansion into the momentum equation, we get,

$$\left(\frac{\chi_r L}{\tau_r u_r}\right) \rho \frac{\partial u}{\partial \tau} + \rho \frac{\partial u}{\partial t} \chi_r \rho u \frac{\partial u}{\partial x} + \left(\frac{\chi_r p_r}{\rho_r u_r^2}\right) \epsilon_u \frac{\partial p_1}{\partial x} = \frac{\chi_r}{Re_r} \frac{\partial}{\partial x} \left( \mu \frac{\partial u}{\partial x} \right) \quad (5.7)$$

where we again conclude that the zeroth order pressure must be constant.

The requirement that the pressure gradient term balance the unsteady time derivative specifies the perturbation parameter,  $\epsilon_u$ ,

$$\epsilon_u = \frac{\rho_r u_r^2}{p_r} \frac{1}{\chi_r} \quad (5.8)$$

with the implication that  $\epsilon_u$  is a small parameter and with the condition that  $\chi_r \leq 1$ . For ideal gases, we get  $\epsilon_u = \gamma M_r^2 / \chi_r$ . Thus, the limiting condition of interest is obtained when  $M_r^2 \ll \chi_r$  and  $\chi_r \leq 1$ . Note that from our earlier observations on the magnitude of  $\chi_r$ , we anticipate that this condition is attained for most low-speed unsteady problems.

As before, we also require the pseudo-time derivative to be order unity as well,

$$\tau_r = \frac{L}{u_r} \chi_r = t_r \quad (5.9)$$

which essentially means that the pseudo-time scale is the same as the physical time scale.

We then turn to the continuity equation to obtain an update the first-order pressure term that appears in the pressure gradient in the momentum equation. This involves defining an artificial property function,  $\tilde{\rho}'_p$  so that the pseudo-time derivative of the first-order pressure becomes of order one, i.e., the same order as the physical time-derivative term. We then get,

$$\tilde{\rho}'_p = k_u \frac{\chi_r}{\epsilon_u} = k_u \frac{\chi_r^2 p_r}{\rho_r u_r^2} \quad (5.10)$$

where  $k_u$  is a constant of order one. In dimensional form, this expression is  $\rho'_p = k_u \chi_r^2 / u_r^2$ . For ideal gases, we have  $\rho'_p = k_u \chi_r^2 \rho_p / \gamma M_r^2$ .

The preconditioning definition in Eqn. 5.10 deserves further comment. We noted earlier that for acoustic wave problems,  $\chi_r \rightarrow M_r$ . This essentially means that  $\rho'_p \rightarrow 1/c^2$ , which is essentially  $\rho_p$ . The analysis thus stipulates that for acoustic problems, the pseudo time-derivative must not be preconditioned, or the original time-derivatives must be used. This is precisely the same conclusion that we arrived at from stability analysis in Section 5.1.3. On the other hand, for vortex propagation problems,  $\chi_r \rightarrow 1$ . In that case, the above preconditioning definition prescribes the use of the low Mach number inviscid preconditioning choice (see Eqn. 2.14), which is again in agreement with the stability results in Section 5.1.3. Finally, for viscous-dominated unsteady flows, we get  $\chi_r \rightarrow Re_r$  which gives us the viscous preconditioning choice from Eqn. 3.15.

Thus, the unsteady preconditioning provides a means of shifting the definition of the preconditioning from that corresponding to the original system to those corresponding to the inviscid and viscous preconditioning choices, depending upon the kind of problem being solved. Further, we make the observation that since  $\chi_r = u_r t_r / L$ , its definition essentially corresponds to a physical *CFL* number based upon the physical time-step and the characteristic particle velocity and a representative length dimension for the problem.

The final step of deriving the complete form of the preconditioning system from the above perturbation equations is the same as that described in previous chapters. The form of the preconditioning matrix is identical to that given in Eqn. 2.23. The definition of the matrix and the  $\rho'_p$  parameter are discussed in the following section.

### 5.3 Implementation of Unsteady Preconditioning

The preconditioned unsteady Navier-Stokes equations in two dimensions are given as,

$$\Gamma_p \frac{\partial Q_p}{\partial \tau} + \frac{\partial Q}{\partial t} + \frac{\partial E}{\partial x} + \frac{\partial F}{\partial y} = \mathcal{L}(Q_p) \quad (5.11)$$

where the preconditioning matrix,  $\Gamma_p$  is defined in Eqn. 2.24 and the flux vectors are given in Appendix A.1.2. The definition of the preconditioning parameter  $\rho'_p$  is now modified to include the unsteady terms and is discussed below.

We define the preconditioning parameter,  $\rho'_p$ , by specifying the artificial speed of sound,

$$\frac{\rho h_T}{d'} = V_p^2 \quad (5.12)$$

where the preconditioned velocity scale is given as,

$$V_p = \text{Min}[ \text{Max}(V_{inv}, V_{pgr}, V_{vis}, V_{uns}), c ]$$

where  $V_{inv}$ ,  $V_{vis}$  and  $V_{pgr}$  have their usual definitions. The new unsteady preconditioning velocity scale is given as,

$$V_{uns} = \text{Max}\left[\frac{l_x}{\pi \Delta t}, \frac{l_y}{\pi \Delta t}\right]$$

where  $l_x$  and  $l_y$  are characteristic dimensions in the  $x$  and  $y$  directions respectively. We typically select them to be the physical dimensions of the geometrical configuration being modeled. Note that this definition is closely patterned after the unsteady preconditioning choice suggested by the perturbation analysis (Eqn. 5.10). The derivation of the precise form follows from the analysis given in the following section [62].

### 5.4 Stability Analysis and Convergence Studies

#### 5.4.1 One-Dimensional Stability Analysis

Von Neumann stability analysis of the one-dimensional version of Eqn. 5.3 is useful in enhancing understanding of the dual-time scheme because the amplification factors of the scheme may be derived analytically. The amplification matrix may be written as:

$$G = \left[ \Gamma_p + \Gamma_e \frac{\Delta \tau}{\Delta t} + \frac{A \Delta \tau}{\Delta x} (i S_x) \right]^{-1} \Gamma_p \quad (5.13)$$

where  $S_x = \text{Sin}(n \pi \Delta x / l)$ . It is more convenient to write out the eigenvalues of  $G^{-1}$  rather than those of G. The corresponding amplification factors are then given by the reciprocals of these eigenvalues:

$$\lambda_1 = 1 + \frac{\Delta \tau}{\Delta t} + \frac{u \Delta \tau}{\Delta x} i S_x \quad (5.14)$$

$$\lambda_{2,3} = 1 + \frac{1}{2} \left[ \left( \frac{\Delta\tau}{\Delta t} + \frac{u\Delta\tau}{\Delta x} iS_x \right) (1 + M_p^2) \pm \sqrt{\left( \frac{\Delta\tau}{\Delta t} + \frac{u\Delta\tau}{\Delta x} iS_x \right)^2 (1 - M_p^2)^2 - 4M_p^2 \gamma RT \left( \frac{\Delta\tau S_x}{\Delta x} \right)^2} \right]$$

where we have taken  $\rho'_p = 1/\epsilon_p c^2$  and  $\rho'_T = 0$ , which gives  $\epsilon_p = M_p^2$ . The stability condition requires the magnitudes of these complex eigenvalues be greater than unity and the larger the eigenvalues, the better the damping.

We first consider the eigenvalues in Eqn. 5.14 as we approach the limits of small and large time-step sizes. When all the physical CFL numbers are small (as they are for transonic and supersonic flows and problems involving acoustic waves), the eigenvalues become:

$$\lambda_1 = 1 + \frac{\Delta\tau}{\Delta t} \quad \text{and} \quad \lambda_{2,3} = 1 + \frac{1}{2} \left[ \frac{\Delta\tau}{\Delta t} (1 + M_p^2) \pm \frac{\Delta\tau}{\Delta t} (1 - M_p^2) \right]$$

Here, the choice of  $M_p = 1$  (no-preconditioning) renders the three eigenvalues equal. Note that all three eigenvalues show damping that is proportional to the ratio of the pseudo to artificial time-step sizes. When  $\Delta\tau$  is taken to be infinity and since  $\Delta t$  is small, extremely rapid convergence will result. As noted earlier, this choice corresponds to the approximate-Newton method, which works well for such problems. On the other hand, when  $M_p = M$  (steady preconditioning), one of the eigenvalues approaches unity as Mach number becomes low. This will correspond to poor convergence rates in the inner iterations. These conclusions are in agreement with the stability findings in Figs. 5.2 and 5.3.

Alternately, in the limit of large physical CFL numbers (the limit of steady-state), the eigenvalues become:

$$\lambda_1 = 1 + \frac{u\Delta\tau}{\Delta x} iS_x$$

$$\lambda_{2,3} = 1 + \frac{1}{2} \left[ \frac{u\Delta\tau}{\Delta x} iS_x (1 + M_p^2) \pm \sqrt{\left( \frac{u\Delta\tau}{\Delta x} iS_x \right)^2 (1 - M_p^2)^2 - 4M_p^2 \gamma RT \left( \frac{\Delta\tau S_x}{\Delta x} \right)^2} \right]$$

It is clear that the magnitudes of these eigenvalues depend on the pseudo-CFL numbers, which is to be anticipated in the steady-state limit. At low Mach numbers, the acoustic-CFL number is much greater than the particle-CFL number. The second expression then reduces to  $\lambda_{2,3} = \pm \sqrt{M_p^2 \gamma RT} \frac{\Delta\tau}{\Delta x} iS_x$ . Thus,  $\lambda_1$  is governed by the particle-CFL number and  $\lambda_{2,3}$  are controlled by the acoustic-CFL number. When  $M_p = 1$  (no preconditioning) the disparity between the two sets of amplification factors causes the different parts of the equation to converge at vastly different rates. With approximate-inversion methods such as ADI, LU or LGS, this results in poor convergence rates. However, when  $\epsilon = M^2$  (steady preconditioning), the three eigenvalues are of the same order of magnitude and the difficulty is resolved.

In between the above two limits, examination of the eigenvalues in Eqn. 5.14 suggests the following definition of  $M_p^2$  so as to maintain reliable damping properties,

$$M_p^2 = \left( \frac{\Delta x}{\Delta t S_x} \right)^2 \frac{1}{c^2}$$

The above expression depends on the wavenumber through the term  $S_x$ . Since in most problems, it is the low wavenumbers that are typically the hardest to damp out, we tune the  $\epsilon_p$  definition so that it is optimum for the smallest wavenumber in the domain, i.e.,  $S_x = \pi\Delta x/l$  (i.e.,  $n = 1$ ). We then get,

$$M_p^2 = \left(\frac{l_x}{\pi\Delta t}\right)^2 \frac{1}{c^2}$$

which is the expression that was used in Eqn. 5.12.

#### 5.4.2 Two-Dimensional Stability Analysis

In order to confirm the stability/convergence properties of the unsteady preconditioning choice for two-dimensional unsteady computations, we consider the von Neumann stability results. Figure 5.4 shows these results for the central-difference ADI scheme for  $M = 0.001$  and two values of physical CFL— $CFL_{u+c} = 1$  (acoustic propagation) and  $CFL_u = 1$  (vortex propagation). In both cases, we take the pseudo-CFL ( $CFL_\tau$ ) to be three. In contrast to the schemes considered previously, the present scheme reveals good damping under both situations even though they correspond to widely different time scales. In the  $CFL_u = 1$  situation, the approximate factorization error is evident over the mid wavenumbers causing the amplification factor to be around 0.9. However, as mentioned earlier, the convergence rate is primarily governed by the low wavenumbers, where this scheme shows better damping characteristics.

Similar stability results for the upwind-biased DDLGS scheme is shown in Fig. 5.5. Here, the RHS fluxes are treated using third-order upwind-biased differences, while the LHS fluxes are treated using first-order upwind differences. In the context of the dual-time scheme, it is important that the construction of the numerical fluxes be based on the preconditioned pseudo-time derivative and not on the physical time-derivative. The resulting diagonal dominance of the scheme allows for unconditional stability of the inner iterations and the pseudo-CFL ( $CFL_\tau$ ) may be picked to be very large ( $1 \times 10^6$  is used here). Fig. 5.5 shows results for  $CFL_{u+c} = 1$  and  $CFL_u = 1$ . Very good damping is again evident under both situations. Results without the unsteady preconditioning matrix suggest poor convergence behavior as discussed earlier. Thus, the preconditioning matrix plays a dominant role in controlling the convergence characteristics of the upwind-based schemes as well. Comparison with Fig. 5.4 also indicates that the LGS scheme generally performs better than the ADI scheme. This is in accordance with experience from steady-state computations (Chapter 4).

Stability studies (not shown here) also confirm the performance capabilities at intermediate time scales that may be encountered in problem involving local grid-stretching. Furthermore, stability results for the DDLU approximate-factorization scheme also reveal unconditional stability of the pseudo-iterations and good convergence behavior at all Mach numbers and time scales. Finally, for convergence results using the dual-time preconditioned algorithm, the reader is referred to Ref. [62].

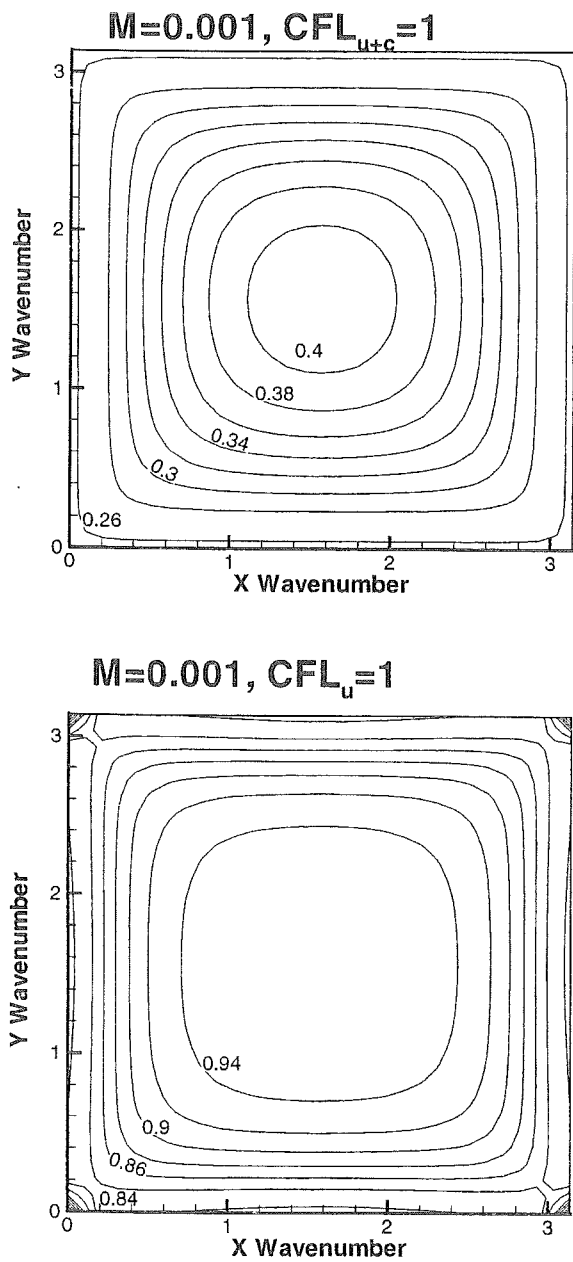


Figure 5.4: Stability Results for Dual Time Scheme, Central-Difference ADI, Unsteady Preconditioning.  $M=0.001$ ,  $\text{CFL}_\tau = 3$ ,  $\text{CFL}_{u+c} = 1$  and  $\text{CFL}_u = 1$ .

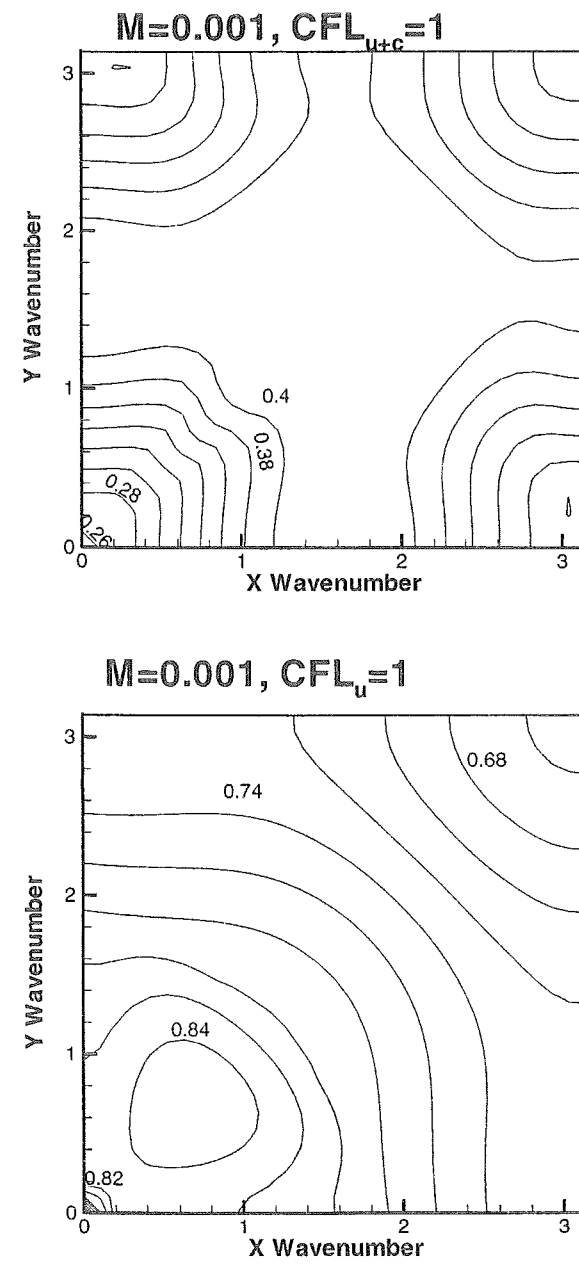


Figure 5.5: Stability Results. Dual-Time Scheme with Unsteady Preconditioning. Upwind DDLGS.  $M=0.001$ ,  $\text{CFL}_\tau = 3$ ,  $\text{CFL}_{u+c} = 1$  and  $\text{CFL}_u = 1$ .

# Chapter 6

## Preconditioning Formulation for Turbulent Reacting Flows

The vast majority of combustion applications take place at low speeds. Representative examples include industrial and residential furnaces, automotive engines, gas turbine engines, rocket combustors, fires, flames and incineration applications. As we have seen traditional time-marching methods fail to converge at low speeds and preconditioning algorithms are necessary to obtain efficient convergence of these problems. Chemically reacting flowfields are rich in physical complexity. In addition to the low flow speeds mentioned above, reacting flowfields are typically characterized by dominant viscous effects, steep flowfield gradients, stiff source terms, strong non-linearities, physical unsteadiness and turbulence. These physical complexities in turn pose fresh challenges to CFD algorithms by exposing inherent weaknesses and usually resulting in lack of code robustness or poor convergence or both. Reacting flow problems therefore offer the ultimate test of the preconditioning procedures developed in the previous chapters, and in addition, they introduce a new difficulty, that due to the combustion source terms.

In this chapter, we extend the preconditioning formulation developed in the previous chapters to the reacting system, comprised of the multiple-species equations and turbulence transport equations coupled to the Navier-Stokes equations. First, we begin with the turbulence equations (we use  $k - \varepsilon$  for demonstration purposes), and then consider the inclusion of multiple species equations. We specifically address numerical difficulties associated with combustion (and turbulence) source terms and suggest means of dealing with them. Finally, we perform several representative computations to demonstrate the capabilities of the method.

### 6.1 Computation of Turbulent Flows

The coupling of turbulence model equations to the fluid equations is usually considered to be rather benign. Most researchers, in fact, choose to de-couple the turbulent system from the Navier-Stokes system and solve the entire system by iterating between the two sets. This loosely coupled approach is usually justified by the fact that the major influence

of the turbulence terms on the fluids equations is through the definition of the turbulent viscosity. Since most CFD algorithms “lag” the viscosity coefficient anyway during the linearization procedure (i.e., it is treated at the known time level  $n$ ), it may be argued that there is not much to be gained by solving the system fully coupled.

The problem with the above argument is that it ignores the effects of the turbulent kinetic energy term in the pressure gradient of the momentum equations (see Appendix A.2). For certain types of flows, researchers are justified in dropping these terms altogether, in which case, of course, they do have any influence on stability. Even when included, it has been suggested that these terms are not important since the turbulent kinetic energy is so much smaller than the thermodynamic pressure. The latter suggestion is specious, however, since it is not the relative magnitudes of the turbulent energy and the pressure that is of concern; rather, it is the comparison between their respective gradients that is relevant. We have seen in the perturbation procedures that the magnitude of the pressure gradient can be very different from that of the thermodynamic pressure. For instance, at low speeds, the pressure gradient is proportional to  $\rho u^2$ . It is evident that the gradient in turbulent kinetic energy can then be of the same order as or greater than the actual pressure gradient. Therefore, the presence of this term in the momentum equation can materially affect the overall stability of the fluids-turbulence system. Because of this coupling effect, in fact, we feel that a fully coupled formulation is desirable and this is the approach that we take in this development.

A further effect of the turbulent kinetic energy term is that it changes the eigenvalues of the system. This may be conveniently expressed as a modified speed of sound,  $c_t = \sqrt{\gamma R T} = \sqrt{\gamma(R + \frac{2}{3}\frac{k}{T})T}$ . For transonic flows, this modification of the speed of sound is admittedly small and does not impact the performance of the algorithm. However, when the system is preconditioned, we replace the physical speed of sound with an artificial speed of sound, which is of the same order as the particle velocity. Indeed, the influence of the kinetic energy term can now become significant and, as we will see presently, it actually introduces a major new difficulty.

The governing equations for the Reynolds-averaged Navier-Stokes equations coupled to the  $k - \varepsilon$  model are given in Appendix A.2,

$$\frac{\partial Q}{\partial \tau} + \frac{\partial E}{\partial x} + \frac{\partial F}{\partial y} = H + \mathcal{L}(Q_p) \quad (6.1)$$

where  $H$  is the source term that contains the production and dissipation terms of the turbulent kinetic energy and dissipation. We note for clarity that the vectors  $Q$  and  $Q_p$  are given as,

$$Q = \begin{pmatrix} \rho \\ \rho u \\ \rho v \\ e \\ \rho k \\ \rho \varepsilon \end{pmatrix} \quad Q_p = \begin{pmatrix} p \\ u \\ v \\ T \\ k \\ \varepsilon \end{pmatrix}$$

The preconditioned version of these equations may be derived in the standard manner by performing a change of variable from  $Q$  to  $Q_p$  in the time-derivative,

$$\frac{\partial Q}{\partial Q_p} \frac{\partial Q_p}{\partial \tau} + \frac{\partial E}{\partial x} + \frac{\partial F}{\partial y} = H + \mathcal{L}(Q_p) \quad (6.2)$$

Preconditioning the system in Eqn. 6.2 involves replacing the transformation Jacobian by the preconditioning matrix, which has the same form as the above matrix, except that  $\rho_p$  is replaced by  $\rho'_p$ . Thus, we have,

$$\Gamma_p \frac{\partial Q_p}{\partial \tau} + \frac{\partial E}{\partial x} + \frac{\partial F}{\partial y} = H + \mathcal{L}(Q_p) \quad (6.3)$$

where the preconditioning matrix is given as,

$$\Gamma_p = \begin{pmatrix} \rho'_p & 0 & 0 & \rho_T & 0 & 0 \\ u\rho'_p & \rho & 0 & u\rho_T & 0 & 0 \\ v\rho'_p & 0 & \rho & v\rho_T & 0 & 0 \\ h_o\rho'_p - (1 - \rho h_p) & \rho u & \rho v & h_o\rho_T + \rho h_T & \rho & 0 \\ k\rho'_p & 0 & 0 & k\rho_T & \rho & 0 \\ \varepsilon\rho'_p & 0 & 0 & \varepsilon\rho_T & 0 & \rho \end{pmatrix}$$

This straightforward extension of the preconditioning methodology to the coupled fluids-turbulence equations unfortunately does not work very well. The reason is the presence of the turbulent kinetic energy in the pressure gradient term as discussed earlier. The inviscid eigenvalues of the coupled preconditioned system, including the turbulent kinetic energy terms in the pressure gradient, are now complex. Although the imaginary part of the eigenvalues are large only for high levels of turbulence, it is still undesirable for many reasons. For one, the system is no longer strictly hyperbolic, which means that it is not well-posed for time-marching. Indeed, it may lead to solution divergence. Further, it creates difficulties with the formulation of characteristic-based upwind schemes and boundary condition specification. One approach may be to drop the offending terms from the inviscid Jacobian (but retain them in the residual). However, we have observed lack of robustness and poor convergence characteristics with such a formulation. It is therefore necessary to modify the preconditioning formulation to render the turbulent system well-posed.

Fortunately, this is readily accomplished by a simple transformation of variables. The essence of the idea lies in the realization that  $(\partial \rho / \partial p)_s$  no longer represents the effective sound speed (squared) of the system. Rather, the effective sound speed is obtained from the modified property derivative,  $(\partial \rho / \partial p_t)_s$ , where the new variable,  $p_t$  is a “turbulent” pressure that is defined as,  $p_t = p + \frac{2}{3}\rho k$ . We therefore conclude that proper term to be scaled by the preconditioning is the derivative involving the turbulent pressure,  $\partial \rho / \partial p_t$  and not  $\rho_p$ . In order to carry out this preconditioning, we introduce a new variable vector,  $\tilde{Q}_p$ , and re-write Eqn. 6.2 as,

$$\frac{\partial Q}{\partial \tilde{Q}_p} \frac{\partial \tilde{Q}_p}{\partial \tau} + \frac{\partial E}{\partial x} + \frac{\partial F}{\partial y} = H + \mathcal{L}(Q_p) \quad (6.4)$$

where  $\tilde{Q}_p$  is given as,

$$\tilde{Q}_p = \begin{pmatrix} p_t \\ u \\ v \\ T \\ k \\ \varepsilon \end{pmatrix}$$

Note that  $\tilde{Q}_p$  should not be confused with the dependent variable defined in the perturbation equation system in Section 2.1.4.

The new Jacobian now contains property terms which are derivatives with respect to the  $\tilde{Q}_p$  vector. Preconditioning this system involves replacing the new  $\tilde{\rho}_p = (\partial\rho/\partial p_t)$  derivatives with the preconditioning parameter,  $\tilde{\rho}'_{p_t}$ . The preconditioning system is then given by,

$$\tilde{\Gamma}_p \frac{\partial \tilde{Q}_p}{\partial \tau} + \frac{\partial E}{\partial x} + \frac{\partial F}{\partial y} = H + \mathcal{L}(Q_p) \quad (6.5)$$

and

$$\tilde{\Gamma}_p = \begin{pmatrix} \tilde{\rho}'_{p_t} & 0 & 0 & \tilde{\rho}_T & \tilde{\rho}_k & 0 \\ u\tilde{\rho}'_{p_t} & \rho & 0 & u\tilde{\rho}_T & u\tilde{\rho}_k & 0 \\ v\tilde{\rho}'_{p_t} & 0 & \rho & v\tilde{\rho}_T & v\tilde{\rho}_k & 0 \\ h_o\tilde{\rho}'_{p_t} - (1 - \rho\tilde{h}_{p_t}) & \rho u & \rho v & h_o\tilde{\rho}_T + \rho\tilde{h}_T & \frac{5}{3}\rho + \tilde{\rho}_k + h_o\tilde{\rho}_k & 0 \\ k\tilde{\rho}'_{p_t} & 0 & 0 & k\tilde{\rho}_T & \rho + k\tilde{\rho}_k & 0 \\ \varepsilon\tilde{\rho}'_{p_t} & 0 & 0 & \varepsilon\tilde{\rho}_T & \varepsilon\tilde{\rho}_k & \rho \end{pmatrix}$$

where  $\tilde{\rho}'_{p_t}$  is the preconditioning parameter and is defined in the usual manner.

The property derivatives in the preconditioning matrix are defined as,

$$\tilde{\rho}_{p_t} = \varphi\rho_p \quad \tilde{\rho}_T = \varphi\rho_T \quad \tilde{\rho}_k = -\frac{2}{3}\varphi\rho\rho_p$$

$$\tilde{h}_{p_t} = \varphi h_p \quad \tilde{h}_T = h_T - \frac{2}{3}\varphi k\rho_T h_p \quad \tilde{h}_k = -\frac{2}{3}\varphi\rho h_p$$

where  $\varphi = 1/(1 + \frac{2}{3}k\rho_p)$ . Note that for the new system,  $\tilde{\rho}_k$  and  $\tilde{h}_k$  are not zero because of the dependence of  $p_t$  on  $k$ .

The preconditioning system in Eqn. 6.5 possesses all real eigenvalues, which are, in fact, the same as those for the Euler and laminar Navier-Stokes systems (see Appendix B).

## 6.2 Computation of Reacting Flows

### 6.2.1 Preconditioning System for Reacting Flows

The governing equations for reacting flows typically include the Reynolds-averaged Navier-Stokes equations coupled to transport equations for the species mass fractions and the

turbulence quantities. The equations are summarized in Appendix A.2. The corresponding preconditioning system may be derived in the same manner as for the turbulent system in the previous section. The resulting system is given as,

$$\tilde{\Gamma}_p \frac{\partial \tilde{Q}_p}{\partial \tau} + \frac{\partial E}{\partial x} + \frac{\partial F}{\partial y} = H + \mathcal{L}(Q_p) \quad (6.6)$$

and

$$\tilde{\Gamma}_p = \begin{pmatrix} \tilde{\rho}'_{pt} & 0 & 0 & \tilde{\rho}_T & \tilde{\rho}_k & 0 & \tilde{\rho}_{Y_j} \\ u\tilde{\rho}'_{pt} & \rho & 0 & u\tilde{\rho}_T & u\tilde{\rho}_k & 0 & u\tilde{\rho}_{Y_j} \\ v\tilde{\rho}'_{pt} & 0 & \rho & v\tilde{\rho}_T & v\tilde{\rho}_k & 0 & v\tilde{\rho}_{Y_j} \\ h_o\tilde{\rho}'_{pt} - (1 - \rho\tilde{h}_{pt}) & \rho u & \rho v & h_o\tilde{\rho}_T + \rho\tilde{h}_T & \frac{5}{3}\rho + \rho\tilde{h}_k + h_o\tilde{\rho}_k & 0 & h_0\tilde{\rho}_{Y_j} + \rho\tilde{h}_{Y_j} \\ k\tilde{\rho}'_{pt} & 0 & 0 & k\tilde{\rho}_T & \rho + k\tilde{\rho}_k & 0 & k\tilde{\rho}_{Y_j} \\ \varepsilon\tilde{\rho}'_{pt} & 0 & 0 & \varepsilon\tilde{\rho}_T & \varepsilon\tilde{\rho}_k & \rho & \varepsilon\tilde{\rho}_{Y_j} \\ Y_i\tilde{\rho}'_{pt} & 0 & 0 & Y_i\tilde{\rho}_T & Y_i\tilde{\rho}_k & 0 & Y_i\tilde{\rho}_{Y_j} + \rho\delta_{ij} \end{pmatrix}$$

where the property functions are the same as those defined in the previous section. The new terms are given as,

$$\tilde{\rho}_{Y_i} = \varphi\rho_{Y_i} \quad \tilde{h}_{Y_j} = \varphi h_{Y_i}$$

The eigenvalues of the above system are the same as for the fluids system given in Appendix B. In the following sections, we examine numerical issues that arise with the treatment of chemical source terms and then present computational results for representative reacting flow problems.

### 6.2.2 Numerical Issues in Reacting Computations

Subsonic combustion problems are typically characterized by high volumetric energy release rates and increased disparity between flow and reaction time scales. The treatment of the chemical source terms therefore presents unique difficulties to numerical algorithms. As we will see, this is particularly the case during the initial stages of a reacting flow computation, wherein high levels of species and heat release may change the local gas properties and temperatures by more than an order of magnitude. In this section, we examine numerical issues associated with solving combustion problems and, in particular, we address the treatment of source terms.

We begin by reviewing the form of the source terms that arise when using finite-rate chemistry models. We then consider stability behavior of sources and sinks and use this understanding to analyze the numerical behavior of combustion source terms. In these studies, we use a zero-dimensional combustion problem, which consists of a system of ordinary differential equations, and use the understanding gained from the relatively simple analysis to improve our understanding of multi-dimensional combustion computations.

## Chemistry Model

The source vector  $H$  contains the source terms due to combustion and turbulence. The combustion source term in the species equations,  $\dot{w}_i$ , is obtained by summing the species generation contributions from the various elemental reactions. This is written as:

$$\dot{w}_i = M_i \sum_{k=1}^{NR} (\dot{c}_i)_k \quad (6.7)$$

where  $NR$  is the total number of reactions.  $(\dot{c}_i)_k$  is the rate of production of moles of species  $i$  by reaction  $k$ ,

$$(\dot{c}_i)_k = (\nu_{ik}'' - \nu'_{ik})(k_{fk} \prod_{m=1}^N C_m^{\nu'_m} - k_{bk} \prod_{m=1}^N C_m^{\nu''_m})$$

where the  $k^{th}$  reaction is written as:

$$\sum_{i=1}^N \nu'_{ik} M_i \rightleftharpoons \sum_{i=1}^N \nu''_{ik} M_i$$

Here,  $\nu'_{ik}$  and  $\nu''_{ik}$  are the stoichiometric coefficients for the  $i^{th}$  species,  $k_{fk}$  and  $k_{bk}$  are the forward and backward reaction rates and  $M_i$  is the molecular weight of the  $i^{th}$  species.  $C_i$  is the molar concentration of the species and is given by  $C_i = \frac{\rho Y_i}{M_i}$ .

## Numerical Behavior of Combustion Source Terms

We consider the following system of ordinary differential equations (or ODE's),

$$\frac{\partial \rho Y_i}{\partial t} = \dot{w}_i \quad (6.8)$$

which is augmented by the condition that the total energy of the system,  $e$ , remains constant. The resulting initial value problem follows the evolution of species in an enclosed container and is therefore commonly referred to as a constant-volume bomb calculation.

Although ODE packages for the solution of Eqn. 6.8 are widely available, we perform numerical solutions of this system to understand the difficulties involved. This simple ODE in fact contains much of the inherent complexity of combustion systems, while providing useful insight into the physical and mathematical character of the chemical source terms. We express the numerical solution of the system of ODE's by using Euler implicit temporal integration. While this is clearly not sufficiently time-accurate, it mimics the integration commonly employed in implicit CFD algorithms. The Euler implicit scheme in delta form is given as,

$$[I - \Delta t \theta D] \Delta \rho Y_i = \Delta t \dot{w}_i \quad (6.9)$$

Here,  $\theta = 1$  for Euler implicit, it is equal to 0 for Euler explicit and is 1/2 for Crank-Nicholson temporal discretization.  $D$  is the Jacobian of the source term and  $\Delta t$  is the time-step.

Conventional wisdom has it that fully implicit treatment of the source term is unconditionally stable. However, linear stability theory reveals that the statement is true only with regard to sinks and not for positive sources. This is readily confirmed by considering the scalar counter-part of Eqn. 6.9, in which case the amplification factors are given as,

$$g_{imp} = \frac{1}{1 - \beta} \quad g_{exp} = 1 + \beta \quad (6.10)$$

where  $\beta = d\Delta T$  and  $d$  is the scalar counter-part of the Jacobian  $D$ . When  $d$  is negative, it corresponds to a sink term. In that case,  $g_{imp}$  is always stable, while  $g_{exp}$  is conditionally stable. On the other hand, when  $d$  is positive, it corresponds to a source. Both schemes are then observed to permit growing modes, but when compared to the analytical growth rate for the source, it is clear that the *explicit* treatment is unconditionally stable, while the implicit treatment is only conditionally stable. In fact, Eqn. 6.10 shows that, as  $\beta \rightarrow 1$ , the implicit amplification factor blows up. Interestingly, for  $\beta > 2$ , the LHS of Eqn. 6.9 becomes negative definite and the source starts to behave like a sink. While the scheme is stable for such values of  $\beta$ , frequently, under such circumstances, the temporal integration converges to the wrong solution.

Linear stability theory therefore suggests that sinks should be treated implicitly and sources must be treated explicitly for unconditional stability. One must qualify the latter part of the statement with the observation that large positive sources typically lead to strongly non-linear behavior, so linear stability in this regime is not a sufficient condition for stability by any means. Still, the stability analysis does point to the fact that positive sources treated implicitly may cause instability or physical time-reversal. Further, we conclude that, for implicit treatment of sources, stability is ensured only if  $\beta$  is sufficiently small.

Turning our attention back to the vector system of ODE's in Eqn. 6.9, we note that for general chemical kinetics, the chemical source Jacobian is composed of both positive and negative eigenvalues. Interestingly, the precise source/sink combination varies during the temporal development of the combustion problem. Typically, the process is composed of three distinct stages—namely, a species induction phase, a heat-release phase and an equilibrating phase. Positive sources are usually present only during the induction and heat-release stages of the computation (though they are generally mixed in with some negative eigenvalues). The later equilibration phase is then characterized by purely negative eigenvalues or sinks.

A further aspect of the induction and heat-release stages is that non-linear effects usually dominate. This is, in part, due to the presence of positive sources that lead to an exponential growth of species mass fractions along with a rapid increase in the temperature. We therefore characterize the early source-dominated stages, as the “non-linear” computational regime, while the later equilibration phase, we refer to as the “linear” regime.

Figures 6.1 to 6.4 illustrate these stages clearly. The results are for a hydrogen-oxygen constant-volume bomb computation with a eight species/eighteen reactions kinetics package. Two cases corresponding to initial pressures of 1 atm and 30 atm are shown.

Figure 6.1 shows the plot of temperature vs. time. Both cases show the induction, heat-release and equilibrating phase. The heat-release stage is, of course, characterized by a rapid increase in temperature. For the lower pressure case, the rate of temperature rise is relatively modest, while the higher pressure case, shows an almost instantaneous rise in the temperature.

Figure 6.2 shows the magnitude of the maximum eigenvalue of the chemical Jacobian. As discussed earlier, positive eigenvalues are present only during the induction and heat release stages. During the final equilibrating phase, both cases show that the maximum eigenvalue is zero, indicating the absence of positive sources. Note also that during the initial stages, the magnitudes of these positive eigenvalues are extremely large. By considering the scale of the time-axis, one can see that if time-steps of the order of  $10^{-6}$  seconds are used, the product  $\lambda\Delta t$  would be of the order of unity or more. Figure 6.3 shows the magnitudes of the corresponding minimum eigenvalues (which are sinks). It is seen that large sink eigenvalues are present throughout the computation, but they become especially strong in the equilibrating phase. This indicates that the system is approaching a stable state as the combustion progresses.

In order to compute the combustion process, one must keep in mind that the algorithm must be stable in the equilibrating phase. Given the large magnitudes of the sink eigenvalues, there is no question that implicit source treatment is necessary. Further, because of the complexity of the chemical source terms, it is very difficult to separate out positive and negative eigenvalues. Therefore, it is not practical to treat sources and sinks differently. Such a treatment would not guarantee stability anyway during the induction and heat release stages because of the strong non-linearities that are present. Thus, during the non-linear regime, it is necessary to stabilize the computation through judicious selection of the time-step size.

In general, one needs to account for the positive eigenvalues in selecting the time-step size. In the present computations, the time-step size was selected based upon keeping  $\lambda\Delta t$  about 0.1. Further, the time-step was also selected to ensure that the temperature changed by a maximum of 10% over each time-step. This latter criterion ensures that the corrections introduced by the linear scheme do not drive the solution unstable. Figure 6.4 shows the resulting time-step selection using these criteria. It is observed that the more benign  $P = 1$  atm case requires a time-step reduction of about a factor of 10 to 20 (from  $10^{-6}$  s to maintain stable temporal evolution during the non-linear stages. Once the equilibrating stage is reached, the unconditional linear stability of the scheme allows the choice of large time-steps. The higher pressure case shows a very sharp dependence of the time-step size near the region of exponential growth. The time-step is, in fact, lowered to about  $5 \times 10^{-9}$  s for this case, to maintain stability. After the heat release stage is over, it is possible to ramp the time-step up very quickly.

The detailed study of the zero-dimensional constant-volume bomb computation has provided useful insight into the process of initializing a flame. This naturally has profound implications on the performance and robustness of multi-dimensional problems as well. We discuss these issues in the following section.

# Hydrogen/Oxygen Combustion

## Constant-Volume Bomb

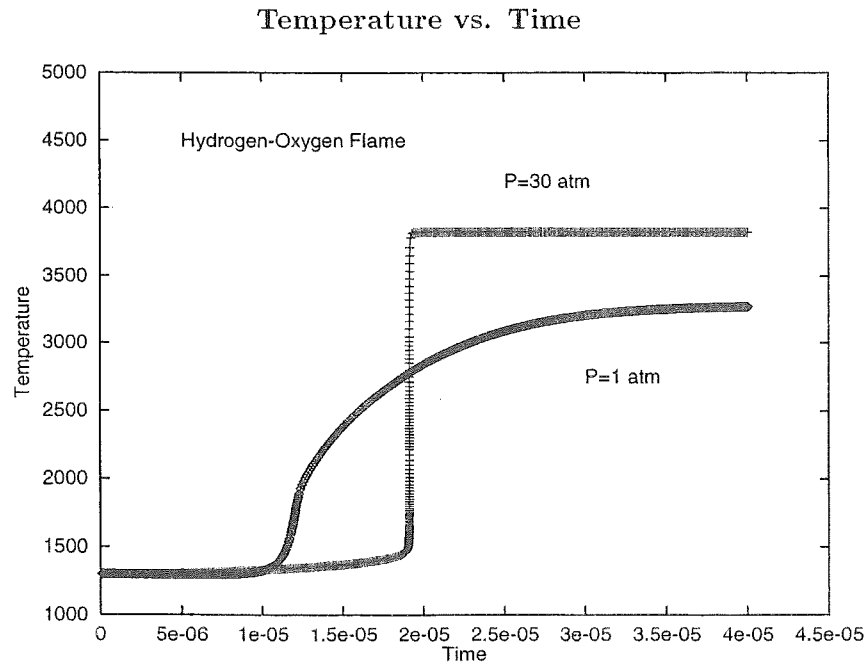


Figure 6.1: Hydrogen/Oxygen Constant Volume Bomb. Temperature vs. Time.

# Hydrogen/Oxygen Combustion

## Constant-Volume Bomb

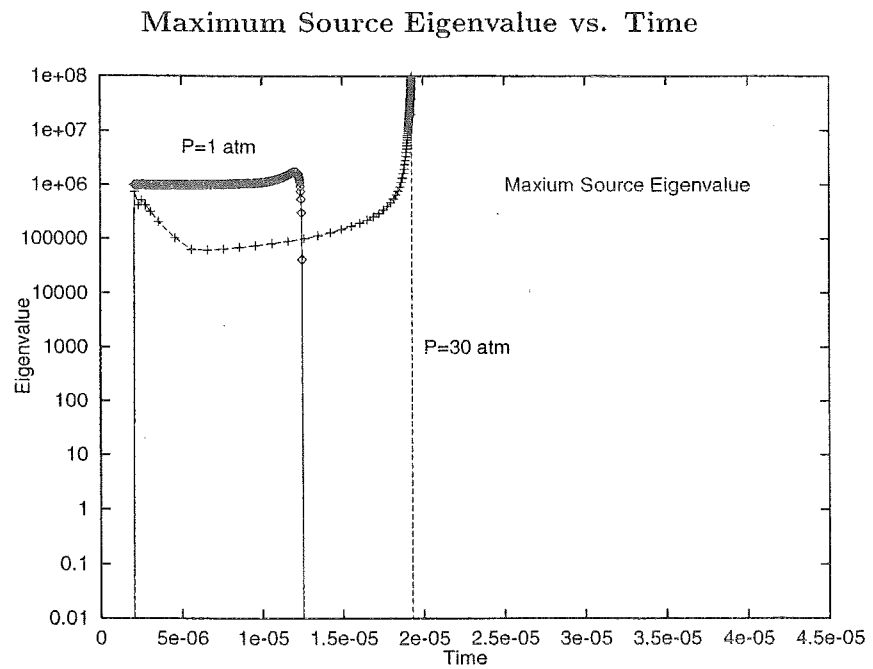


Figure 6.2: Hydrogen/Oxygen Constant Volume Bomb. Maximum Eigenvalue vs. Time.

# Hydrogen/Oxygen Combustion

## Constant-Volume Bomb

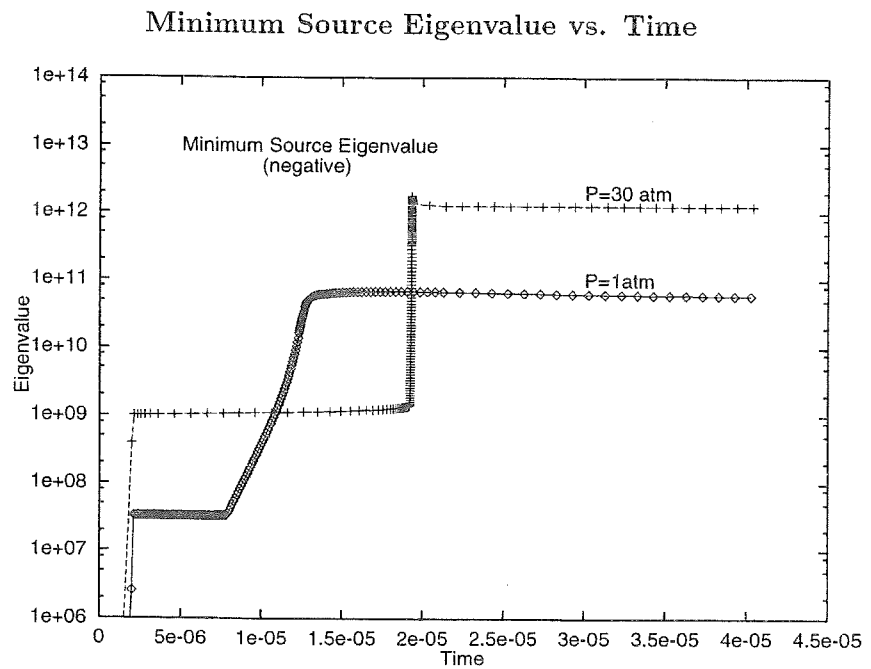


Figure 6.3: Hydrogen/Oxygen Constant Volume Bomb. Minimum Eigenvalue (Magnitude) vs. Time.

# Hydrogen/Oxygen Combustion

## Constant-Volume Bomb

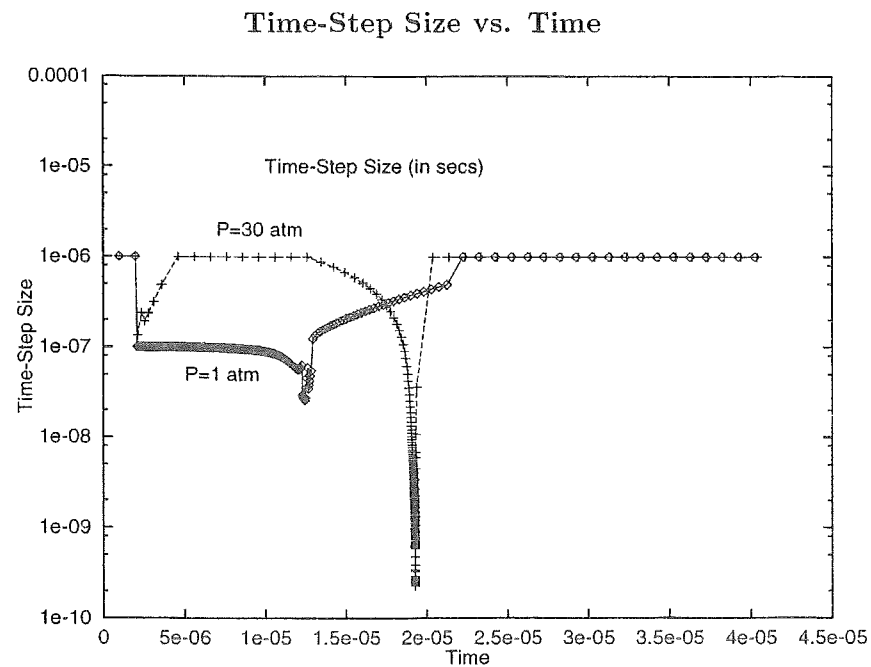


Figure 6.4: Hydrogen/Oxygen Constant Volume Bomb. Time-Step Size vs. Time.

## Implications of Combustion Source Treatment

The process of initializing a multi-dimensional flowfield is similar to the combustion process in the constant volume bomb. Initially, when fuel and oxidizer come into contact (in a diffusion flame), the grid points where this occurs are characterized by dominant source terms and the equations resemble the ODE system. During this non-linear phase, the choice of time-step from the convective/diffusive terms (i.e., the CFL/VNN number definitions) would typically prove to be unacceptably large and result in unstable behavior. Once the flame computation has been “nursed” through this initial non-linear phase, and the flowfield has been established, the computation enters the linear phase. Here, most of the flowfield is characterized by sink terms and system is stable. Even near the flamefront where positive eigenvalues would still remain, the chemical source terms are adequately balanced by the convective and diffusive terms. During this linear stage, the time-step size may be specified by the convective and diffusive terms and convergence rates similar to non-reacting flow is typically possible.

Thus, the major difficulty with computing reacting flows is the initial non-linear stage. Indeed, the best way to ensure stable flame flowfield development would be to locally select the time-step according to the size of the source Jacobian eigenvalues and the rate of change of the solution (usually temperature). However, this method is very expensive in general, although it may be possible to minimize the eigenvalue computations by devising an algorithm to intelligently select when a grid point needs such time-step control [66].

The present authors have preferred to employ a more *ad-hoc* method of time-step control, usually in combination with reducing the reaction rates and heats of formation. Since in steady-state combustion computations, the transient is not of interest, slowing down the combustion process enables the initialization of the flame to progress more smoothly. Once the flame is successfully initialized, it is typically possible to ramp up the time-steps, reaction rates and heats of formation to their normal operating values and reliable convergence behavior is obtained from that juncture. In the following section, we will demonstrate several practical reacting flow computations.

### 6.2.3 Computational Examples

#### Methane-Air Laminar Diffusion Flame

As an initial demonstration of the preconditioned method, we consider the methane-air axisymmetric laminar diffusion flame experiment of Mitchell *et al* [74]. The converged temperature contours for this case are shown in Fig. 6.5. The grid size used is 101 X 61. The set-up consists of an inner fuel jet of radius 0.635 cm and an outer oxidizer (air) jet with an outer radius of 2.54 cm. The length of the tube is 30 cm. The inlet velocity of the methane gas is 4.5 cm/s and that of the air is 9.88 cm/s. The temperature of the gases as well as of the tube walls are maintained at 300 K. Because of the low velocities of the gases, buoyancy effects are present in the flame. However, in the computational results shown, buoyancy was neglected because, in the presence of buoyancy, long recirculation regions are set up that extend up to the tube outlet, leading to uncertainties in the boundary

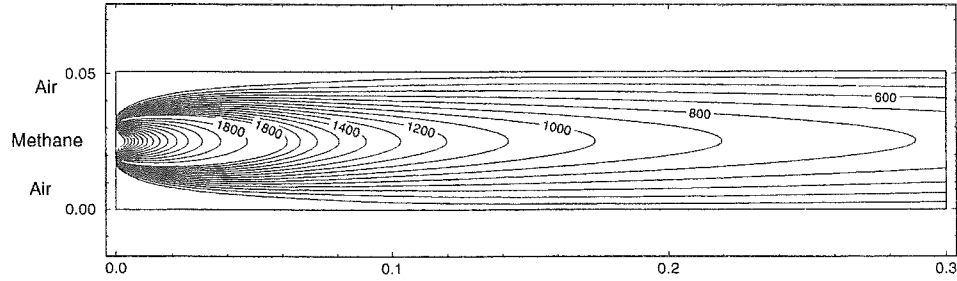


Figure 6.5: Temperature contours for methane/air laminar diffusion flame.

condition specification. For the combustion model, a global two-step kinetics model is employed involving  $CH_4$ ,  $O_2$ ,  $CO$ ,  $CO_2$ ,  $H_2O$  and  $N_2$ .

Convergence results are shown in Fig. 6.6 for both non-reacting and reacting computations using the preconditioned algorithm as well as for the reacting case without preconditioning and aspect ratio control. Good convergence is evident when preconditioning is used. For the reacting case, the initial portion of the convergence corresponds to the initialization of the flame flowfield. In this case, a steady torch at 2000 K was maintained at the inlet until combustion was initiated. During this period, the reaction rates were scaled down by a factor of ten and the CFL and VNN numbers maintained at unity. After 500 iterations, the torch was turned off and the time-steps progressively scaled to their optimum values. Beyond that juncture, the reacting computation is seen to converge at virtually the same rate as the non-reacting computation, reaching close to machine zero in about 1000 iterations.

In contrast, the convergence of the reacting case for the non-preconditioned system is extremely poor due to the low velocities characterizing the flowfield. Finally, for the case with inviscid preconditioning but without the aspect ratio modifications discussed in Chapter 4, convergence during the initialization phase is seen to be about the same as the preconditioned case but, is noticeably worse in the ‘linear’ phase of the computation. This is because the initial phase is dominated by the heat release effects of the combustion, while in the latter part of the computation, the convective/diffusive effects control the convergence behavior.

Experimental findings indicate a peak flame temperature of 2000 K and a flame length of about 6 cm, which are in good general agreement with the numerical results. Figure 6.7 shows the comparison of the predicted species profiles with experimental data at a given axial location ( $x = 1.2$  cm). The agreement is observed to be fairly good with some notable discrepancies. First, the methane concentration near the centerline is much higher than the measured value. This discrepancy has been observed by other researchers as well and may be attributed to inaccuracies in the experimental data close to the centerline. Secondly, the computed flame is located further into the oxidizer stream than in the experiments. This discrepancy is related to flow recirculation due to buoyancy effects, which tends to confine the flame more tightly along the axis of the tube.

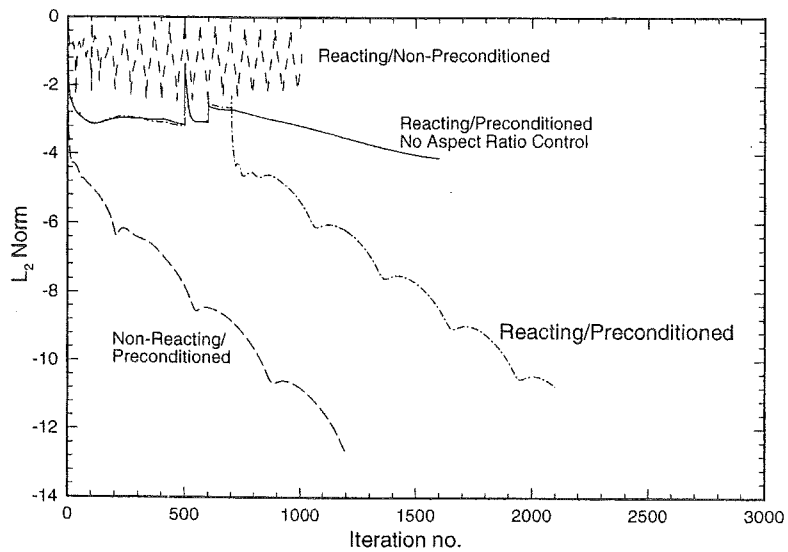


Figure 6.6: Convergence results for methane/air laminar diffusion flame.

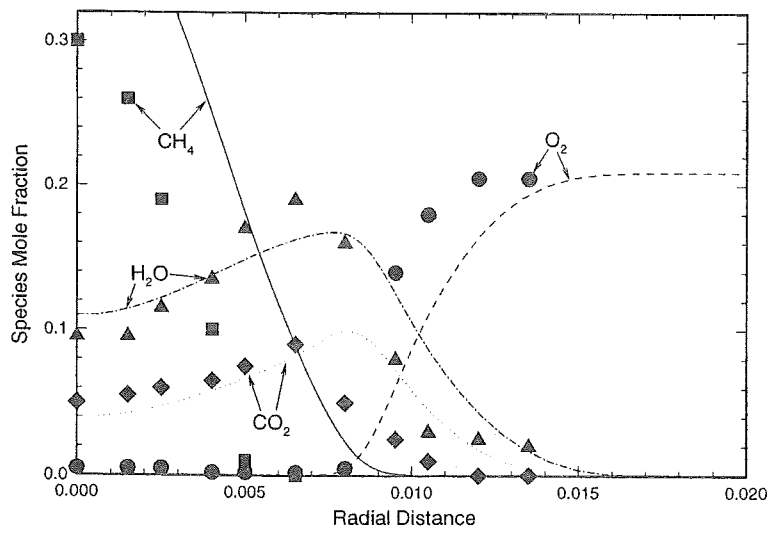


Figure 6.7: Comparison of species profiles for methane/air laminar diffusion flame.

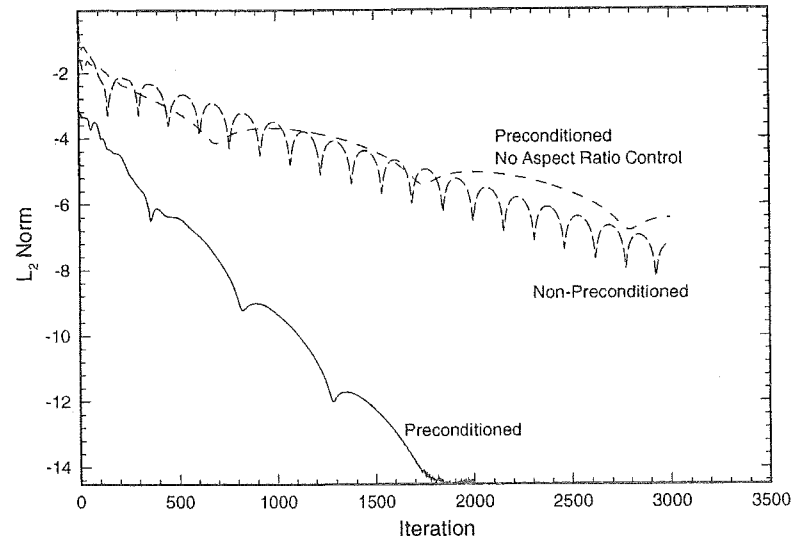


Figure 6.8: Convergence results for non-reacting turbulent shear layer.

### Non-Reacting Turbulent Shear Layer

The next two sets of computations correspond to the experimental studies on turbulent mixing in non-reacting and reacting shear layers performed at NASA/Lewis Research Center [75]. The non-reacting case is comprised of a planar mixing layer with the lower air stream conditions being:  $U_1 = 390\text{m/s}$  and  $T_1 = 822\text{K}$ , while the upper air stream conditions are:  $U_2 = 140\text{m/s}$  and  $T_2 = 304.3\text{K}$ . The corresponding Mach numbers of the two streams are 0.68 and 0.4 respectively. The grid size used in the present calculations is 81 X 81 with strong clustering in the mixing region.

Figure 6.8 shows the convergence for the preconditioned and non-preconditioned systems as well as for the preconditioned system without aspect ratio control. In contrast to the laminar diffusion flame presented earlier, we employ third-order upwind-biased differencing of the convective fluxes. Because of the steep gradients, central differences show evidence of oscillatory behavior. Again, the preconditioned system displays excellent convergence rates reaching machine zero in about 2000 iterations. On the other hand, the convergence for the other two cases are worse by a factor of two or three, primarily because of the long grid cells in the mixing region of the shear layer.

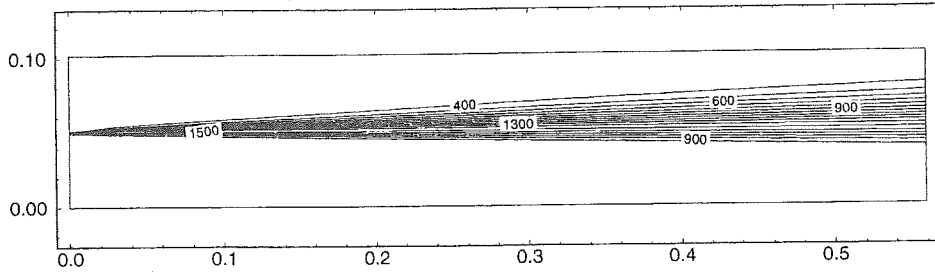


Figure 6.9: Temperature Contours for reacting turbulent shear layer.

### Reacting Turbulent Shear Layer

We next consider the reacting case corresponding to the above configuration. Here, the lower air stream conditions are:  $U_1 = 390\text{m/s}$  and  $T_1 = 810.9\text{K}$ , while the upper stream is now comprised of 96.06%  $N_2$  and 3.94%  $H_2$  by mass with the conditions being:  $U_2 = 140\text{m/s}$  and  $T_2 = 366.5\text{K}$ . The inlet RMS velocities are specified to be 6% and 11% of the axial velocities of the lower and upper streams respectively. In order to hold a stable flame, the experiments employed a continuous ignition source in the form of a hydrogen torch located at the upstream end. A similar ignition source was maintained in the computations as well. For the combustion model, a detailed kinetics set of eighteen elementary reactions and nine chemical species is used. Figure 6.9 shows temperature contours for the reacting flow case with a grid size of 81 X 81 and upwind representation of the convective fluxes.

Convergence for the reacting case is shown in Fig. 6.10. In order to initialize the flame, in this case, the species time-steps were scaled down and the value gradually increased after about 300 iterations. The procedure performed remarkably well for this test case as evidenced by the convergence curve. Further, the overall convergence rate is seen to be quite efficient with the residuals dropping by about ten orders of magnitude in 3000 iterations. It should be pointed out that additional calculations, performed with different inlet turbulent intensities, sometimes showed evidence of physical unsteadiness. In such cases, convergence tended to flatten out after a few to several orders of residual reduction.

Comparison of axial velocity and turbulence profiles with experimental data is shown in Fig. 6.11. The velocity profiles show fairly good agreement with the data near the inlet section but, further downstream, the experiments indicate stronger mixing into the upper stream. The RMS fluctuations show similar disagreement at the downstream section as well as discrepancies near the inlet. Various reasons may be responsible for the discrepancies. Firstly, the experiments indicate a strong normal velocity component at the inlet in the region where the hydrogen torch is located. Secondly, experimental data also indicate significant anisotropy in the velocity fluctuations outside the mixing layer which are not accounted for in the  $k - \epsilon$  model. Finally, unsteady effects related to large-scale roll-up may explain the stronger mixing of the reacting shear layer with the upper stream. Indeed, reacting flow computations often show evidence of such unsteadiness.

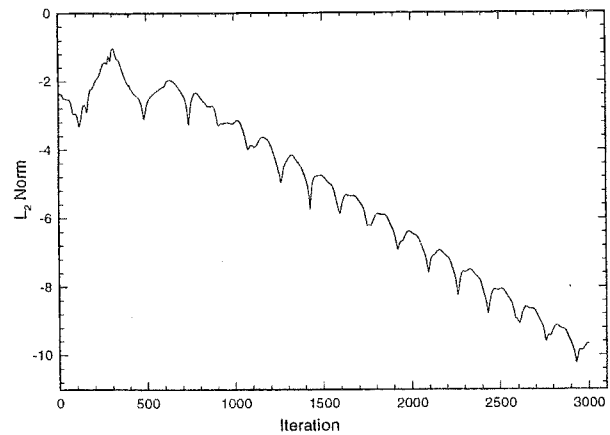


Figure 6.10: Convergence results for reacting turbulent shear layer.

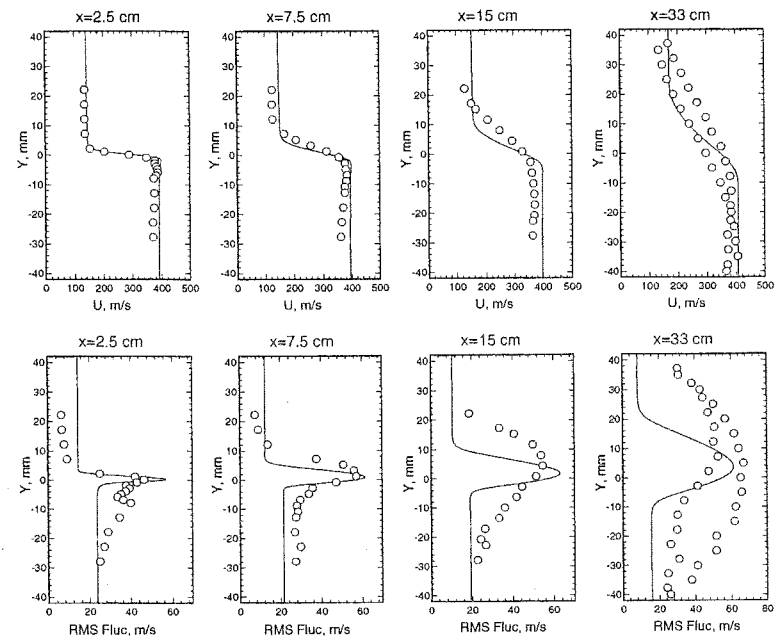


Figure 6.11: Comparison with experimental data for reacting turbulent shear layer.

# Chapter 7

## Conclusions

We have discussed the evolution, development, and application of preconditioning methods. The intention of the presentation has been to elucidate the principles underlying the method. We have emphasized that the particular advantage of using time-marching methods is that they allow the interpretation of mathematical convergence in terms of the unsteady physical processes. Preconditioning offers a way of building upon this understanding to enhance algorithmic performance.

Preconditioning methods were originally devised for improving the performance of time-marching methods at low speeds. Time marching methods have historically suffered at low speeds because the stiffness between the particle wave speeds and the acoustic wave speeds hinder the transport of errors within the system. Like its forerunner the artificial compressibility formulation, preconditioning methods replace the standard physical time derivatives with a set of artificial time derivatives, which render the wave speeds comparable in magnitude and, thereby, allow efficient removal of errors from the system.

Over the years, preconditioning methods have grown in popularity and have been applied to a wide range of problems. Further, the preconditioning methodology has been adapted to optimize the system characteristics and enhance performance over a wide range of flow regimes including viscous-dominated flows, unsteady flows, stretched grid flows, turbulent flows, multi-phase flows, etc. With these developments, preconditioning is becoming established as a fundamental framework with which one can construct general numerical algorithms.

Our study of preconditioning has been based upon three analytical approaches—namely, perturbation analysis, stability analysis and convergence analysis. Perturbation analysis has particular relevance to preconditioning since perturbation methods have been classically used to probe the behavior of the fluids equations under asymptotic limiting conditions such as low Mach number and low Reynolds number. We have demonstrated how the asymptotic expansions may be used to diagnose convergence difficulties and then used to devise preconditioning procedures to eliminate the problems. Furthermore, we have shown how they may be used to assess artificial dissipation terms and, hence, the accuracy of the discrete representations as well.

Stability analysis is an invaluable tool for the CFD practitioner. It serves as a predic-

tive tool for estimating the performance of numerical methods. It provides a quantitative estimate of convergence rate and thereby allows us to verify the physical trends indicated by the time-marching formulation. We have demonstrated, for instance, how stability analysis may be used to probe high aspect ratio convergence behavior.

Convergence analysis completes our trio of analytical tools. It enables practical testing of methods and computer codes. Throughout this presentation, we have employed convergence studies to scrutinize the performance of schemes in a methodical manner. In particular, we have chosen to study simple model problems that allow us to isolate the controlling issues and assess them parametrically.

Preconditioning promises to continue playing an important role in the convergence acceleration of CFD algorithms. A particular trend in the CFD research community is to combine preconditioning techniques with other convergence enhancement methods such as multigrid or GMRES in order to maximize the performance benefits to both classes of schemes. Furthermore, as CFD algorithms are called upon to solve problems of increasing physical complexity, preconditioning methods also need to evolve to face the new challenges.

# Appendix A

## Governing Equations

### A.1 Fluid-Dynamic Equations

#### A.1.1 1D Navier-Stokes Equations

The one-dimensional Navier-Stokes equations are given as:

$$\frac{\partial Q}{\partial t} + \frac{\partial E}{\partial x} = \frac{\partial V}{\partial x} \quad (\text{A.1})$$

where the flux vectors are defined as:

$$Q = \begin{pmatrix} \rho \\ \rho u \\ e \end{pmatrix} \quad E = \begin{pmatrix} \rho u \\ \rho u^2 + p \\ (e + p)u \end{pmatrix} \quad V = \begin{pmatrix} 0 \\ \mu \frac{\partial u}{\partial x} \\ \kappa \frac{\partial T}{\partial x} + \mu u \frac{\partial u}{\partial x} \end{pmatrix}$$

Note that in writing the viscous terms, we have omitted the second coefficient of viscosity for simplicity.

#### A.1.2 2D Navier-Stokes Equations

The two-dimensional Navier-Stokes equations are given as,

$$\frac{\partial Q}{\partial t} + \frac{\partial E}{\partial x} + \frac{\partial F}{\partial y} = \mathcal{L}(Q_p) \quad (\text{A.2})$$

where the vectors Q, E and F are defined as,

$$Q = \begin{pmatrix} \rho \\ \rho u \\ \rho v \\ e \end{pmatrix} \quad E = \begin{pmatrix} \rho u \\ \rho u^2 + p \\ \rho uv + p \\ (e + p)u \end{pmatrix} \quad F = \begin{pmatrix} \rho v \\ \rho uv \\ \rho v^2 + p \\ (e + p)v \end{pmatrix}$$

and the total energy per unit volume is defined as,

$$e = \rho h_o - p = \rho[\epsilon + \frac{1}{2}(u^2 + v^2)]$$

Here,  $\epsilon$  is the internal energy per unit mass.

The viscous terms are represented by the operator  $\mathcal{L}(Q_p)$ , where  $Q_p = (p, u, v, T)^T$  is the primitive variables vector, and  $\mathcal{L}$  is defined as,

$$\mathcal{L} = \frac{\partial}{\partial x} R_{xx} \frac{\partial}{\partial x} + \frac{\partial}{\partial x} R_{xy} \frac{\partial}{\partial y} + \frac{\partial}{\partial y} R_{yx} \frac{\partial}{\partial x} + \frac{\partial}{\partial y} R_{yy} \frac{\partial}{\partial y}$$

where

$$R_{xx} = \begin{pmatrix} 0 & 0 & 0 & 0 \\ 0 & \frac{4}{3}\mu & 0 & 0 \\ 0 & 0 & \mu & 0 \\ 0 & \frac{4}{3}\mu u & \mu v & \kappa \end{pmatrix} \quad R_{xy} = \begin{pmatrix} 0 & 0 & 0 & 0 \\ 0 & 0 & -\frac{2}{3}\mu & 0 \\ 0 & \mu & 0 & 0 \\ 0 & \mu v & -\frac{2}{3}\mu u & 0 \end{pmatrix}$$

$$R_{yx} = \begin{pmatrix} 0 & 0 & 0 & 0 \\ 0 & 0 & \mu & 0 \\ 0 & -\frac{2}{3}\mu & 0 & 0 \\ 0 & -\frac{2}{3}\mu v & \mu u & 0 \end{pmatrix} \quad R_{yy} = \begin{pmatrix} 0 & 0 & 0 & 0 \\ 0 & \mu & 0 & 0 \\ 0 & 0 & \frac{4}{3}\mu & 0 \\ 0 & \mu u & \frac{4}{3}\mu v & \kappa \end{pmatrix}$$

The three-dimensional version of the equations and coordinate transformations are given in [18].

## A.2 Turbulent Reacting System

### A.2.1 Two-Dimensional Equations

The two-dimensional Navier-Stokes equations coupled to the turbulence and species transport equations are given as,

$$\frac{\partial Q}{\partial t} + \frac{\partial E}{\partial x} + \frac{\partial F}{\partial y} = \mathcal{L}(Q_p) \quad (\text{A.3})$$

where the vectors  $Q$ ,  $E$  and  $F$  are defined as,

$$Q = \begin{pmatrix} \rho \\ \rho u \\ \rho v \\ e \\ \rho k \\ \rho \varepsilon \\ \rho Y_i \end{pmatrix} \quad E = \begin{pmatrix} \rho u \\ \rho u^2 + p_t \\ \rho uv \\ (e + p_t)u \\ \rho uk \\ \rho u \varepsilon \\ \rho u Y_i \end{pmatrix} \quad F = \begin{pmatrix} \rho v \\ \rho uv \\ \rho v^2 + p_t \\ (e + p_t)v \\ \rho vk \\ \rho v \varepsilon \\ \rho v Y_i \end{pmatrix}$$

where  $p_t = p + \frac{2}{3}\rho k$  and  $e = \rho h_0 - p_t$  with  $h_0 = h + \frac{1}{2}(u^2 + v^2) + \frac{5}{3}k$ .

## Appendix B

# Preconditioning System for the Fluids Equations

### B.1 Preconditioned Equations

#### B.1.1 Equations in Generalized Coordinates

The 2D preconditioned equations in generalized coordinates are given as,

$$\Gamma_p \frac{\partial \hat{Q}_p}{\partial \tau} + \frac{\partial \hat{E}}{\partial \xi} + \frac{\partial \hat{F}}{\partial \eta} = 0 \quad (\text{B.1})$$

where

$$\hat{Q}_p = \frac{Q}{J}$$

$$\hat{E} = \frac{1}{J}(\xi_x E + \xi_y F)$$

$$\hat{F} = \frac{1}{J}(\eta_x E + \eta_y F)$$

and the preconditioning matrix is defined as,

$$\Gamma_p = \begin{pmatrix} \rho'_p & 0 & 0 & \rho'_T \\ u\rho'_p & \rho & 0 & u\rho'_T \\ v\rho'_p & 0 & \rho & v\rho'_T \\ h_o\rho'_p - (1 - \rho h_p) & \rho u & \rho v & h_o\rho'_T + \rho h_T \end{pmatrix}$$

The transformation of the viscous terms is not given here. For more details, please refer [18].

### B.1.2 Definition of the Preconditioning Parameter

The preconditioning matrix contains two artificial property functions,  $\rho'_p$  and  $\rho'_T$ . These parameters are typically defined as,

$$\rho'_p = \frac{1}{V_p^2} - \frac{\rho'_T(1 - \rho h_p)}{\rho h_T} \quad (\text{B.2})$$

$$\rho'_T = \delta \rho_T$$

where  $\delta$  is typically taken to be unity, unless otherwise specified. Equivalently, we may express the preconditioning in terms of the the “artificial” sound speed,

$$\frac{\rho h_T}{d'} = V_p^2$$

The “preconditioned” velocity scale is defined as,

$$V_p = \text{Min}[ \text{Max}(V_{inv}, V_{pgr}, V_{vis}, V_{uns}), c ]$$

Note also that sometimes it is convenient to use the corresponding Mach number scale,  $M_p = V_p/c$ . The various velocity scales in the above expression are defined as,

$$\begin{aligned} V_{inv} &= \sqrt{u^2, v^2} \\ V_{pgr} &= \sqrt{\frac{|\Delta p|}{\rho}} \\ V_{uns} &= \text{Max}\left[\frac{l_x}{\pi \Delta t}, \frac{l_y}{\pi \Delta t}\right] \end{aligned}$$

As for the viscous choice,  $V_{vis}$ , there are two possible sets of choices. The first corresponds to optimizing the max-CFL and the max-VNN,

$$V_{vis}^2 = \text{Max}\left[\frac{\hat{\alpha}(\hat{\alpha} - \hat{U})}{\hat{U}(\hat{\alpha} - \hat{U}) + \frac{\rho h_T}{d}(\xi_x^2 + \xi_y^2)}, \frac{\hat{\beta}(\hat{\beta} - \hat{V})}{\hat{V}(\hat{\beta} - \hat{V}) + \frac{\rho h_T}{d}(\eta_x^2 + \eta_y^2)}\right] \left(\frac{\rho h_T}{d}\right)$$

where  $\hat{U} = u\xi_x + v\xi_y$  and  $\hat{V} = u\eta_x + v\eta_y$  and the parameters  $\hat{\alpha}$  and  $\hat{\beta}$  are defined as,

$$\hat{\alpha} = \frac{CFL}{VNN} \nu(\xi_x^2 + \xi_y^2) \quad \hat{\beta} = \frac{CFL}{VNN} \nu(\eta_x^2 + \eta_y^2)$$

The second choice corresponds to the min-CFL/max-VNN definition and is given as,

$$V_{vis}^2 = \text{Max}\left[\frac{\hat{\beta}(\hat{\beta} - \hat{U})}{\hat{U}(\hat{\beta} - \hat{U}) + \frac{\rho h_T}{d}(\xi_x^2 + \xi_y^2)}, \frac{\hat{\alpha}(\hat{\alpha} - \hat{V})}{\hat{V}(\hat{\alpha} - \hat{V}) + \frac{\rho h_T}{d}(\eta_x^2 + \eta_y^2)}\right] \left(\frac{\rho h_T}{d}\right)$$

Finally, we note that the min-CFL/min-VNN choice is obtained by choosing the minimum rather than the maximum in the max-CFL/max-VNN set given above.

## B.2 Jacobians and Eigensystem

### B.2.1 Inviscid Jacobians

For the purposes of deriving the eigenvalues and eigenvectors of the preconditioned equations, we express Eqn. B.1 in the following non-conservative form:

$$\frac{\partial \hat{Q}_p}{\partial \tau} + \Gamma^{-1} \hat{A} \frac{\partial \hat{Q}_p}{\partial \xi} + \Gamma^{-1} \hat{B} \frac{\partial \hat{Q}_p}{\partial \eta} = 0 \quad (\text{B.3})$$

where

$$\hat{A} = \frac{\partial \hat{E}}{\partial \hat{Q}_p}, \quad \hat{B} = \frac{\partial \hat{F}}{\partial \hat{Q}_p}$$

Each of these Jacobians can be expressed in the following generic form,

$$\hat{A} = \begin{bmatrix} \hat{U} \rho_p & \rho \xi_x & \rho \xi_y & \hat{U} \rho_T \\ \xi_x + u \hat{U} \rho_p & \rho(\hat{U} + u \xi_x) & \rho u \xi_y & u \hat{U} \rho_T \\ \xi_y + v \hat{U} \rho_p & \rho v \xi_x & \rho(\hat{U} + v \xi_y) & v \hat{U} \rho_T \\ (\rho_p h_o + \rho h_p) \hat{U} & \rho(h_o \xi_x + u \hat{U}) & \rho(h_o \xi_y + v \hat{U}) & \hat{U} (\rho_T h_o + \rho h_T) \end{bmatrix}$$

with

$$\hat{U} = u \xi_x + v \xi_y$$

Note that  $\hat{B}$  is obtained by substituting  $\eta$  for  $\xi$  and  $\hat{V}$  for  $\hat{U}$ .

### B.2.2 Eigenvalues

The eigenvalues of the preconditioned system are the eigenvalues of the terms,  $\Gamma^{-1} \hat{A}$  and  $\Gamma^{-1} \hat{B}$ , that appear in Eqn. B.3. Again, these terms may be expressed in the following generic form,

$$\Gamma^{-1} \hat{A} = \begin{bmatrix} \frac{\hat{U}}{d'} [\rho'_T (1 - \rho h_p) + \rho \rho_p h_T] & \frac{\rho^2 h_T \xi_x}{d'} & \frac{\rho^2 h_T \xi_y}{d'} & \frac{\rho \hat{U} h_T}{d'} (\rho_T - \rho'_T) \\ \xi_x / \rho & \hat{U} & 0 & 0 \\ \xi_y / \rho & 0 & \hat{U} & 0 \\ \frac{\hat{U}}{d'} (1 - \rho h_p) (\rho_p - \rho'_p) & \frac{\rho(1-\rho h_p)}{d'} \xi_x & \frac{\rho(1-\rho h_p)}{d'} \xi_y & \frac{\hat{U}}{d'} (\rho_T (1 - \rho h_p) + \rho \rho'_p h_T) \end{bmatrix}$$

where  $d' = \rho h_T \rho'_p + \rho'_T (1 - \rho h_p)$ .

The eigenvalues of  $\Gamma^{-1} \hat{X}$  are,

$$\lambda_{1,2} = \hat{U}$$

$$\lambda_{3,4} = \frac{1}{2}[\hat{U}(1 + \frac{d}{d'}) \pm \sqrt{\hat{U}^2(1 - \frac{d}{d'})^2 + 4\frac{\rho h_T}{d'}(\xi_x^2 + \xi_y^2)}]$$

and  $d = \rho h_T \rho_p + \rho_T(1 - \rho h_p)$

### B.2.3 Eigenvector Matrices

The left and right eigenvector matrices corresponding to the above eigenvalues are,

$$M_l = \begin{bmatrix} 0 & 0 & \frac{\tilde{\lambda}_4 - \tilde{U} \frac{d}{d'}}{\tilde{\lambda}_4 - \tilde{\lambda}_3} & \frac{\tilde{\lambda}_3 - \tilde{U} \frac{d}{d'}}{\tilde{\lambda}_3 - \tilde{\lambda}_4} \\ -\frac{\tilde{U}(\rho_T - \rho'_T)\tilde{\xi}_x}{\rho} & -\tilde{\xi}_y & \frac{\tilde{\xi}_x}{\rho(\tilde{\lambda}_3 - \tilde{\lambda}_4)} & \frac{\tilde{\xi}_x}{\rho(\tilde{\lambda}_4 - \tilde{\lambda}_3)} \\ -\frac{\tilde{U}(\rho_T - \rho'_T)\tilde{\xi}_y}{\rho} & \tilde{\xi}_x & \frac{\tilde{\xi}_y}{\rho(\tilde{\lambda}_3 - \tilde{\lambda}_4)} & \frac{\tilde{\xi}_y}{\rho(\tilde{\lambda}_4 - \tilde{\lambda}_3)} \\ 1 & 0 & \frac{1 - \rho h_p}{\rho h_T} \frac{\tilde{\lambda}_4 - \tilde{U} \frac{d}{d'}}{\tilde{\lambda}_4 - \tilde{\lambda}_3} & \frac{1 - \rho h_p}{\rho h_T} \frac{\tilde{\lambda}_3 - \tilde{U} \frac{d}{d'}}{\tilde{\lambda}_3 - \tilde{\lambda}_4} \end{bmatrix}$$

$$M_r^{-1} = \begin{bmatrix} -\frac{1 - \rho h_p}{\rho h_T} & 0 & 0 & 1 \\ 0 & -\tilde{\xi}_y & \tilde{\xi}_x & 0 \\ 1 - \frac{\tilde{U}(1 - \rho h_p)(\rho_T - \rho'_T)}{(\tilde{\lambda}_3 - \tilde{U})d'} & \rho[\tilde{\lambda}_3 - \tilde{U} \frac{d}{d'}]\tilde{\xi}_x & \rho[\tilde{\lambda}_3 - \tilde{U} \frac{d}{d'}]\tilde{\xi}_y & \frac{\rho \tilde{U} h_T (\rho_T - \rho'_T)}{(\tilde{\lambda}_3 - \tilde{U})d'} \\ 1 - \frac{\tilde{U}(1 - \rho h_p)(\rho_T - \rho'_T)}{(\tilde{\lambda}_4 - \tilde{U})d'} & \rho[\tilde{\lambda}_4 - \tilde{U} \frac{d}{d'}]\tilde{\xi}_x & \rho[\tilde{\lambda}_4 - \tilde{U} \frac{d}{d'}]\tilde{\xi}_y & \frac{\rho \tilde{U} h_T (\rho_T - \rho'_T)}{(\tilde{\lambda}_4 - \tilde{U})d'} \end{bmatrix}$$

where

$$\tilde{\xi}_x = \frac{\xi_x}{\sqrt{\xi_x^2 + \xi_y^2}} \quad \tilde{\xi}_y = \frac{\xi_y}{\sqrt{\xi_x^2 + \xi_y^2}}$$

and

$$\tilde{U} = \tilde{\xi}_x u + \tilde{\xi}_y v \quad \tilde{\lambda}_{3,4} = \frac{\lambda_{3,4}}{\sqrt{\xi_x^2 + \xi_y^2}}$$

Again, the 3D versions of these matrices are given in [18].

# Appendix C

## Formulation of Upwind Schemes

### C.1 Flux-Difference Splitting Procedure

The numerical representation of the convective fluxes at the cell faces is defined by,

$$\hat{E}_{i+1/2} = \frac{1}{2} [E_{i+1} + E_i] - \hat{D}_{i+1/2} \quad (\text{C.1})$$

with similar definitions for  $\hat{E}_{i-1/2}$  and  $\hat{F}_{j\pm 1/2}$ . The artificial diffusivity,  $\hat{D}_{i+1/2}$ , is given by,

$$\hat{D}_{i+1/2} = k_1[\Delta E_{i+1/2}^+ - \Delta E_{i+1/2}^-] - k_2[\Delta E_{i-1/2}^+ - \Delta E_{i+3/2}^-] - k_3[\Delta E_{i+3/2}^+ - \Delta E_{i-1/2}^-]$$

When preconditioning is used, the preconditioning matrix,  $\Gamma$ , should be included in the definition of the artificial diffusivity,  $\hat{D}_{i+1/2}$ . Therefore, the above expressions are defined according to,

$$\Delta E_{i\pm 1/2}^\pm = (\Gamma M_x \Lambda_x^\pm M_x^{-1})_{i\pm 1/2} \Delta Q_{p_{i\pm 1/2}}$$

and

$$\Lambda_x = M_x^{-1}(\Gamma^{-1}A)M_x$$

where  $\Delta Q_{p_{i+1/2}} = Q_{p_{i+1}} - Q_{p_i}$ ,  $M_x$  and  $M_x^{-1}$  are the modal matrices which diagonalize  $\Gamma^{-1}A$ , and  $A = \partial E / \partial Q_p$ . Similar definitions can be given for  $\Delta F_{j\pm 1/2}^\pm$ . We note that, in this formulation, if we set  $\Gamma = I$  and  $Q_p = Q$ , we obtain the flux-differencing scheme for the standard (non-preconditioned) system.

In Eqn. C.1, a first-order upwind flux is given by choosing  $(k_1, k_2, k_3) = (1/2, 0, 0)$ , and a third-order upwind-biased flux is obtained from  $(k_1, k_2, k_3) = (1/6, 1/6, 0)$ . A second-order central flux plus a third-order matrix dissipation can be obtained by setting  $(k_1, k_2, k_3) = (1/4, 1/8, 1/8)$ . The standard central-difference representation is obtained by setting  $(k_1, k_2, k_3) = (0, 0, 0)$  and adding fourth-order scalar dissipation.

Further, in order to simplify the presentation of upwind schemes, we adopt the following notation:

$$\mathcal{A}_i^\pm = \frac{1}{2} (A_i \pm \Gamma|\Gamma^{-1}A|_{i\pm 1/2}), \quad \mathcal{B}_j^\pm = \frac{1}{2} (B_j \pm \Gamma|\Gamma^{-1}B|_{j\pm 1/2})$$

with

$$|\Gamma^{-1} A| = M_x |\Lambda_x| M_x^{-1}$$

These definitions are employed to represent the implicit linearization of the flux-difference scheme as shown in Section 1.2.3.

## C.2 Relationship Between Relaxation Methods and Approximate Factorization

We begin with the unfactored form of the Euler Implicit upwind system in Eqn. 1.10:

$$\left[ I + \frac{\Delta t}{\Delta x} (\nabla_x \mathcal{A}^+ + \Delta_x \mathcal{A}^-) + \frac{\Delta t}{\Delta y} (\nabla_y \mathcal{B}^+ + \Delta_y \mathcal{B}^-) \right] \Delta Q = -\Delta t \mathcal{R}^n \quad (\text{C.2})$$

Using the notation given in Section 1.2.4, we express this equation as:

$$[\mathcal{D} + \mathcal{T}_1 + \mathcal{T}_2] \Delta Q = -\Delta t \mathcal{R}^n \quad (\text{C.3})$$

where we note that  $\Delta Q = Q^{n+1} - Q^n$ .

A generic symmetric relaxation technique may be expressed by the following two steps:

$$\begin{aligned} [\mathcal{D} + \mathcal{T}_1] \Delta Q^* &= -\Delta t \mathcal{R}^n - \mathcal{T}_2 \Delta Q^k \\ [\mathcal{D} + \mathcal{T}_2] \Delta Q^{k+1} &= -\Delta t \mathcal{R}^n - \mathcal{T}_1 \Delta Q^* \end{aligned} \quad (\text{C.4})$$

where  $\Delta Q^*$  is a provisional value after the first relaxation sweep. Note that in the case of ADI-type schemes, the first step would correspond to a line-implicit  $x$  sweep, while the second step would correspond to a line-implicit  $y$  sweep. For point Gauss-Seidel iterations, the two steps would correspond to a lower-upper sweep combination.

The first step of Eqn. C.4 may be re-written in the following ‘delta’ form in terms of the inner iteration counter,  $k$ :

$$[\mathcal{D} + \mathcal{T}_1] (Q^* - Q^k) = -\Delta t \mathcal{R}^n - [\mathcal{D} + \mathcal{T}_1 + \mathcal{T}_2] \Delta Q^k \quad (\text{C.5})$$

And, the second step may be re-written as:

$$[\mathcal{D} + \mathcal{T}_2] (Q^{k+1} - Q^k) = Q^* - Q^k \quad (\text{C.6})$$

Equations C.5 and C.6 may be combined and written as:

$$(\mathcal{D} + \mathcal{T}_1) \mathcal{D}^{-1} (\mathcal{D} + \mathcal{T}_2) (Q^{k+1} - Q^k) = -\Delta t \mathcal{R}^n - (\mathcal{D} + \mathcal{T}_1 + \mathcal{T}_2) (Q^k - Q^n) \quad (\text{C.7})$$

which is the approximately factored expression that is used in Section 1.2.4.

# Bibliography

- [1] D. A. Anderson, J. C. Tannehill and R. H. Pletcher, *Computational Fluid Dynamics and Heat Transfer*, Hemisphere Publishing Corporation, 1984.
- [2] C. Hirsch, *Numerical Computation of Internal and External Flows*, Vol. 1 and 2, John Wiley and Sons, 1991.
- [3] C. L. Merkle and S.-T. Yu, *Computational Fluid Dynamics of Inviscid and High Reynolds Number Flows*, (to be published).
- [4] Briley, W.R. and McDonald, H., "Solution of the Multidimensional Compressible Navier-Stokes Equations by a Generalized Implicit Method," *Journal of Computational Physics*, Vol. 24, 1977, pp. 372-397.
- [5] Warming, R. F. and Beam, R. M., "On the Construction and Application of Implicit Factored Schemes for Conservation Law," *SIAM-AMS Proceedings*, Vol. 11, 1978, pp. 85-129.
- [6] Pulliam, T. H. and Chaussee, D. S., "A Diagonal Form of an Implicit Approximate Factorization Algorithm," *Journal of Computational Physics*, Vol. 39, 1981, pp. 347-363.
- [7] P. L. Roe, "Approximate Riemann Solvers, Parameter Vectors, and Difference Schemes," *Journal of Computational Physics*, Vol. 43, pp. 357-372, 1981.
- [8] Chakravarthy, S.R., "Relaxation Methods for Unfactored Implicit Upwind Schemes," AIAA Paper 84-0165, 1984.
- [9] Lombard, C.K., Bardina, J., Venkatapathy, E. and Oliker, J., "Multi-Dimensional Formulation of CSCM – An Upwind Flux Difference Eigenvector Split Method for the Compressible Navier-Stokes Equations," AIAA Paper 83-1895, 1983.
- [10] Thomas, J.L. and Walters, R.W., "Upwind Relaxation Algorithm for the Navier-Stokes Equations," *AIAA Journal*, Vol. 25, No. 4, 1987, pp. 527-534.
- [11] Vanden, K.J. and Whitfield, D.L., "Direct and Iterative Algorithms for the Three-Dimensional Euler Equations," AIAA Paper 93-3378-CP, 1993.

- [12] MacCormack, R.W. and Candler, G.V., "The Solution of the Navier-Stokes Equations Using Gauss-Seidel Line Relaxation," *Computers and Fluids*, Vol. 17, No. 1, 1989, pp. 135-150.
- [13] MacCormack, R. W., "A New Implicit Algorithm for Fluid Flow," AIAA Paper CP-97-2100, June 1997.
- [14] Pulliam, T. H., MacCormack, R. W. and Venkateswaran, S., "Convergence Characteristics of Several Approximate Factorization Schemes," 16th International Conference on Numerical Methods in Fluid Dynamics, Arcachon, France, July 6-10, 1998.
- [15] Klopfer, G. H., Hung, C. M., Van der Wijngaart R. F. and Onufer, J. T., "A Diagonalized Diagonally Dominant Alternating Direction Implicit (D3ADI) Scheme and Subiteration Correction," AIAA 98-2824, 29th AIAA Fluid Dynamics Conference, Albuquerque, NM, June, 1998.
- [16] Huang, P. G., Coakley, T. J. and Buning, P. G., "On Iterative Diagonally Dominant ADI Algorithm," To be published as a NASA TM.
- [17] Venkateswaran, S., Buelow, P. E. O. and Merkle, C. L., "Development of Linearized Preconditioning Methods for Enhancing Robustness and Efficiency of Euler and Navier-Stokes Computations," AIAA CP 97-2030, 13th AIAA Computational Fluid Dynamics Conference, Snowmass, CO, 1997.
- [18] Buelow, P. E. O., *Convergence Enhancement of Euler and Navier-Stokes Computations*, Ph. D. Thesis, Department of Mechanical Engineering, Penn State University, December, 1995.
- [19] Chorin, A. J., "A Numerical Method for Solving Incompressible Viscous Flow Problems," *Journal of Computational Physics*, Vol. 2, pp. 12, 1967.
- [20] Chakravarthy, S. R., "Euler Equations—Implicit Schemes and Boundary Conditions," *AIAA Journal*, Vol. 21, No. 5, pp. 696-706, 1983.
- [21] Kwak, D., Chang, J. L. C., Shanks, S. P., and Chakravarthy, S., "A Three-Dimensional Incompressible Navier-Stokes Flow Solver Using Primitive Variables," *AIAA Journal*, Vol. 24, No. 3, pp. 390-396, 1986.
- [22] Choi, D. and Merkle, C. L., "Application of Time-Iterative Schemes to Incompressible Flow," *AIAA Journal*, Vol. 23, pp. 1518-1524, 1985.
- [23] Rehm, R. G. and Baum, H. R., *Journal of Research of the National Bureau of Standards*, Vol. 83, pp. 297, 1978.
- [24] Guerra, J. and Gustafsson, B., "A Numerical Method for Incompressible and Compressible Flow Problems with Smooth Solutions," *Journal of Computational Physics*, Vol. 63, pp. 377, 1986.

- [25] Merkle, C. L. and Choi, Y.-H., "Computation of Low Speed Compressible Flows with Time-Marching Methods," *International Journal for Numerical Methods in Engineering*, Vol. 25, pp. 293-311, 1985.
- [26] Hosangadi, A., Merkle, C. L. and Turns, S. R., "Analysis of Forced Combusting Jets," *AIAA Journal*, Vol. 28, pp. 1473, 1990.
- [27] Venkateswaran, S. and Merkle, C. L., "Numerical Investigation of Bluff-Body Stabilized Microwave Plasmas," *Journal of Propulsion and Power*, Vol. 11, No. 2, March-April, pp. 357-364, 1995.
- [28] Viviand, H., "Pseudo-Unsteady Systems for Steady Inviscid Calculations, Numerical Methods for the Euler Equations of Fluid Dynamics," *SIAM Journal of Numerical Analysis*, pp. 334, 1985.
- [29] Briley, W. R., McDonald, H. and Shamroth, S. J., "A Low Mach Number Euler Formulation and Application to Time-Iterative LBI Schemes," *AIAA Journal*, Vol. 21, No. 24, pp. 1467-1469, 1983.
- [30] Turkel, E., "Preconditioning Methods for Solving Incompressible and Low-Speed Compressible Equations," *Journal of Computational Physics*, Vol. 72, pp. 277-298, 1987.
- [31] Turkel, E., Radespiel, R. and Kroll, N., "Assessment of Two Preconditioning Methods for Aerodynamics Problems," *Computers and Fluids*, Vol. 26, pp. 613-634, 1997.
- [32] Turkel, E., Fiterman, A. and van Leer, B., "Preconditioning and the Limit to the Incompressible Flow Equations," *Computing the Future: Frontiers of Computational Fluid Dynamics*, eds. Caughey, D. A. and Hafez, M. M., Wiley Publishing, pp. 215-234, 1994.
- [33] Turkel, E., Vatsa, V. and Radespiel, R., "Preconditioning Methods for Low Speed Flows," AIAA PAper 96-2460, 1996.
- [34] Choi, Y. H. and Merkle, C. L., "The Application of Preconditioning to Viscous Flows," *Journal of Computational Physics*, Vol. 105, pp. 207-223, 1993.
- [35] Weiss, J. M. and Smith, W. A., "Preconditioning Applied to Variable and Constant Density Flows," *AIAA Journal*, Vol. 33, pp. 2050-2057, 1995.
- [36] Venkateswaran, S., Weiss, J. M. Merkle, C. L. and Choi, Y. H., "Propulsion-Related Flowfields Using the Preconditioned Navier-Stokes Equations," AIAA 92-3437, Joint Propulsion Conference, Nashville, TN, 1992.
- [37] Jespersen, D., Buning, P. and Pulliam, T., "Recent Enhancements to OVERFLOW," AIAA Paper 97-0644, 1997.

- [38] Edwards, J. and Liou, M. S., "Low Diffusion Flux Splitting Methods for Flows at All Speeds," AIAA 97-1862, 13th AIAA CFD Conference, Snowmass, CO, 1997.
- [39] Van Leer, B., Lee, W. T. and Roe, P. L., "Characteristic Time-Stepping or Local Preconditioning of the Euler Equations," AIAA Paper 91-1552-CP, Computational Fluid Dynamics Conference, Honolulu, 1991.
- [40] Darmofal, D. and van Leer, B., "Local Preconditioning: Manipulating Mother Nature to Fool Father Time," *Computing the Future II: Advances and Prospects in Computational Aerodynamics*, M. Hafez and D. Caughey, eds. John Wiley and Sons, 1998.
- [41] Darmofal, D. and Schmid, P., "The Importance of Eigenvectors for Local Preconditioners of the Euler Equations," *Journal of Computational Physics*, Vol. 127, pp. 346-362, 1996.
- [42] Lee, D., *Local Preconditioning of the Euler and Navier-Stokes Equations*, Ph. D. Thesis, University of Michigan, 1991.
- [43] Darmofal, D. and Siu, K., "A Robust Locally Preconditioned Multigrid Algorithm for the Euler Equations," AIAA Paper 98-2428, 1998.
- [44] Pierce, N. A. and Giles, M. B., "Preconditioned Compressible Flow Calculations in Stretched Meshes," AIAA Paper 96-0889, 1996.
- [45] Venkateswaran, S. and Merkle, C. L., "Analysis of Time-Derivative Preconditioning for the Navier-Stokes Equations," Sixth International Symposium on Computational Fluid Dynamics, pp. 1323-1328, 1995.
- [46] Merkle, C. L. and Venkateswaran. S., "The Use of Asymptotic Expansions to Enhance Computational Methods," AIAA 98-2485, 2nd AIAA Theoretical Fluid Mechanics Meeting, Albuquerque, June, 1998.
- [47] Venkateswaran, S. and Merkle, C. L., "Evaluation of Artificial Dissipation Models and their Relationship to the Accuracy of the Euler and Navier-Stokes Computations," 16th International Conference on Numerical Methods in Fluid Dynamics, Arcachon, France, July 6-10, 1998.
- [48] Godfrey, A. G., Walters, R. W. and van Leer, B., "Preconditioning for the Navier-Stokes Equations," AIAA Paper 93-0535, 1993.
- [49] Buelow, P.E.O., Venkateswaran, S., and Merkle, C.L., "The Effect of Grid Aspect Ratio on Convergence," *AIAA Journal*, vol. 32, No. 12, 1994, pp. 2401-2408. (Also AIAA Paper 93-3367-CP, 1993.)
- [50] Buelow, P. E. O., Venkateswaran, S. and Merkle, C. L., "Grid Aspect Ratio Effects on the Convergence of Upwind Schemes," AIAA Paper 95-0565, 33rd Aerospace Sciences Meeting, Reno, NV, 1995.

- [51] Brandt, A., "Multigrid Techniques with Applications to Fluid Dynamics," *VKI Lecture Series*, 1984-04.
- [52] Mulder, W. A., "Multigrid Relaxation for the Euler Equations," *Journal of Computational Physics*, Vol. 30, pp. 232-252, 1985.
- [53] Hutchison, B. R. and Raithby, G. D., *Numerical Heat Transfer*, Vol. 9, pp. 511-537, 1986.
- [54] Raw, M., AIAA Paper 96-0297, 1996.
- [55] Weiss, J. M., Maruszewski, J. P. and Smith, W. A., "Implicit Solution of the Preconditioned Navier-Stokes Equations Using Algebraic Multigrid," *AIAA Journal*, Vol. 37, No. 1, pp. 29, 1999.
- [56] Mavriplis, D., "Multigrid Strategies for Viscous Flow Solvers on Anisotropic Unstructured Meshes," AIAA Paper 97-1952, 1997.
- [57] Rai, M. M., "Navier-Stokes Simulations of Blade-Vortex Interaction Using High - Order Accurate Upwind Schemes,' AIAA Paper 87-0543, January, 1987.
- [58] Merkle, C. L. and Athavale, M., 'A Time Accurate Unsteady Incompressible Algorithm Based on Artificial Compressibility', AIAA Paper No. 87-1137, AIAA 8th Computational Fluid Dynamics Conference, June 9-11, 1987, Honolulu, HA.
- [59] Rogers, S. E., Kwak, D. and Kiris, C., "Numerical Solution of the Incompressible Navier-Stokes Equations for Steady and Time-Dependent Problems," *AIAA Journal*, Vol. 29, No. 4, pp. 603-610, 1991.
- [60] Withington, J. P., Shuen, J. S. and Yang, V., "A Time-Accurate Implicit Method for Chemically Reacting Flows at All Mach Numbers," AIAA Paper 91-0581, 1991.
- [61] Shuen, J. S., Chen, K. H. and Choi, Y. H., "A Time-Accurate Algorithm for Chemical Non-Equilibrium Viscous Flows at All Speeds," AIAA Paper 92-3639, 1992.
- [62] Venkateswaran, S. and Merkle, C. L., "Dual Time-Stepping and Preconditioning for Unsteady Computations," AIAA 95-0078, 33rd Aerospace Science Sciences Meeting and Exhibit, Reno, NV, 1995.
- [63] McHugh and Ramshaw, 1995.
- [64] Buelow, P. E. O., Schwer, D., Feng, J., Merkle, C. and Choi, D., "A Preconditioned Dual-Time Diagonalized ADI Scheme for Unsteady Computations," AIAA 97-2101, 13th CFD Conference, Snowmass, CO, June, 1997.
- [65] Venkateswaran, S., Deshpande, M. and Merkle, C. L., "Application of Preconditioning to Reacting Flow Computations," AIAA Paper 95-1673, June, 1995.

- [66] Weiss, J. M., "Calculation of Reacting Flowfields Involving Stiff Chemical Kinetics," to be presented at the 14th CFD Conference, Hampton, 1999.
- [67] Merkle, C. L., Sullivan, J. A. Y., Buelow, P. E. O. and Venkateswaran, S., "Computation of Flows with Arbitrary Equations of State," *AIAA Journal*, Vol. 36, No. 4, pp. 515-521, April 1998.
- [68] Merkle, C. L., Feng, J. Z. and Buelow, P. E. O., "Computational Modeling of the Dynamics of Sheet Cavitation," Third International Symposium on Cavitation, Grenoble, France, April, 1998.
- [69] Kunz, R. F., Boger, D. A., Stinebring, D. R., Chyczewski, T. S., Gibeling, H. K. and Govindan, T. R., "Multi-Phase CFD Analysis of Natural and Ventilated Cavitation About Submerged Bodies," FEDSM 99-7364, ASME Summer Fluids Engineering Division Meeting, San Francisco, July, 1999.
- [70] Kunz, R. F., Cope, W. K. and Venkateswaran, S., "Development of an Implicit Method for Multi-Fluid Computations," *Journal of Computational Physics*, accepted for publication, 1999.
- [71] Venkateswaran, S. and Merkle, C. L., "Preconditioning Methods for Multi-Phase Flows," (unpublished).
- [72] Jameson, A., Schmidt, W. and Turkel, E., "Numerical Solutions of the Euler Equations by Finite Volume Methods Using Runge-Kutta Time-Stepping Scheme," AIAA 81-1259, 1981.
- [73] Delanaye, M., *Polynomial Reconstruction Finite Volume Schemes for the Compressible Euler and Navier-Stokes Equations on Unstructured Adaptive Grids*, Ph. D. Thesis, Universite de Liege, 1998.
- [74] Mitcell, R., Sarofim, A., and Clonburg, L., *Combustion and Flame*, Vol. 37, pp. 227, 1980.
- [75] Chang, C., Marek, C., Wey, C., Jones, R., and Smith, M., AIAA Conference Proceedings, 93-2381, 1993.
- [76] Oefelein, J. C. and Yang, V., "Modeling High Pressure Mixing and Combustion Processes in Liquid Rocket Engines," *Journal of Propulsion and Power*, Vol. 14, Number 5, pp. 843, 1998.